Microwave Imaging for Breast Cancer Detection using 3D Level Set based Optimization, FDTD Method and Method of Moments

by

PATEL HARDIK NAYANKUMAR
201221005

A Thesis Submitted in Partial Fulfilment of the Requirements for the Degree of

DOCTOR OF PHILOSOPHY

to

Dhirubhai Ambani Institute of Information and Communication Technology

March, 2019

Declaration

I hereby declare that

    i) the thesis comprises of my original work towards the degree of Doctor of Philosophy at Dhirubhai Ambani Institute of Information and Communication Technology and has not been submitted elsewhere for a degree,

   ii) due acknowledgment has been made in the text to all the reference material used.

<div align="right">

_____

Patel Hardik Nayankumar

</div>

Certificate

This is to certify that the thesis work entitled MICROWAVE IMAGING FOR BREAST CANCER DETECTION USING 3D LEVEL SET BASED OPTIMIZATION, FDTD METHOD AND METHOD OF MOMENTS has been carried out by PATEL HARDIK NAYANKUMAR for the degree of Doctor of Philosophy at _Dhirubhai Ambani Institute of Information and Communication Technology_ under my supervision.

<div align="right">

_____

Prof. Deepak K. Ghodgaonkar

Thesis Supervisor

</div>

Acknowledgments

I would like to thank my father Nayankumar and mother Jashodaben for their support and patience during this PhD journey. I am very thankful to my sister Brinda for encouraging me throughout the study. I would like to thank my little kid Tanay who taught me about unconditional inner happiness. His smile and joy gave me so much confidence. I would like to thank my wife Poonam for her support during this journey. I would like to thank all other family members who have supported directly or indirectly in this journey.

I would like to thank my school teachers and University professors for their direct or indirect contribution in this PhD journey.

Contents

Abstract

Microwave imaging is emerging as new diagnostic option for breast cancer detection because of non-ionizing nature of microwave radiation and significant contrast between dielectric properties of healthy and malignant breast tissues. Class III and IV breasts have more than 50% fibro-glandular tissues. So, it is very difficult to detect cancer in class III and IV breasts by using X-ray based mammography. Microwave imaging is very promising for cancer detection in case of dense breasts. Complex permittivity profile of breasts is reconstructed in three dimensions for microwave breast imaging. 3D level set based optimization proposed in this thesis is able to reconstruct proper shape and dielectric property values of breast tissues.

Multiple frequency inverse scattering problem formulation improves computational efficiency and accuracy of microwave imaging system because complex number computations are avoided. Measurements of scattered electric fields are taken at five equally spaced frequencies in the range 0.5-2.5 GHz. Class III numerical breast phantom and Debye model are used in multiple frequency inverse scattering problem formulation. There are three unknowns per cell of numerical breast phantom due to Debye model. Linear relationships between Debye parameters are applied to get only static permittivity as unknown per cell of numerical breast phantom. Two level set functions are used to detect breast cancer in 3D level set based optimization. Pixel based reconstruction is replaced by initial guess about static permittivity solution in this modified four stage reconstruction strategy. Frequency hopping method is used to avoid local minima present at particular frequency in the 3D level set based optimization. 3D FDTD solves forward problem efficiently during each iteration of 3D level set method which leads to better reconstruction of static permittivity profile.

3D reconstruction problem is very challenging due to Ill posed system matrix and noisy scattered fields data. Tikhonov and total variation (TV) regularization schemes are used to overcome above challenges. The performance of TV regularization is better than Tikhonov regularization in 3D level set based optimization. TV regularization reconstructs shape and size of very small tumour but it fails to reconstruct exact location of very small tumour. Better 3D reconstruction is achieved by using regularized 3D level set based optimization for at least 20 dB SNR in electric field data. 3D FDTD method based electric field computation in heterogeneous numerical breast phantom is very efficient because it solves Maxwell's equations on grids by using an iterative process. Microwave imaging problem is solved with millions of cells because 3D FDTD is used.

Method of moments is used to solve electric field integral equation (EFIE) which estimates complex permittivity of 2048 cell human breast model. Matrix formation and inversion time are reduced to allow large number of cells in breast model. Computational efficiency of the imaging system is improved by exploiting symmetry using group theory. Matrix formed by method of moments is ill posed due to presence of large number of buried cells in inverse scattering formulation. Ill posed system matrix and noise are two major challenges in the solution of inverse scattering problem. Levenberg-Marquardt method is used to solve above challenges.

List of Tables

List of Figures

Chapter 1

Introduction

Breast cancer incidence and mortality are increasing worldwide. Mortality rate can be reduced by early breast cancer detection. It is quite important to understand anatomy of breasts for breast cancer detection system development. Internal structure of human female breast is shown in figure1.1 [1]. Each breast has approximately
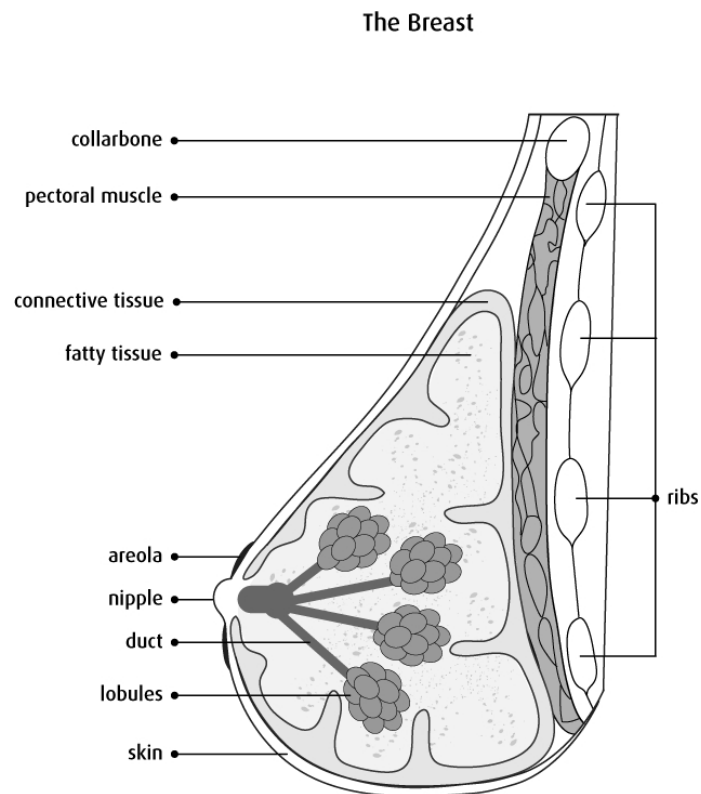
The Breast

Figure 1.1: Human female breast internal structure [1]

14-20 lobes as shown in figure 1.1. These lobes are formed by structure known as lobules. There are bulbs at the end of each lobule which can produce milk and ducts carry milk from lobules to nipple. Whole milk producing network is surrounded by

fatty tissues. Lymph node has ability to filter harmful bacteria. So, lymph nodes are key locations because cancer can spread in other body parts through them.

In general, breast cancer is broadly divided in non-invasive and invasive categories. Non-invasive type of cancers stay within some part of breasts. They do not grow beyond breast. On the other hand, invasive types of cancers do spread in normal healthy tissues. Unfortunately, most breast cancers are invasive. Ductal carcinoma in situ (DCIS), lobular carcinoma in situ (LCIS) and invasive ductal carcinoma, (IDC) are most common types of breast cancer. DCIS type of breast cancer stays inside milk ducts. So it is non-invasive type of breast cancer. LCIS type indicates risk of developing invasive breast cancer. IDC type of breast cancer starts in milk ducts and it spreads in normal healthy breast tissues. Patient's survival depends on early detection of breast cancer. Three main techniques used for breast cancer detection are described below.

X-ray based mammography

It is main technique used for breast screening. In mammography, breasts are compressed between two plates of machine to improve contrast. Now, X-rays are transmitted on breasts. These signals are recorded on film after passing through breasts. Main advantages and disadvantages of mammography are given below.

Advantages

- High sensitivity

- Good Resolution

- Short image formation time

Disadvantages

- Sensitivity is less for dense breasts.

- Low contrast.

- Painful for patients because breasts are pressed to improve image quality.

- It uses ionizing radiation.

Ultrasound Imaging

Ultrasound imaging is also used for breast screening. This system uses ultrasonic waves for imaging which generates breast image by using reflected sound waves. Main advantages and disadvantages of ultrasound are given below.

Advantages

- Non-ionizing radiation

- Examination of dense breasts and implants is possible

- Good resolution

Disadvantages

- Technician's skills based system performance

- Difficult to distinguish solid masses

- Lesions lying deep inside breast are difficult to detect

Magnetic resonance imaging (MRI)

MRI uses magnets and radio waves for breast screening. Patient has to lie on bed which is protected by shield. It is time consuming process. Advantages and disadvantages of MRI are given below.

Advantages

- Non-ionizing technique

- Capability of detecting small tumours

- Multi focal cancers can be detected

Disadvantages

- It is extremely expensive

- It is immobile

- Contrast agent injection is needed

- Time consuming

1.1 Motivation

Breast cancer cases are increasing rapidly with high mortality rate according to globocan [2]. Breast cancer statistics show alarming situation for developing countries [2]. At present, gold standard technique for breast screening is X-rays based mammography. It uses ionizing X-ray radiation for breasts screening. High radiation dose of X-ray or frequent mammography screening increases risk of cancer because X-rays are an ionizing radiation. False negative and false positive rates are about 15% and 13%, respectively in mammography which leads to additional imaging and biopsies [3, 4]. Breasts are compressed between two plates to enhance contrast in mammography which makes it uncomfortable and painful for patients. An alternative breast screening technique is required to overcome above disadvantages of mammography.

Microwave imaging is emerging as new diagnostic option for breast screening in the last decade [3, 4]. Advantages of microwave imaging are mentioned below.

1. Significant contrast has been observed between dielectric properties of healthy and malignant breast tissues over microwave frequencies [5, 6, 7].

2. Non-ionizing nature of microwave radiation is considered as key advantage over X-rays based mammography.

3. Low power microwave signal is used for breast screening which does not harm patient.

It is extremely important to understand breast tissues and tumour cell properties. Breast anatomy gives clear idea about different tissues and their locations which are used in this thesis. Breasts mainly contain fatty and fibro-glandular tissues as shown in figure 1.2 [8, 9]. Tumour detection point of view, it is extremely important to know tumour cell properties given below [10].

1. Dielectric properties of tumour tissues are different from healthy tissues in microwave frequency range [5, 6, 7].
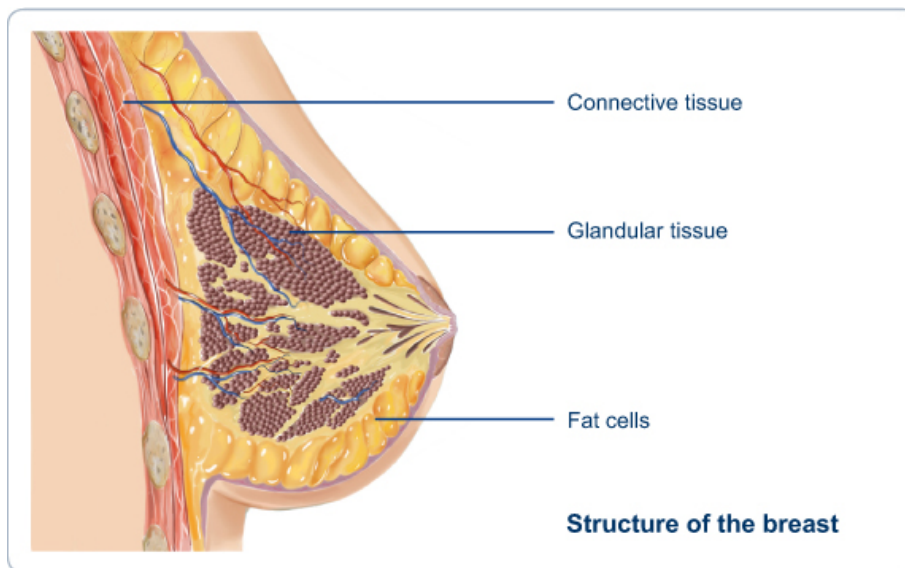
Figure 1.2: Breast anatomy showing main tissues [9]

2. Cell Reproduction rate is higher

3. Glucose and blood consumption are high due to abnormal reproduction rate.

4. Temperature is high due to abnormal reproduction rate.

5. Shape and size are abnormal.

6. Electrical properties are also different

7. They neither become mature nor commit suicide.

8. They don't follow commands of surrounding healthy cells.

First property of tumour cells is base of microwave imaging. Positron emission tomography (PET) is based on third property of tumour cells. Thermography is based on fourth property of tumour cells. Electrical impedance tomography (EIT) is based on sixth property of tumour cells. Microwave imaging is most promising technique as compared to PET, thermography and EIT [4]. There are four classes of breasts according to Breast Imaging Reporting and Data System (BI-RADS). Mammography based images of four breast classes are shown in figure 1.3 [11, 12].

Class I breasts have only 25% glandular tissues which makes it almost entirely fatty. Class II breasts have 25% to 50% scattered glandular tissues. Class III breasts
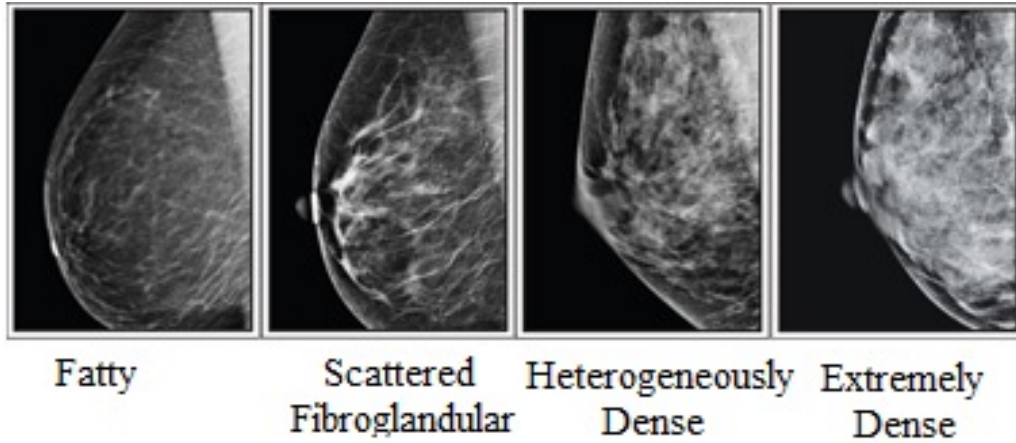
Figure 1.3: Classification of breast according to density. Class I, ClassII, Class III and Class IV breasts(Left to right) [12]

are heterogeneously dense due to 51% to 75% glandular tissues. Class IV breasts are known as extremely dense due to more than 75% of glandular tissues. Women with class III and class IV breasts have high breast cancer risk [13, 14, 15, 16]. The colour of breast tumour is white in mammographic images. It is very difficult to detect tumour in class III and class IV breasts because of white glandular tissues. If tumour is hidden inside glandular tissues then it results into false negative detection. If higher density of glandular tissues is detected as tumour then it results into false positive detection. False positive and false negative rates are higher in class III and class IV breasts [17]. In microwave imaging, inverse scattering problem has been solved by computer to reconstruct microwave image of breast. There are several techniques for microwave image reconstruction. Traditional optimization schemes don't have shape related features. Shape reconstruction is an additional burden in case of 3D image reconstruction.

1.2   Microwave Imaging

Microwave imaging is used to develop image in terms of object's unknown dielectric properties. Dielectric profiles of object are reconstructed using microwaves. These images of dielectric profiles are also known as microwave image. Microwave imaging is classified in two types as shown below.

- Passive microwave imaging

- Active microwave imaging

1.2.1 Passive Microwave Imaging

Electromagnetic signals coming out of tissues are captured in this technique. Electromagnetic signals are captured from breast tissues. Temperature of malignant tumour is higher than the healthy breast tissues. Based on these signals and temperature difference, malignant tissues are distinguished. Figure 1.4 shows typical setup for passive microwave imaging [3]. As shown in figure 1.4, signals from differ-
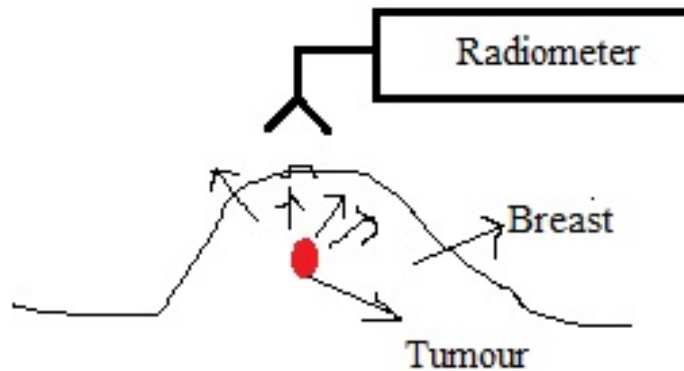
Figure 1.4: Passive microwave imaging setup

ent breast tissues are captured using radiometer, Tumour is detected based on these received signals. Detection of weak signal is involved which makes it more sensitive to noise. It is considered as a disadvantage of passive microwave imaging.

1.2.2 Active Microwave Imaging

Microwave signals are transmitted through antennas placed near object to be imaged. Now, these microwave signals interact with object of interest. Signals are received by antennas after these interaction. These received signals are used to reconstruct microwave image of breast. Active microwave imaging is further divided

in microwave tomography and RADAR based microwave imaging. Typical setup of active microwave imaging is shown in figure 1.5.
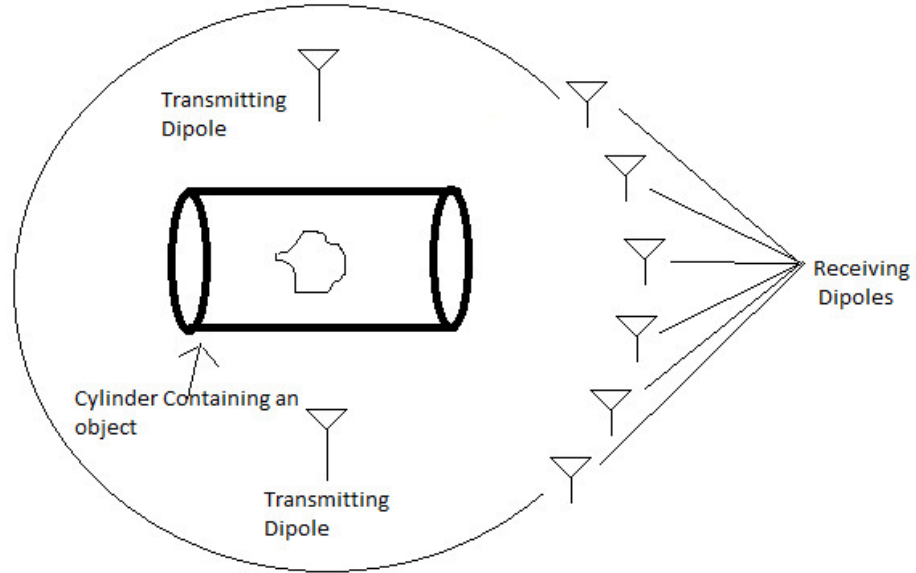
Figure 1.5: Microwave Tomography

In microwave tomography, low power microwave signals are transmitted on breast using antennas. These incident signals are scattered according to dielectric properties of breast tissues. The scattered waves are received by antennas. This process is known as forward problem. To get measured electric field data, noise is added to known scattered field. Dielectric (complex permittivity) profile of breast is reconstructed from noisy scattered fields data. This process is known as inverse scattering problem. Classification of different methods to solve forward and inverse scattering problems is given in [18]. If different sets of antennas are used as transmitters and receivers, then it is known as bi-static system. If same sets of antennas are used as transceivers, then it is known as mono-static system. In radar based microwave imaging, tumour is detected based on high reflection criteria [3].

1.3 Microwave Breast Imaging Research Groups

Well known research groups in microwave breast imaging are shown in Table 1.1 [19]. Imaging method column of table 1.1 clearly shows diversity. Main contributions

Table 1.1: Well known research groups in microwave breast imaging

Group Leader (Starting Year)	Location	Antenna Type (Elements)	Imaging Method
Qing H. Liu (2003)	Duke University, Durham, USA	Patch (32-125)	3D Inversion Methods DTA-BIM, BCGS-DBIM
P.M.Meaney (2000)	Dartmouth College Hanover, USA	Monopole (16)	2D and 3D Inversion Methods
S.C.Hagness (1998)	Wisconsin University Madison, USA	Pyramidal Horn (40)	Space-Time Beam-forming combined with Generalised likelihood ratio test
Elise C. Fear (2002)	University of Calgary Alberta, Canada	Wu-King Monopole	Quasi-3D tissue sensing adaptive radar and Microwave Imaging via Space-Time
Maciej Klemm (2006)	University of Bristol Bristol, UK	Stacked Conformal Patch (16)	Delay and sum beam-forming
Matteo Pastorino (2004)	University of Genoa Genova, Italy	Antenna Array	Genetic Algorithm

of Qing H. Liu's group are 3D forward scattering for microwave breast imaging and microwave-induced thermal acoustic tomography to detect breast tumour [20, 21]. Meaney's group is working on two step inversion method and development of realistic supelec-breast phantom for microwave breast imaging[22, 23]. This group have developed clinical prototype for active microwave imaging of the breast [24]. The group of S.C.Hagness have worked on different areas (e.g., measurements of healthy and malignant breast tissue dielectric properties, Numerical breast phantom development, Debye model development for breast tissues, FDTD based confocal algorithm and 3D level set based microwave breast imaging) of microwave breast imaging [25, 26, 27, 28, 29]. This group has started using FDTD for microwave breast imaging [27, 28]. Elise C. Fear's group is working on comparison of radar-based microwave imaging algorithms applied to experimental breast phantoms [30]. This group has worked in different areas of microwave breast imaging [3, 4, 30, 31, 32].

Maciej Klemm's group is working on development of different types of antenna arrays for microwave breast imaging [33, 34]. This group has also performed clinical trials for microwave breast imaging [35]. Matteo Pastorino's group is working on microwave breast imaging system simulation [36].

1.4   Thesis Organization

Short overview of important chapters is given below.

- **Multiple Frequency Inverse Scattering Problem Formulation**

   Multiple frequency inclusion in the inverse scattering problem improves computational efficiency and accuracy of microwave imaging system. Numerical breast phantom, Antenna placement and Debye model are required for multiple frequency inverse scattering problem formulation. Complex permittivity profile of human breast is function of frequency. Single pole Debye model is used to incorporate frequency dependence of human breast complex permittivity profile. Now, computationally efficient inverse scattering problem is formulated for multiple frequencies. Cost function is calculated using matrix formulation of inverse scattering problem.

- **3D Level Set Based Optimization**

   Human breast complex permittivity profile reconstruction is always challenging in three dimensions. Shape and value reconstructions both are important in three dimension. Shape reconstruction does not involve in most of the current optimization techniques. It can be considered as major drawback in 3D reconstruction. This limitation has been avoided using 3D level set functions. The idea of level set was first proposed by Osher and Sethian in [37]. In level sets, topological merging and breaking is occurred naturally in any number of space dimensions. They don't require that the moving surface be written as a function. One level set function is used to distinguish two different regions. Two level set functions can distinguish four different regions. In general, N level set functions can distinguish 2^N different regions. Evolution and optimization are two main level set approaches used for reconstruction

problems. These two approaches are combined in this thesis work. Novel 3D level set based optimization is used to reconstruct dielectric properties as well as shape of breast images. Debye parameter values and 3D level set functions are updated to minimize cost function. Ill posed system matrix and noisy scattered fields data make 3D reconstruction very challenging. Regularization is used to overcome above challenges.

- **3D FDTD Method**

FDTD is an useful method for simultaneous acquisition of multi-frequency vector electromagnetic fields data over bandwidth of interest. FDTD method is computationally efficient because multiple frequency total electric field vector data acquisition is achieved in just one FDTD simulation. In this work, 3D FDTD is used to get multiple frequency total field vector data inside human breast model. Complex permittivity distribution of human breast model is determined by Debye model. Debye model is required only for numerical breast phantom region on grid. Perfectly matched layer (PML) is used to absorb signals at the boundary. Different sets of electric field update equations are given for PML and numerical breast phantom regions.

- **Method of Moments**

Microwave imaging system is represented by electric field integral equation (EFIE). Method of moments is used to solve electric field integral equation (EFIE) which estimates complex permittivity of 2048 cell human breast model. Matrix formation and inversion time should be reduced to allow large number of cells in breast model. This is achieved by exploiting symmetry using group theory which improve computational efficiency of the imaging system. EFIE is solved by using method of moments to find scattered electric field due to human breast models. Additive white Gaussian noise is added to this electric field vector. Matrix formed by method of moments is ill posed due to presence of large number of buried cells in inverse scattering formulation [38]. The effects of total volume, number of cells, symmetry and multiple view on complex permittivity reconstruction are investigated in this chapter. The effect of saline and

air as surrounding medium on complex permittivity reconstruction is evaluated for microwave breast imaging system.

References

[1] The Breasts, Available at http://www.cancer.ca/en/cancer-information/cancer-type/breast/breast-cancer/the-breasts/?region=on, Accessed on April 2015.

[2] F.Jacques, I.Soerjomataram, R.Dikshit, S.Eser, C.Mathers, M.Rebelo, D.M.Parkin, D.Forman, and F.Bray, "Cancer incidence and mortality worldwide: sources, methods and major patterns in GLOBOCAN 2012," International Journal of Cancer, Vol. 136, no. 5, pp. 359-386, March 2015.

[3] E.C.Fear, S.C.Hagness, P.M. Meaney, M.Okoniewski, M.A.Stuchly, "Enhancing breast Tumor detection with near field imaging" IEEE Microwave Magazine, Vol. 3, No. 1, pp. 48-56, 2002.

[4] E.C.Fear, P.M.Meaney, and M.A.Stuchly, "Microwaves for breast cancer detection," IEEE Potentials, Vol. 22, no. 1, pp. 12-18, 2003.

[5] A.M.Campbell, D.V.Land, "Dielectric properties of female human breast tissue measured in vitro at 3.2 GHz," Physics in Medicine and Biology, Vol. 37, no. 1, pp. 193-210, 1992.

[6] M.Lazebnik, L.McCartney, D.Popovic, C.B.Watkins, M.J.Lindstrom, J.Harter, S.Sewall et al. "A large-scale study of the ultrawideband microwave dielectric properties of normal breast tissue obtained from reduction surgeries," Physics in Medicine and Biology, Vol. 52, no. 10, pp. 2637-2656, 2007.

[7] M.Lazebnik, L.McCartney, D.Popovic, C.B.Watkins, M.J.Lindstrom, J.Harter, S.Sewall et al. "A large-scale study of the ultrawideband microwave dielectric properties of normal, benign and malignant breast tissues obtained from cancer surgeries," Physics in Medicine and Biology, Vol. 52, no. 20, pp. 6093-6115, 2007.

13

[8] R.A.Jesinger, "Breast Anatomy for the Interventionalist," Techniques in Vascular and Interventional Radiology, Elsevier, Vol. 17, no. 1, pp. 3-9, March 2014.

[9] Introduction to Breast Cancer, at https://aboutbrachytherapy.com/de/krebsarten/brustkrebs/, Accessed March 2015.

[10] D.Hanahan, R.A.Weinberg, "Hallmarks of Cancer: The Next Generation," Elsevier, Cell Press, Vol. 144, no. 5, pp. 646-674, March 2011.

[11] C.Zhou, H.P.Chan, N.Petrick, M.A.Helvie, M. M.Goodsitt, B.Sahiner, and L.M.Hadjiiski, "Computerized image analysis: estimation of breast density on mammograms," Medical Physics, Vol. 28, no. 6, pp. 1056-1069, 2001.

[12] J.Lemieux, Both Doctors and Patients Confused by Dense Breasts, Available at https://www.acsh.org/news/2016/09/07/both-doctors-and-patients-confused-dense-breasts-9960, Sep. 2016.

[13] P.M.Vacek, B.M.Geller, "A prospective study of breast cancer risk using routine mammographic breast density measurements," Cancer Epidemiology and Prevention Biomarkers, Vol. 13, no. 5, pp. 715-722, 2004.

[14] N.F.Boyd, G.A.Lockwood, J.W.Byng, D.L.Tritchler, and M.J.Yaffe, "Mammographic densities and breast cancer risk," Cancer Epidemiology and Prevention Biomarkers, Vol. 7, no. 12, pp. 1133-1144, 1998.

[15] C.M.Vachon, C.H.VanGils, T.A.Sellers, K.Ghosh, S.Pruthi, K.R.Brandt, and V.S.Pankratz, "Mammographic density, breast cancer risk and risk prediction," Breast Cancer Research, Vol. 9, no. 6, pp. 217-225, 2007.

[16] P.E.Freer,"Mammographic breast density: impact on breast cancer risk and implications for screening," Radiographics, Vol. 35, no. 2, pp. 302-315, 2015.

[17] H.D.Nelson, E.S.O'meara, K.Kerlikowske, S.Balch, and D.Miglioretti,"Factors Associated With Rates of False-Positive and False-Negative Results From Digital Mammography Screening: An Analysis of Registry Data False-Positive and False-Negative Digital Mammography Screening Results," Annals of Internal Medicine, Vol. 164, no. 4, pp. 226-235, 2016.

[18] Q.Fang, "Computational Methods for Microwave Medical Imaging" PhD Thesis, Thayer School of Engineering, Dartmouth College, USA, 2004.

[19] J.P.Stang, "A 3D Active Microwave Imaging System for Breast Cancer Screening" PhD Thesis, Duke University, USA, 2008.

[20] Z.Q.Zhang, Q.H.Liu, C.Xiao, E.Ward, G.Ybarra, and W.T.Joines, "Microwave breast imaging: 3-D forward scattering simulation." IEEE Transactions on Biomedical Engineering, Vol. 50, No. 10, pp. 1180-1189, 2003.

[21] X.Zhu, Z.Zhao, J.Wang, J.Song, and Q.H.Liu. "Microwave-induced thermal acoustic tomography for breast tumor based on compressive sensing." IEEE Transactions on Biomedical Engineering Vol. 60, No. 5, pp. 1298-1307, 2013.

[22] P.M.Meaney, S.D.Geimer, and K.D.Paulsen. "TwoâĂŘstep inversion with a logarithmic transformation for microwave breast imaging." Medical physics Vol. 44, No. 8 pp. 4239-4251, 2017.

[23] T.Rydholm, A.Fhager, M.Persson, and P.M.Meaney. "A First Evaluation of the Realistic Supelec-Breast Phantom." IEEE Journal of Electromagnetics, RF and Microwaves in Medicine and Biology Vol. 1, No. 2, pp.59-65, 2017.

[24] P.M.Meaney, M.W.Fanning, D.Li, S.P.Poplack, and K.D.Paulsen. "A clinical prototype for active microwave imaging of the breast." IEEE Transactions on Microwave Theory and Techniques 48, no. 11 (2000): 1841-1853.

[25] E.Zastrow, S.K.Davis, M.Lazebnik, F.Kelcz, B.D.Van Veen, and S.C.Hagness, "Development of anatomically realistic numerical breast phantoms with accurate dielectric properties for modelling microwave interactions with the human breast," IEEE Transactions on Biomedical Engineering, Vol. 55, no. 12, pp. 2792-2800, 2008.

[26] M.Lazebnik, M.Okoniewski, J.H.Booske, and S.C.Hagness, "Highly accurate Debye models for normal and malignant breast tissue dielectric properties at microwave frequencies," IEEE Microwave and Wireless Components Letters, Vol. 17, no. 12, pp. 822-824, 2007.

[27] S.C.Hagness, A.Taflove, and J.E.Bridges, "Two-dimensional FDTD analysis of a pulsed microwaved confocal system for breast cancer detection: flxed-focus and antenna-array sensors," IEEE Transactions on Antennas and Propagation, vol. 45, pp. 1470-1479, 1998.

[28] S.C.Hagness, A.Taflove, and J.E.Bridges,"Three-dimensional FDTD analysis of a pulsed microwaved confocal system for breast cancer detection: design of an antenna-array element," IEEE Transactions on Antennas and Propagation, Vol. 47, pp. 783-791, 1999.

[29] T.J.Colgan, S.C.Hagness, and B.D.Van Veen, "A 3-D level set method for microwave breast imaging," IEEE Transactions on Biomedical Engineering, Vol. 62, no. 10, pp. 2526-2534, 2015.

[30] M.Glavin, M.O'Halloran, E.C.Fear, E.Porter, B.R.Lavoie, E.Jones, and M.A.Elahi. "Comparison of radar-based microwave imaging algorithms applied to experimental breast phantoms." In 32nd Internal Union of Radio Science General Assembly & Scientific Symposium (URSI GASS). Union Radio-Scientific International, 2017.

[31] E.C.Fear, J.Bourqui, C.Curtis, D.Mew, B.Docktor, and C.Romano. "Microwave breast imaging with a monostatic radar-based system: A study of application to patients." IEEE transactions on microwave theory and techniques, Vol. 61, no. 5, pp. 2119-2128, 2013.

[32] D.Kurrant, J.Bourqui, C.Curtis, and E.C.Fear. "Evaluation of 3-D acquisition surfaces for radar-based microwave breast imaging." IEEE Transactions on Antennas and Propagation 63, no. 11 (2015): 4910-4920.

[33] M.Klemm, I.J.Craddock, J.A.Leendertz, A.Preece, and R.Benjamin. "Radar-based breast cancer detection using a hemispherical antenna arrayâĂŤExperimental results." IEEE transactions on antennas and propagation 57, no. 6 (2009): 1692-1704.

[34] D.Gibbins, M.Klemm, I.J.Craddock, J.A.Leendertz, A.Preece, and R.Benjamin. "A comparison of a wide-slot and a stacked patch antenna for the purpose of

breast cancer detection." IEEE transactions on antennas and propagation 58, no. 3 (2010): 665-674.

[35] T.Henriksson, M.Klemm, D.Gibbins, J.Leendertz, T.Horseman, A.W.Preece, R.Benjamin, and I.J.Craddock, "Clinical trials of a multistatic UWB radar for breast imaging." In IEEE Antennas and Propagation Conference (LAPC), 2011 Loughborough, pp. 1-4., 2011.

[36] G.Bozza, M.Brignone, and M.Pastorino. "Application of the no-sampling linear sampling method to breast cancer detection." IEEE Transactions on Biomedical Engineering, Vol.57, No. 10, pp. 2525-2534, 2010.

[37] S.Osher, J.A.Sethian, "Fronts propagating with curvature-dependent speed: algorithms based on Hamilton-Jacobi formulations,"Journal of Computational Physics, Vol. 79, pp. 12-49, 1988.

[38] D.K.Ghodgaonkar, O.P.Gandhi and M.J.Hagmann, "Estimation of complex permittivities of 3D inhomogeneous biological bodies," IEEE Transactions on Microwave Theory and Techniques, Vol. 31, no. 6, pp. 442-446, 1983.

Chapter 2

Literature Review

Cancer incidence and mortality analysis is very important for prevention and early detection of cancer. GLOBOCAN is an initiative of world health organization (WHO) which aims to provide estimates of the incidence, prevalence and mortality from major cancer types for 184 countries. In USA, 43909 women died out of 232714 women with newly diagnosed breast cancer during 2012 [1]. One woman died in every 6 women who were diagnosed with breast cancer in USA [1]. In China, 47984 women died out of 187213 women with newly diagnosed breast cancer during 2012 [1]. One woman died in every 4 women who were diagnosed with breast cancer in china [1]. Year wise statistics of breast cancer is provided in figure 2.1 for India [1]. In India, 70218 women died out of 144937 women with newly diagnosed breast
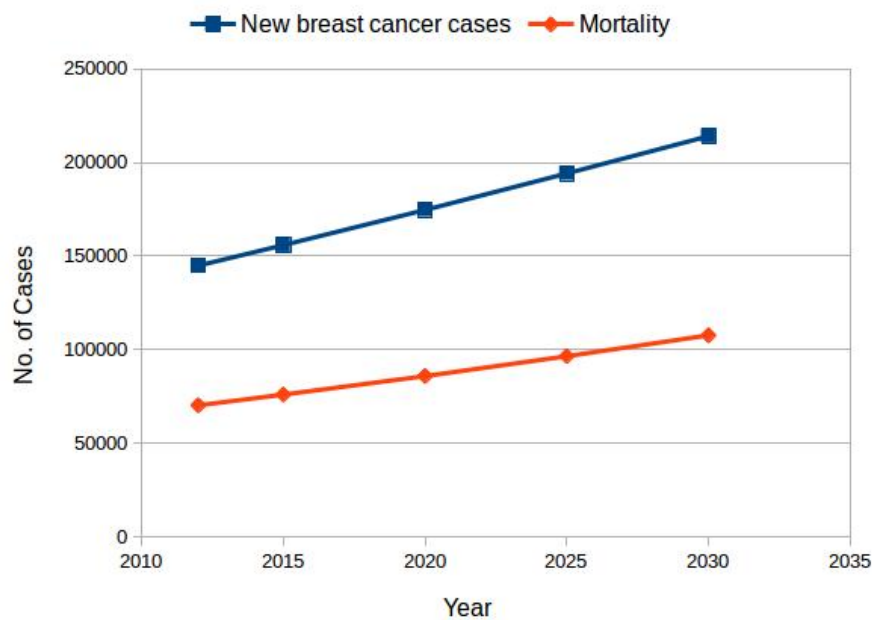
Figure 2.1: Breast cancer statistics in India[1]

cancer during 2012 [1]. One women died in every 2 women who were diagnosed with breast cancer in India [1]. Breast cancer incidences and mortality rate are projected to be high in India, according to statistics of figure 2.1.

Fear et al. have described different types of microwave imaging modalities with significant advantages over X-ray based mammography in [2, 3]. They have provided very promising initial results and analysis of microwave breast imaging. Microwave images have better contrast as compared to X-ray based mammography [2, 3]. Dielectric properties of breast tissues are measured in [4, 5, 6]. Campbell et al. have measured dielectric properties of female human breast tissues at 3.2 GHz in [4]. Their work was converted in online resource which provides dielectric constant values for different human tissues from 10 Hz to 100 GHz. Lazebnik et al. have measured dielectric properties of healthy breast tissues obtained after reduction surgeries in [5]. They have used microwave spectroscopy for this measurement in the frequency range of 0.5 GHz to 20 GHz. Lazebnik et al. have measured dielectric properties of normal, benign and malignant breast tissues obtained after reduction surgeries in [6]. These measured values are widely used in microwave breast imaging research.

Jesinger has given breast internal structure details in [7], which provides useful insights to breast cancer researchers. Hanahan et al. have described great details of human cancer cell properties in [8], which provides very useful information for breast cancer researcher. Zhou et al. have estimated breast density based on analysis of mammographic computer images in [9]. They have estimated four classes of breast which are very useful in risk analysis of breast cancer. Breast cancer risk factors based on mammographic breast density are investigated in [10, 11, 12, 13]. Class III and IV breasts have higher cancer risk as compared to class I and II breasts. Above conclusion clearly suggests use of class III or IV breast models in simulation experiment. Nelson et al. have investigated factors associated with false positive and false negative rates for digital mammography screening in [14]. Their investigation suggests higher breast density results in high false positive and false negative rates.

2.1 Multiple Frequency Inverse Scattering Problem Formulation

Complex permittivity profile of human breast is function of temperature and frequency. Temperature is assumed to be constant. Frequency dependence of human breast complex permittivity profile is incorporated by using single pole Debye model. Now, computationally efficient inverse scattering problem is formulated for multiple frequencies. Cost function is calculated using matrix formulation of inverse scattering problem. Multiple frequency inclusion in inverse scattering problem leads to better reconstruction. Numerical breast phantom, Debye model and antenna placement are required for multiple frequency inverse scattering problem formulation. Zastrow et al. have developed anatomically realistic numerical breast phantom with accurate dielectric properties in [15]. They have provided their class III numerical breast phantom in online repository which is used in our work. Lazebnik et al. have developed highly accurate Debye models for normal and malignant breast tissues using data fitting in [16]. Winters et al. have proposed formulation of multiple frequency inverse scattering problem for dispersive dielectric properties estimation by using patient specific Gaussian basis function in [17]. Shea et al. have used multiple frequency inverse scattering problem formulation with 3D FDTD in [18]. They have solved forward and inverse scattering problems by using 3D FDTD and conjugate gradient respectively in [18]. Garret et al. have proposed a novel technique to analyse average dielectric properties of breast tissues with multipath effect mitigation in [19]. Kurrant et al. have investigated hemispherical, cylindrical and patient specific 3D data acquisition surfaces in [20]. The patient specific acquisition surface of Kurrant et al. results in better object coverage, good target responses and improved images as compared to other two acquisition surfaces. Bourqui et al. have proposed ultra wideband sensors with time delay spectroscopy to estimate dielectric properties of human breast tissues for 1.5 to 10 GHz frequency range in [21]. Their results show only about 2% error in the estimation of human breast dielectric properties.

2.2 Level Set Methods for Optimization

Human breast complex permittivity profile reconstruction is always challenging in three dimensions. Shape and value reconstructions both are important in three dimension. Shape reconstruction is not involved in most of the current optimization techniques. It is considered as major drawback in 3D reconstruction. This limitation is avoided using 3D level set functions. Novel 3D level set based optimization is used to reconstruct values as well as shape of complex permittivity profile. Debye parameter values and 3D level set functions are updated to minimize cost function. Ill posed system matrix and noisy scattered fields data make 3D reconstruction very challenging. Regularization is used in 3D level set based optimization to overcome above challenges. Osher et al. have solved Hamilton-Jacobi equation by using moving fronts with curvature dependent speed in [22]. Now, their work is recognized as level set methods. The algorithm proposed by Osher et al. handles topology merging and breaking naturally which makes it attractive for shape reconstruction. Osher et al. have proposed level set method with fast marching method and extension velocity in [23]. Their level set methods are used widely in many fields of science, engineering and technology now. Santosa has proposed level set based evolution and optimization approaches for inverse problems with deconvolution and diffraction screen reconstruction examples in [24].

Dorn et al. have proposed an efficient two step shape reconstruction method for electromagnetic cross-borehole tomography using adjoint fields and level set in [25]. In this method, shape of obstacle is reconstructed by applying adjoint fields and level set to an initial guess. FDTD is used twice per iteration to solve helmholtz equations. Dorn et al. have consider Only shape reconstruction of object by using known permittivity values inside the object. This level set method is the method of asymptotic regularization, which has been developed for ill-posed problems in Hilbert spaces. They have shown regularizing properties of the level set method with the discrepancy principle as a stopping criteria. Ferraye et al. have proposed a shape reconstruction of obstacle for electromagnetic tomography using level set method

based on contour deformations with frequency hopping technique in [26]. In this approach, automatic merging and breaking capability is used for shape reconstruction inverse scattering problem.

A very good survey of level set method for inverse problems is done in [27, 28, 29]. Survey includes general level set method formulation for following areas.

1. Geometry based inverse and optimization problems

2. Level set methods based evolving interfaces

3. Shape calculus by using level set method

4. Level set methods based shape optimization

5. Level set method for ill posed problems

General framework for above topics are given nicely with several open issues in [27, 28]. Recent techniques which have a level set based representation of shapes for solving inverse scattering problems are given in [29]. Electromagnetic scattering by using different popular models, for example TM-polarized and TE-polarized waves, Maxwell's equations, impedance tomography, a transport equation or its diffusion approximation are described with topological derivatives and shape sensitivity analysis in this work. Various techniques are proposed with realistic application examples in two and three dimensions for incorporating regularization into the shape inverse scattering problem.

Aghasi et al. have proposed reconstruction of obstacles by using parametric level set method in [30]. General level set evolution equations are derived for an unknown obstacle reconstruction. Significantly lower dimensional problem is obtained by applying appropriate form of parametric level set function. Radial basis function is used to make the parametric level set which provide a "narrow-banding" advantage that the number of unknowns are reduced at each step of the evolution by using this approach. The performance of this approach is tested in diffuse optical tomography, electrical impedance tomography and X-ray computed tomography.

Semerci et al. have proposed a novel polychromatic dual-energy processing algorithm, which can detect and characterize objects embedded in background [31]. In this paper, Level-set based characteristic function of the object is used with a number of regularization techniques for addressing both the physical properties of the object and the prior information. The proposed approach gives zero characteristic function in the absence of an object. So, it can be viewed as simultaneously solving both characterization and detection problems. Level set is defined parametrically by using radial basis functions with a Gauss-Newton algorithm for cost minimization. Numerical results show that the algorithm successfully detects objects. It also finds objects' shape, location with reconstruction of the background. A modified level set method (MLSM) is proposed to reconstruct 2D object's shape and electrical properties simultaneously in [32]. Eskandari et al. have proposed an evolution strategy to reconstruct complex permittivity and shape of a 2D object. As the cost function is minimized iteratively, the initial guesses about the complex permittivity and shape of the target object converge to their values. L_1 and L_2 norms are added to cost function as regularization terms. Sudden changes in the shape of the object are prevented by a curvature-based regularization. Fluctuations in the object's parameters are reduced by Laplacian based regularization. The capabilities of MLSM in microwave imaging are evaluated by using different synthetic data sets. Two objects separated by a distance of one-fifteenth of a wavelength can be reconstructed completely using MLSM. Targets of different relative permittivity can be retrieved with less than 10% error by using this method. Reconstruction of the immersed one-tenth wavelength targets in highly contrasting domains is considered as an important feature of this method. These features of MLSM are precious in distinguishing malignant tissues from normal tissues.

Irishina et al. have proposed level set based evolution strategy in two broad steps for early breast cancer detection using microwave imaging [33]. In the first step, location and size of tumour is found. Where as in second step dielectric property of tumour is determined. Level set method of [33] is verified by 2D numerical breast phantom. The tumour characterization may fail for very small hidden breast tumours in the presence of strong noise [33]. Irishina et al. have proposed level set

based strategy for microwave imaging based early breast cancer detection in [34, 35]. Level set based solution has advantages over traditional pixel based approaches when reconstruction of size, shape and static permittivity value of hidden tumour is very crucial. Level set based strategy is useful for correct estimation of interfaces between fibro-glandular and fatty tissues. Level set based proposed strategy of [34, 35] is able to detect and characterize small tumours successfully. In order to reconstruct correct shape, size and location of tumour an initial guess of tumour permittivity value is required.

Reconstructed difference permittivity ($\Delta\epsilon$) profile of class 3 numerical breast phantom by using conjugate gradient method is shown in figure 2.2 [18]. Results of figure
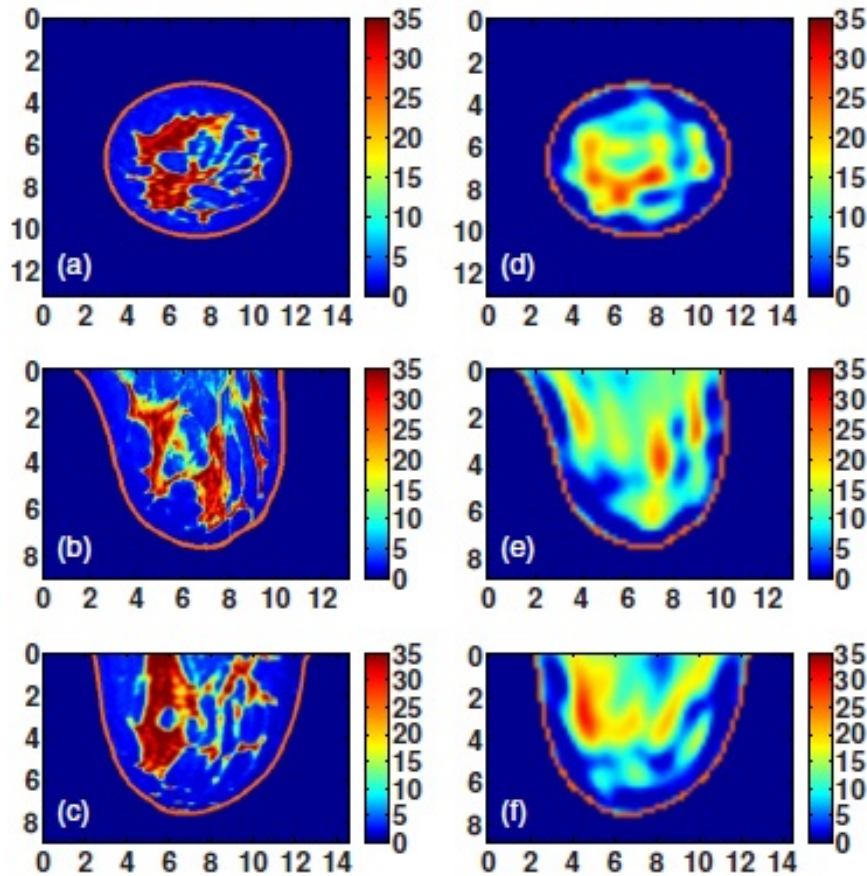
Figure 2.2: Class 3 phantom:(a)-(c) exact and (d)-(f) reconstructed profile of $\Delta\epsilon$ shown in coronal (x-y,top row), sagittal (y-z,middle row), and axial (x-z, bottom row) cross sections[18].

2.2 clearly show that the shape is not reconstructed well by using conjugate gradient method. Some important results of [35] are shown below. Figure 2.3 shows com-
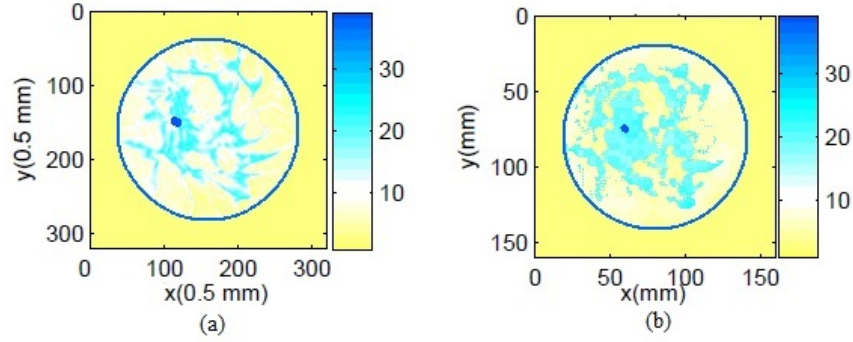
Figure 2.3: Comparison of permittivity profiles in less dense breast (a) Original permittivity profile (b) Reconstructed permittivity profile at the end of four stage algorithm [35]

parison of permittivity profiles in less dense breast. Figure 2.4 shows comparison
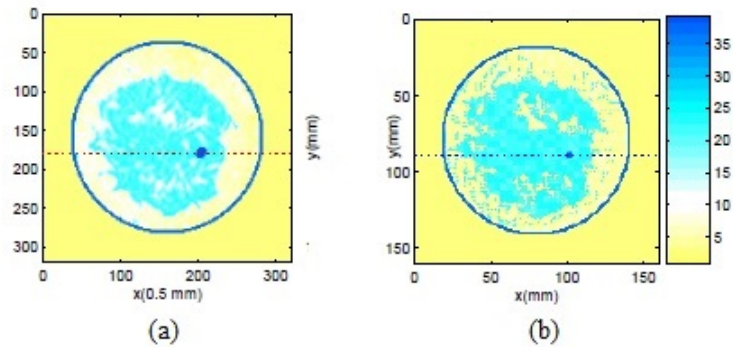
Figure 2.4: Comparison of permittivity profiles in high dense breast (a) Original permittivity profile (b) Reconstructed permittivity profile at the end of four stage algorithm [35]

of permittivity profiles in high dense breast. Figures 2.3 and 2.4 show promising results of level set based four stage inversion method [35]. Figure 2.5 shows original and reconstructed permittivity profiles when there is no tumour. Figure 2.6 shows original and reconstructed permittivity profiles when there are two tumours. Above results clearly show robustness of algorithm proposed in [35].

Colgan et al. have proposed 3D level set based optimization for microwave breast imaging in [36]. Breast density classification is proposed using single level set function. Level set based adjoint method requires two FDTD simulations per iteration.
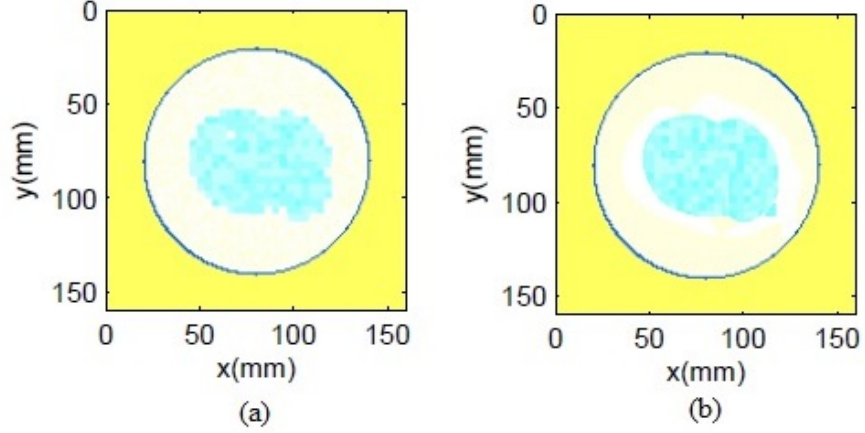
Figure 2.5: Comparison of permittivity profiles without tumour (a) Original permittivity profile (b) Reconstructed permittivity profile at the end of four stage algorithm [35]
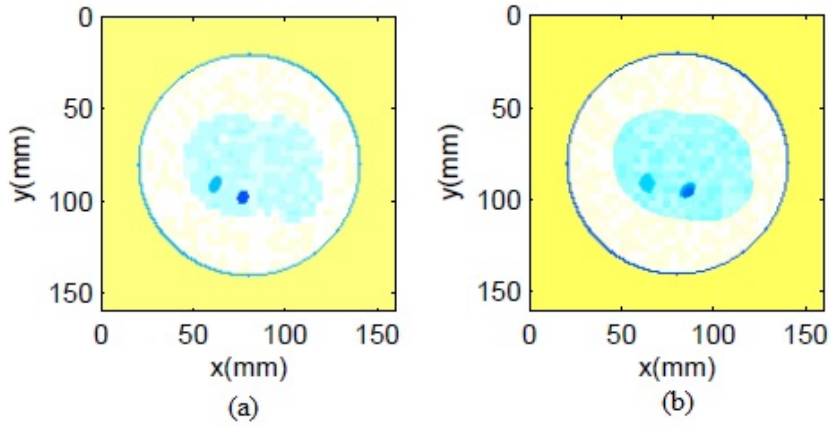
Figure 2.6: Comparison of permittivity profiles with two tumour (a) Original permittivity profile (b) Reconstructed permittivity profile at the end of four stage algorithm [35]

Level set method of [36] is computationally efficient as compared to adjoint method of Dorn et al. because it requires single FDTD simulation per iteration. Figure 2.7 shows promising results of level set based optimization by using single level set function [36]. Results of figure 2.7 clearly show that the performance of 3D level set optimization is better than 3D distorted born iterative method (DBIM).

Ping et al. have proposed modified Newton Raphson algorithm with regularization in [37]. Ping et al. have investigated initial guess, image iteration and optimal
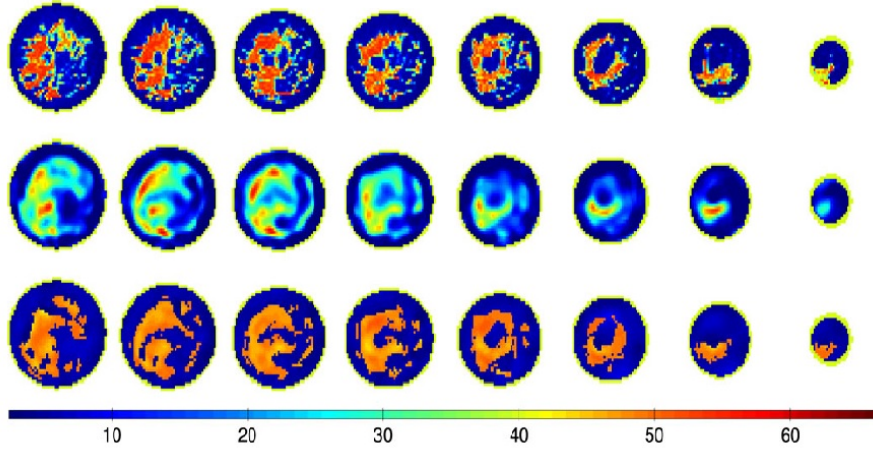
Figure 2.7: Coronal cross section of static permittivity profiles in class 3 breast phantom. Top row shows original permittivity profiles. middle row shows reconstructed permittivity profiles by using 3D Distorted born iterative method (DBIM). Bottom row shows reconstructed permittivity profiles by using 3D level set based optimization. The coronal cross sections are taken every 8 mm [36].

current updating factors in [37]. Prior-image induced nonlocal (PINL) regularization technique was proposed in [38] for statistical iterative reconstruction through the penalized weighted least-squares (PWLS). The PINL regularization uses the redundant information in the prior image. The weighted least-squares term considers a data-dependent variance estimation to improve low-dose image quality. A modified iterative algorithm is used to optimize objective function. Noise reduction, edge detail preservation and low-contrast object detection can be improved by using PWLS-PINL [38]. Tikhonov and total variation regularization methods are developed for ground penetrating radar signals in [39]. Regularization improves GPR signal range resolution in the presence of noise for thin asphalt overlay thickness prediction. Kozegar et al. have proposed computerized segmentation system by using 3D level set method and Gaussian mixture model in [40] which provides accurate automatic segmentation.

2.3 FDTD Method

Yee has proposed novel method to solve Maxwell's equations by using finite difference on discrete grid which is very well known as Yee grid [41]. Taflove has

proposed a numerical method to predict sinusoidal steady state of electromagnetic fields penetration in an arbitrary dielectric or conducting body by introducing lattice truncation conditions and loss factors [42]. Small air-dielectric loss factors are introduced to accelerate the sinusoidal steady state convergence of cavity interior fields. This method is evaluated by using experimental results via application to a dielectric sphere and a cylindrical metal cavity with an aperture. Results of missile-like cavity with two different types of apertures illuminated by an axial-incidence plane wave are also described in [42]. Okonievski et al. have proposed three simple and efficient algorithms to incorporate multi-term Debye or Lorentz dispersion in the FDTD method [43].

Hagness et al. have proposed time-gating and pulsed confocal techniques to enhance tumour detection by suppressing absorption and tissue heterogeneity effects in [44]. A two-dimensional FDTD analysis of the system is conducted by using published data for the dielectric properties of malignant tumors and normal breast tissues. The FDTD simulation results show that small tumours can be detected robustly in the presence of the background clutter. 2D FDTD analysis of the system provides promising results in [44]. Hagness et al. have proposed pulsed microwave confocal system by using 3D FDTD for breast cancer detection in [45]. They have used bowtie antenna element for breast cancer detection because of its sufficient dynamic range to detect small cancerous tumours usually missed by X-rays based mammography [45].

Bond et al. have proposed microwave imaging via space-time (MIST) beamforming for detecting early-stage breast cancer in [46]. An ultra wideband (UWB) signal is transmitted sequentially from each antenna of the array. Removal of artefacts present in the received signals is possible by this data-adaptive algorithm. The effectiveness of this algorithm is demonstrated by using a variety of MRI derived numerical breast phantoms. Malignant tumours embedded in the complex fibroglandular structure are easily detected in [46]. Li et al. have proposed experimental study of UWB antenna performance for dielectric contrast of malignant to normal breast tissues in [47]. Research work of Li et al. represents the first experimen-

tal demonstration of three dimensions MIST beam-forming for malignant-to-normal dielectric contrasts down to 1.5:1 with a synthetic tumour in multilayer breast phantoms.

Kosmas and Rappaport have proposed time reversal algorithm to detect breast cancer in [48]. Amplitude and phase information of the tumour response is used to get enough focusing. They have shown that the algorithm is robust to breast inhomogeneities. Guo et al. have proposed a new FDTD formulation using cole-cole model for electromagnetic wave propagation in dispersive biological tissues in [49]. Kosmas and Rappaport have proposed FDTD based time reversal algorithm for three dimensions in [50]. They have shown that the 3D algorithm based reconstructions are better than 2D algorithm based reconstructions. Kosmas and Rappaport have proposed a clutter dominated total signal processing using matched filter approach with FDTD based time reversal algorithm in [51]. Low complexity cole-cole model is used with FDTD for human tissues modelling by Kang et al. [52]. Gedney has proposed solution to FDTD lattice truncation problem by using an anisotropic perfectly matched layer (PML) absorbing medium in [53]. Schneider et al. has proposed FDTD equations which incorporate polarization and different types of dispersions [54]. Taflove and Hagness have proposed FDTD methods and parameters for different cases in [55].

Moll et al. have proposed computationally efficient and flexible ray tracing algorithm for micowave based tumour localization in moderate heterogeneous breast tissues in [56]. Easy tumour localization is possible using this proposed method [56]. Moll et al. have proposed a novel RADAR based beam-forming procedure by using 31 element array configuration and heterogeneous numerical breast phantom for microwave breast cancer detection in [57]. Yin et al. have proposed a novel adaptive combining through correlation exploration algorithm for breast cancer detection using UWB imaging in [58]. The performance of this algorithm is validated by using accurate 3D FDTD breast models. Song et al. have proposed UWB based microwave breast cancer detection system by using MRI derived realistic numerical breast phantom in [59]. Mirza et al. have implemented 1D, 2D and 3D FDTD nu-

merical methods for breast cancer detection in [60]. They have also discussed about best ways to identify the existence of cancerous tissues in the breast. Wang et al. have proposed microwave imaging system with wearable conformal antenna array for breast cancer detection in [61]. Tumour of size 5 mm diameter inside glandular region can be precisely located and detected by using FDTD solver of microwave studio in computer simulation technology (CST) [61]. Kwon et al. have proposed cost effective breast cancer imaging system with time domain measurements which can reconstruct breast image in the presence of white noise [62]. The above system can acquire images in short time so instantaneous microwave imaging is possible.

2.4   Method of Moments

Livesay et al. have proposed method of moment based procedure to calculate electric field inside arbitrary shaped biological body with approximate solution of green function integral in [63]. They have also found electric field inside fat and muscles tissues. Hohmann has proposed three dimensional induced polarization and electromagnetic modelling using method of moment in [64]. He had solved integral of green's function in three dimensions. Ghodgaonkar et al. have proposed complex permittivity reconstruction of 36 cell 3D human chest model with performance evaluation of surrounding medium in [65]. Cohoon has proposed computationally efficient solution of electromagnetic scattering integral equation through use of group theory in [66]. He has exploited symmetry by using group theory. Ghodgaonkar and Ismail have used symmetry exploitation in electromagnetic imaging by using group theory in [67].

Rubaek et al. have proposed an iterative Newton-based algorithm for reconstructing the images with method of moment in 3D microwave breast imaging system [68]. Zaeytijd et al. have proposed regularized gauss-newton method for three dimensional microwave imaging in [69]. A regularized cost function is proposed to mitigate the measurement noise effect on the reconstruction. Regularized cost function effectively deals with the non-linear optimization problem. The modified Gauss-Newton method converges much faster than the Broyden-Fletcher-Goldfarb-Shanno

(BFGS) quasi-Newton method with experimental and simulated data based quantitative reconstructions in [69]. Park et al. have developed hybrid algorithm based on Levenberg-Marquardt and genetic algorithms for microwave image reconstruction in [70]. The iterative inverse scattering technique (IIST) uses the finite element method (FEM) for calculating the electric fields and it uses hybrid (Levenberg-Marquardt and genetic) algorithm for minimizing the cost function. Numerical results show that the proposed hybrid algorithm can reconstruct the permittivity of the high contrast object, where as LMA alone can not reconstruct the desired permittivity. Numerical results also show that the quality and convergence of permittivity reconstruction by the hybrid algorithm is better than that of GA. [70]. Rubaek et al. have proposed Gauss-Newton's method and conjugate gradient least square (CGLS) inversion algorithms for non-linear microwave breast imaging in [71]. The proposed iterative CGLS algorithm can solve the update problem by using only Jacobian. To reconstruct images, this algorithm is taking fewer iterations than Tikhonov regularized Gauss-Newton method [71]. Fang et al. have proposed singular value analysis of the microwave imaging system Jacobian matrix in [72]. The results show significant ill-posedness reductions for increased signal frequency, property parameter sampling and antenna array density. The decay rate of Jacobian singular spectrum decreases with signal frequency and it is improved with 35 equally-spaced circumferentially positioned antenna array elements. These results are useful in design specifications development for an optimized hardware installation in [72].

Ney et al. have proposed Pseudo-inverse algorithm to reconstruct consecutive parameter distributions of infinitely long dielectric cylinders from the scattered field produced by them [73]. Pichot et al. have proposed numerical method for tomographic reconstruction of body with experimental technique by using diffraction phenomena in [74]. Spatial impulse response, simulated human arm, dielectric rods, isolated animal organs and inhomogeneous bodies examples are covered in [74]. Garnero et al. have proposed a novel iterative algorithm based on simulated annealing for quantitative reconstruction of the dielectric properties of strongly inhomogeneous object by active microwave imaging [75]. The performance of simulated annealing is more efficient than iterative deterministic methods in [75]. Belkebir et al. have

collected multiple frequency scattered fields data for reconstruction of location and shape of object by using Newton-Kantorovich (NK) and modified gradient methods in [76]. Caorsi et al. have solved two dimensional inverse scattering problem by using model driven approach and a priori information about biological tissues in [77]. The reconstruction of scatterers like living tissues and 2D TM mathematical formulation are shown in [77]. Pastorino has reviewed different stochastic methods for the solution of inverse scattering problems in [78]. Differential evolution methods, particle swarm optimizations, ant colony optimization, hybrid techniques, genetic algorithms and their use in electromagnetic are covered. Buried object detection, tomography and borehole sensing imaging modalities are also covered with the computational load reduction strategies in [78]. Andreuccetti et al. have provided dielectric properties of different human tissues for frequency range of 10 Hz-100 GHz in [79].

Meany et al. have build active microwave breast imaging clinical prototype in [83]. This prototype has 16-elements transceiver monopole antenna array which operates in the 300-1000 MHz frequency range. An examination of five women are done through a water-coupled interface to the pendant breast in prone position on an examination table. Full tomographic data acquisition is done at seven different array heights. Data collection starts at the chest wall and moving toward the nipple for seven different frequencies at each array position. This is the first clinical experience report of active near-field microwave imaging to exploit model-based image reconstructions in vivo. It appears that the average relative permittivity of the breast correlates with radiologic breast density classification in [83]. El-shenawee and Miller have proposed breast cancer tumour shape and location reconstruction algorithm by using microwave spherical harmonics in [84]. Spherical harmonic decomposition approach is used to capture the shape of the tumour. A direct electromagnetic solver is combined with gradient descent optimization method to determine the coefficients in the harmonics. The results show the advantage of multiple-view/tomographic-type strategy for data collection. This approach shows accurate tumour image reconstruction regardless of the source polarization. This algorithm is useful for Gaussian noise affected data in the absence of perfect knowledge about tumour electrical properties [84]. Donelli et al. have proposed modified particle swarm optimization for three

dimensional microwave imaging problems in [85]. The aim of this modified algorithm is to reduce both the dimension of search space and computational load of the optimization. The exploitation of particle swarm global search capabilities is favourable in the large-scale 3-D inverse scattering problems [85]. Single and multiple 3-D targets are used to assess this technique. Tong et al. have proposed reconstruction of dielectric objects Gauss-Newton minimization with line search and multiplicative regularization methods in [88]. Ahmadabadi et al. have proposed Fourier-Jacobi expansion of two dimensional inverse scattering problem for microwave imaging in [89].

References

[1] J.Ferlay, I.Soerjomataram, R.Dikshit, S.Eser, C.Mathers, M.Rebelo, D.M.Parkin, D.Forman, and F.Bray, "Cancer incidence and mortality worldwide: sources, methods and major patterns in GLOBOCAN 2012," International Journal of Cancer, Vol. 136, no. 5, pp. 359-386, March 2015.

[2] E.C.Fear, S.C.Hagness, P.M.Meaney, M.Okoniewski, M.A.Stuchly,"Enhancing breast Tumor detection with near field imaging" IEEE Microwave Magazine, Vol. 3, No. 1, pp. 48-56, 2002.

[3] E.C.Fear, P.M.Meaney, and M.A.Stuchly, "Microwaves for breast cancer detection," IEEE Potentials, Vol. 22, no. 1, pp. 12-18, 2003.

[4] A.M.Campbell, and D.V.Land, "Dielectric properties of female human breast tissue measured in vitro at 3.2 GHz," Physics in Medicine and Biology, Vol. 37, no. 1, pp. 193-210, 1992.

[5] M.Lazebnik, L.McCartney, D.Popovic, C.B.Watkins, M.J.Lindstrom, J.Harter, S.Sewall et al. "A large-scale study of the ultrawideband microwave dielectric properties of normal breast tissue obtained from reduction surgeries," Physics in Medicine and Biology, Vol. 52, no. 10, pp. 2637-2656, 2007.

[6] M.Lazebnik, L.McCartney, D.Popovic, C.B.Watkins, M.J.Lindstrom, J.Harter, S.Sewall et al. "A large-scale study of the ultrawideband microwave dielectric properties of normal, benign and malignant breast tissues obtained from cancer surgeries," Physics in Medicine and Biology, Vol. 52, no. 20, pp. 6093-6115, 2007.

[7] R.A.Jesinger "Breast Anatomy for the Interventionalist," Techniques in Vascular and Interventional Radiology, Elsevier, Vol. 17, no. 1, pp. 3-9, March 2014.

[8] D.Hanahan, R.A.Weinberg, "Hallmarks of Cancer: The Next Generation," Elsevier, Cell Press, Vol. 144, no. 5, pp. 646-674, March 2011.

[9] C.Zhou, H.Chan, N.Petrick, M.A.Helvie, M.M.Goodsitt, B.Sahiner, and L.M.Hadjiiski, "Computerized image analysis: estimation of breast density on mammograms," Medical Physics, Vol. 28, no. 6, pp. 1056-1069, 2001.

[10] P.M.Vacek, B.M.Geller, "A prospective study of breast cancer risk using routine mammographic breast density measurements," Cancer Epidemiology and Prevention Biomarkers, Vol. 13, no. 5, pp. 715-722, 2004.

[11] N.F.Boyd, G.A.Lockwood, J.W.Byng, D.L.Tritchler, and M.J.Yaffe, "Mammographic densities and breast cancer risk," Cancer Epidemiology and Prevention Biomarkers, Vol. 7, no. 12, pp. 1133-1144, 1998.

[12] C.M.Vachon, C.H.VanGils, T.A.Sellers, K.Ghosh, S.Pruthi, K.R.Brandt, and V.S.Pankratz, "Mammographic density, breast cancer risk and risk prediction," Breast Cancer Research, Vol. 9, no. 6, pp. 217-225, 2007.

[13] P.E.Freer,"Mammographic breast density: impact on breast cancer risk and implications for screening," Radiographics, Vol. 35, no. 2, pp. 302-315, 2015.

[14] H.D.Nelson, E.S.O'meara, K.Kerlikowske, S.Balch, and D.Miglioretti,"Factors Associated With Rates of False-Positive and False-Negative Results From Digital Mammography Screening: An Analysis of Registry Data False-Positive and False-Negative Digital Mammography Screening Results," Annals of Internal Medicine, Vol. 164, no. 4, pp. 226-235, 2016.

[15] E.Zastrow, S.K.Davis, M.Lazebnik, F.Kelcz, B.D.Van Veen, and S.C.Hagness, "Development of anatomically realistic numerical breast phantoms with accurate dielectric properties for modelling microwave interactions with the human breast," IEEE Transactions on Biomedical Engineering, Vol. 55, no. 12, pp. 2792-2800, 2008.

[16] M.Lazebnik, M.Okoniewski, J.H.Booske, and S.C.Hagness, "Highly accurate Debye models for normal and malignant breast tissue dielectric properties at mi-

crowave frequencies," IEEE Microwave and Wireless Components Letters, Vol. 17, no. 12, pp. 822-824, 2007.

[17] D.W.Winters, J.D.Shea, P.Kosmas, B.D.Van Veen, S.C.Hagness, "Three-dimensional microwave breast imaging: dispersive dielectric properties estimation using patient-specific basis functions," IEEE Transactions on Medical Imaging, Vol. 28, no. 7, pp. 969-981, July 2009.

[18] J.D.Shea, P.Kosmas, S.C.Hagness, and B.D. Van Veen, "Three-dimensional microwave imaging of realistic numerical breast phantoms via a multiple-frequency inverse scattering technique," Medical Physics, Vol. 37, no. 8, pp. 4210-4226, 2010.

[19] J.D.Garrett, E.C.Fear, "Average dielectric property analysis of complex breast tissue with microwave transmission measurements." Sensors 15, no. 1, pp. 1199-1216, 2015.

[20] D.Kurrant, J.Bourqui, C.Curtis, and E.C.Fear. "Evaluation of 3-D acquisition surfaces for radar-based microwave breast imaging." IEEE Transactions on Antennas and Propagation 63, no. 11, pp. 4910-4920, 2015.

[21] J.Bourqui, E.C.Fear. "System for bulk dielectric permittivity estimation of breast tissues at microwave frequencies." IEEE Transactions on Microwave Theory and Techniques 64, no. 9, pp. 3001-3009, 2016.

[22] S.Osher, J.A.Sethian, "Fronts propagating with curvature-dependent speed: algorithms based on Hamilton-Jacobi formulations,"Journal of Computational Physics, Vol. 79, pp. 12-49, 1988.

[23] S.Osher and R.Fedkiw, "Level set methods and dynamic implicit surfaces," Applied Mathematical Sciences, Springer-Verlag New York Inc, pp.1-142, 2003.

[24] F.Santosa, "A level-set approach for inverse problems involving obstacles," EASIM: Control, Optimization and Calculus of Variations, Vol. 1, pp. 17-33, January 1996.

[25] O.Dorn, E.L.Miller and C.M.Rappaport, "A shape reconstruction method for electromagnetic tomography using adjoint fields and level sets," Inverse Problems, Vol. 16, No. 5, October 2000.

[26] R.Ferraye, J.Y.Dauvignac, C.Pichot, "An inverse scattering method based on contour deformations by means of a level set method using frequency hopping technique," IEEE Transactions on Antennas and Propagation, Vol. 51, No. 5, pp.1100-1113, July 2003.

[27] M.Burger, "A level set method for inverse problems," Inverse Problems, Vol. 17, No. 5, August 2001.

[28] M.Burger, S.J.Osher, "A survey on level set methods for inverse problems and optimal design," European Journal of Applied Mathematics, Vol. 16, no. 2, pp. 263-301, April 2005.

[29] O.Dorn and D.Lesselier, "Level set methods for inverse scattering," Inverse Problems, Vol. 22, No. 4, pp. 1-79, June 2006.

[30] A.Aghasi, M.Kilmer, and E.L.Miller, "Parametric level set methods for inverse problems," SIAM Journal on Imaging Sciences, Vol. 4, No. 2, pp. 618-650, 2011.

[31] O.Semerci, E.L.Miller, "A parametric level-set approach to simultaneous object identification and background reconstruction for dual-energy computed tomography," IEEE Transactions on Image Processing, Vol. 21, No. 5, pp.2719-2734, February 2012.

[32] M.R.Eskandari, M.Dehmollaian, R.Safian, "Simultaneous microwave imaging and parameter estimation using modified level-set method," IEEE Transactions on Antennas and Propagation, Vol. 64, No. 8, pp. 3554-3564, June 2016.

[33] N.Irishina, O.Dorn, M.Miguel, "A level set evolution strategy in microwave imaging for early breast cancer detection," Computers & Mathematics with Applications, Elsevier, Vol. 56, No. 3, pp. 607-618, August 2008.

[34] N.Irishina, M.Moscoso, O.Dorn, "Microwave imaging for early breast cancer detection using a shape-based strategy," IEEE Transactions on Biomedical Engineering, Vol. 56, No. 4, pp. 1143-1153, January 2009.

[35] N.Irishina, "Microwave medical imaging using level set techniques," PhD Thesis, University of Carlos, Spain, 2009.

[36] T.J.Colgan, S.C.Hagness, and B.D.Van Veen, "A 3-D level set method for microwave breast imaging," IEEE Transactions on Biomedical Engineering, Vol. 62, no. 10, pp. 2526-2534, 2015.

[37] P.Hua, E.J.Woo, J.G.Webster, and W.J.Tompkins. "Iterative reconstruction methods using regularization and optimal current patterns in electrical impedance tomography," IEEE Transactions on Medical Imaging, Vol. 10, no. 4, pp. 621-628, 1991.

[38] H.Zhang, J.Huang, J.Ma, Z.Bian, Q.Feng, H.Lu, Z.Liang, and W.Chen. "Iterative reconstruction for X-ray computed tomography using prior-image induced nonlocal regularization," IEEE Transactions on Biomedical Engineering, Vol. 61, no. 9, pp. 2367-2378, 2014.

[39] S.Zhao and I.L.Al-Qadi. "Development of regularization methods on simulated ground-penetrating radar signals to predict thin asphalt overlay thickness," Signal Processing, Elsevier, Vol. 132, pp. 261-271, March 2017.

[40] E.Kozegar, M.Soryani, H.Behnam, M.Salamati, and T.Tan. "Mass Segmentation in Automated 3-D Breast Ultrasound Using Adaptive Region Growing and Supervised Edge-Based Deformable Model." IEEE transactions on medical imaging 37, no. 4, pp. 918-928, 2018.

[41] K.Yee, "Numerical solution of initial boundary value problems involving Maxwell's equations in isotropic media," IEEE Transactions on Antennas and Propagation, Vol. 14, no. 3, pp. 302-307, 1966.

[42] A.Taflove, "Application of the finite-difference time-domain method to sinu-

soidal steady-state electromagnetic-penetration problems," IEEE Transactions on Electromagnetic Compatibility, Vol. 22, no. 3, pp. 191-202, 1980.

[43] M.Okonievski, M.Mrozowski, and M.A.Stuchly, "Simple treatment of multi-term dispersion in FDTD", IEEE Microwave Guided Wave Letters, Vol. 7, pp. 121-123, 1997.

[44] S.C.Hagness, A.Taflove, and J.E.Bridges, "Two-dimensional FDTD analysis of a pulsed microwaved confocal system for breast cancer detection: fixed-focus and antenna-array sensors," IEEE Transactions on Antennas and Propagation, vol. 45, pp. 1470-1479, 1998.

[45] S.C.Hagness, A.Taflove, and J.E.Bridges,"Three-dimensional FDTD analysis of a pulsed microwaved confocal system for breast cancer detection: design of an antenna-array element," IEEE Transactions on Antennas and Propagation, Vol. 47, pp. 783-791, 1999.

[46] E.J.Bond, X.Li, S.C.Hagness, and B.D.Van Veen, "Microwave imaging via space-time beam-forming for early detection of breast cancer," IEEE Transactions on Antennas and Propagation, Vol. 51, no. 8, pp. 1690-1705, 2003.

[47] X.Li, S.K.Davis, S.C.Hagness, D.W.Van der Weide, and B.D.Van Veen, "Microwave imaging via space-time beam-forming: Experimental investigation of tumour detection in multilayer breast phantoms," IEEE Transactions on Microwave Theory and Techniques, Vol. 52, no. 8, pp. 1856-1865, 2004.

[48] P.Kosmas and C.Rappaport, "Time reversal with FDTD method for microwave breast cancer detection," IEEE Trans. Microwave Theory and Techniques, Vol. 53, pp. 2317-2322, 2005.

[49] B.Guo, L.Jian, and H.Zmuda, "A new FDTD formulation for wave propagation in biological media with Cole-Cole model," IEEE Microwave Wireless Component Letters, Vol. 16, pp. 633-635, 2006.

[50] P.Kosmas and C.Rappaport, "FDTD-basedtime reversal for microwave breast

cancer detection:Localization in three dimensions ," IEEE Transactions on Microwave Theory and Techniques, vol. 54, pp. 1921-1927, 2006.

[51] P.Kosmas and C.Rappaport, "A matched filter FDTD-based time reversal approach for microwave breast cancer detection ," IEEE Transactions on Antennas and Propagation, Vol. 54, pp. 1257-1264, 2006.

[52] K.Kang , X.Chu, R.Dilmaghani and M.Ghavami, "Low-complexity Cole-Cole expression for modelling human biological tissues in FDTD method," Electronic letters, Vol.43, no. 3, 2007.

[53] S.D.Gedney,"An anisotropic perfectly matched layer-absorbing medium for the truncation of FDTD lattices," IEEE Transactions on Antennas and Propagation, Vol. 44, no. 12, pp. 1630-1639, 1996

[54] J.B.Schneider, "Understanding the Finite-Difference Time-Domain Method," pp. 33-308, www.eecs.wsu.edu/ schneidj/ufdtd, 2010.

[55] A.Taflove, S.C.Hagness, "Computational Electrodynamics: The Finite-difference Time-domain Method," Boston, The Artech House, pp. 81-105, 2000.

[56] J.Moll, C.Bauer, and V.Krozer. "Microwave-based tumor localization in moderate heterogeneous breast tissue." In Radar Symposium (IRS), 2013 14th International, vol. 2, pp. 877-884. IEEE, 2013.

[57] J.Moll, M.Sarafianou, T.N.Kelly, V.Krozer, and I.J.Craddock. "Radar-based tumor localization in heterogeneous breast tissue using a 3D permittivity model." In Antennas and Propagation (EuCAP), 2014 8th European Conference, pp. 1288-1291. IEEE, 2014.

[58] T.Yin, and F.H.Ali. "Adaptive combining via correlation exploration for ultra-wideband breast cancer imaging." IEEE Antennas and Wireless Propagation Letters 14, pp.587-590, 2015.

[59] H.Song, X.Xiao, Z.Wang, and T.Kikkawa. "UWB microwave breast cancer detection with MRI-derived 3-D realistic numerical breast model." 2015 IEEE In-

ternational Symposium on Antennas and Propagation & USNC/URSI National Radio Science Meeting, pp. 544-545, 2015.

[60] A.F.Mirza, F.Abdulsalam, R.Asif, Y.A.S.Dama, M.M.Abusitta, F.Elmegri, R.A.Abd-Alhameed, James M. Noras, and Rami Qahwaji. "Breast Cancer Detection Using 1D, 2D, and 3D FDTD Numerical Methods." In Computer and Information Technology; Ubiquitous Computing and Communications; Dependable, Autonomic and Secure Computing; Pervasive Intelligence and Computing (CIT/IUCC/DASC/PICOM), 2015 IEEE International Conference on, pp. 1042-1045. IEEE, 2015.

[61] F.Wang, T.Arslan, G.Wang, "Breast cancer detection with microwave imaging system using wearable conformal antenna arrays." In Imaging Systems and Techniques (IST), 2017 IEEE International Conference on, pp. 1-6. IEEE, 2017.

[62] S.Kwon and S.Lee, "Instantaneous microwave imaging with time-domain measurements for breast cancer detection." Electronics Letters 49, no. 10, pp. 639-641, 2013.

[63] D.E.Livesay and K.Chen. "Electromagnetic fields induced inside arbitrarily shaped biological bodies," IEEE Transactions on Microwave Theory and Techniques, Vol. 22, no. 12, pp. 1273-1280, 1974.

[64] G.W.Hohmann, "Three dimensional induced polarization and electromagnetic modeling," Geophysics, vol. 40, no. 2, pp. 305-324, 1975.

[65] D.K.Ghodgaonkar, O.P.Gandhi and M.J.Hagmann, "Estimation of complex permittivities of 3D inhomogeneous biological bodies," IEEE Transactions on Microwave Theory and Techniques, Vol. 31, no. 6, pp. 442-446, 1983.

[66] D.K.Cohoon, "Reduction of the cost of solving an Integral Equation arising in electromagnetic scattering through the use of group theory," IEEE Transactions on Antennas and Propagation, Vol. 28, no. 1, pp. 104-107,January 1980.

[67] D.K.Ghodgaonkar and R.Ismail, "Exploiting Symmetry in Electromagnetic

Imaging Problems by using Group Representation Theory," Bull. Malaysian Math. Sc. Soc., Vol. 23 , no. 1, pp. 33-44, 2000.

[68] T.Rubaek, O.S.Kim, and P.Meincke, "Computational Validation of a 3-D Microwave Imaging System for Breast-Cancer Screening," IEEE Transactions on Antennas and Propagation, Vol. 57, no. 7, pp. 2105-2115, July 2009.

[69] J.D.Zaeytijd, A.Franchois, C.Eyraud, and J.Geffrin, "Full-Wave Three-Dimensional Microwave Imaging With a Regularized Gauss-Newton Method-Theory and Experiment," IEEE Transactions on Antennas and Wave Propagation, Vol. 55, no. 11, pp. 3279-3292, November 2007.

[70] C.S.Park, B.S.Jeong, "Reconstruction of a high contrast and large object by using the hybrid algorithm combining a Levenberg-Marquardt algorithm and a genetic algorithm," IEEE Transactions on Magnetics, Vol. 35, no. 3, pp. 1582-1585, May 1999.

[71] T.Rubaek, P.M.Meaney, P.Meincke, and K.D.Paulsen, "Nonlinear microwave imaging for breast-cancer screening using Gauss-Newton's method and the CGLS inversion algorithm," IEEE Transactions on Antennas and Propagation, Vol. 55, no. 8, pp. 2320-2331, August 2007.

[72] Q.Fang, P.M.Meaney, and K.D.Paulsen. "Singular value analysis of the Jacobian matrix in microwave image reconstruction," IEEE Transactions on Antennas and Propagation, Vol. 54, no. 8, pp. 2371-2380, 2006.

[73] M.M.Ney, A.M.Smith, S.S.Stuchly, "A Solution of Electromagnetic Imaging Using Pseudoinverse Transformation," IEEE Transactions on Medical Imaging, Vol.3 , Issue: 4, pp. 155-162, Dec 1984.

[74] C.Pichot, L.Jofre, G.Peronnet, J.Bolomey, "Active microwave imaging of Inhomogeneous bodies," IEEE Transactions on Antennas and Propagation, Vol. AP-33, No. 4, pp.416-425, April 1985.

[75] L.Garnero, A.Franchois, J.Hugonin, C.Pichot, and N.Joachimowicz, "Microwave Imaging complex permittivity reconstruction by simulated annealing," IEEE

Transaction on Microwave Theory and Techniques, Vol. 39, No. 11, pp.1801-1807, November 1991.

[76] K.Belkebir, R.E.Kleinman, and C.Pichot, "Microwave Imaging Location and Shape Reconstruction from Multifrequency Scattering Data," IEEE Transaction on microwave theory and techniques, Vol.45, No. 4, pp. 469-476, April 1997.

[77] S.Caorsi, G.L.Gragnani, M.Pastorino, and Mauro Rebagliati, "A Model driven approach to microwave diagnostics in biomedical applications," IEEE Transactions on Microwave Theory and Techniques, Vol.44, No.10, October 1996.

[78] M.Pastorino, "Stochastic Optimization Methods Applied to Microwave Imaging:A Review," IEEE Transactions on Antennas and Propagation, Vol.55, No.3, pp.538-548, March 2007.

[79] D.Andreuccetti, R.Fossi and C.Petrucci: An Internet resource for the calculation of the dielectric properties of body tissues in the frequency range 10 Hz - 100 GHz. Website at http://niremf.ifac.cnr.it/tissprop/. IFAC-CNR, Florence (Italy), 1997. Based on data published by C.Gabriel et al. in 1996.

[80] R.F.Harrington, Field Computation by Moment Methods, New York, IEEE Press, pp.1-79, 1993.

[81] D.M.Pozar, Microwave Engineering, New York, John Wiley and sons, pp.1-243,547-593, 1989.

[82] S.A.Dianat, E.S.Saber, Advanced Linear Algebra for Engineers with MATLAB, CRC Press, pp. 1-302, 2009.

[83] P.M.Meaney, M.W.Fanning, D.Li, S.P.Poplack, and K.D.Paulsen, "A Clinical Prototype for Active Microwave Imaging of the Breast," IEEE Transactions on Microwave Theory and Techniques, Vol. 48, NO. 11, pp.1841-1853, November 2000.

[84] M.El-Shenawee, E.L.Miller, "Spherical Harmonics Microwave Algorithm for Shape and Location Reconstruction of Breast Cancer Tumor," IEEE Transactions On Medical Imaging, Vol. 25, NO. 10, pp. 1258-1271, October 2006.

[85] M.Donelli, D.Franceschini, P.Rocca, and A.Massa, "Three-Dimensional Microwave Imaging Problems Solved Through an Efficient Multiscaling Particle Swarm Optimization," IEEE Transactions on Geoscience and Remote Sensing, Vol. 47, No. 5, pp.1467-1481 May 2009.

[86] C.L.Epstein, "Introduction to the Mathematics of Medical Imaging," Society for Industrial and Applied Mathematics, pp.337-404, 2008.

[87] J.L.Mueller, S.Siltanen, "Linear and Nonlinear Inverse Problems with Practical Applications," Society for Industrial and Applied Mathematics, pp.111-221, 2012.

[88] M.S.Tong, K.Yang, W.Tian.Sheng, and Z.Y.Zhu. "Efficient reconstruction of dielectric objects based on integral equation approach with Gauss-Newton minimization." IEEE Transactions on Image Processing 22, no. 12, pp. 4930-4937, 2013.

[89] H.Ahmadabadi and K.Forooraghi, "Application of Fourier-Jacobi Expansion to Inverse Scattering Problem." IEEE Antennas and Wireless Propagation Letters 16, 956-959, 2017.

Chapter 3

Multiple Frequency Inverse Scattering Problem Formulation

3.1 Introduction

Multiple frequency inclusion in the inverse scattering problem improves computational efficiency and accuracy of microwave imaging system. Numerical breast phantom, Antenna placement and Debye model are required for multiple frequency inverse scattering problem formulation. Numerical breast phantom and antenna placement are given in appendix A for breast cancer detection system. Zastrow et al. have developed anatomically realistic numerical breast phantom with accurate dielectric properties in [1]. Debye model is used to model polarization and dispersion properties of human breast tissues. Derivation of Debye model is given in appendix B1. Lazebnik et al. have developed highly accurate Debye models for normal and malignant breast tissue dielectric properties in 0.5 to 20 GHz frequency range [2]. Experimental approximation of human breast tissue properties by using improved Debye model is proposed by Khuda et al in [3]. Average dielectric property analysis and bulk dielectric permittivity estimation for breast tissues are given in [4] and [5] respectively. Winters et al. have proposed multiple frequency inverse scattering problem in [6]. Shea et al. have also used multiple frequency inverse scattering problem formulation of winters et al. in [7]. Irishina has proposed antenna placement for 2D microwave breast imaging system in [8]. Colgan et al. have used multiple frequency inverse scattering problem formulation for 3D level set technique in [9]. Our work on multiple frequency inverse scattering problem formulation is described

in [10, 11, 12].

3.2   Problem Formulation

Multiple frequency inverse scattering problem formulation for human breast tissues requires Debye model. Debye model is incorporated in the system of scattered field equations. Antenna placement surrounding breast of appendix A.2 is used to formulate multiple frequency inverse scattering problem. Scattered fields at antenna locations are calculated by using equation (3.1).

$$\vec{E}^s(\vec{r}) = \iiint G(\vec{r}, \vec{r'}) \cdot \vec{J}(\vec{r'}) dv' \tag{3.1}$$

In equation (3.1), $\vec{E}^s(\vec{r})$ is scattered electric field at antenna locations $\vec{r}$, Green's function of homogeneous background medium is $G(\vec{r}, \vec{r'})$, and $\vec{J}(\vec{r'})$ is polarization current density. Equation (3.2) is obtained by substituting polarization current density into equation (3.1).

$$\vec{E}^s(\vec{r}) = \omega^2 \mu \iiint G(\vec{r}, \vec{r'}) \cdot \vec{E}_t(\vec{r'}) [\epsilon(\vec{r'}) - \epsilon^b(\vec{r})] dr' \tag{3.2}$$

In equation (3.2), $\epsilon(\vec{r'}) - \epsilon^b(\vec{r})$ is contrast in permittivity with respect to homogeneous background medium, $\vec{E}_t(\vec{r'})$ is total electric field intensity at location $\vec{r'}$. Single pole Debye model of equation (3.3) is substituted in equation (3.2).

$$\epsilon(\omega) = \epsilon_\infty + \frac{\Delta\epsilon}{1 + j\omega\tau} + \frac{\sigma_s}{j\omega\epsilon_0} \tag{3.3}$$

In equation 3.3, ϵ_∞ is infinite frequency permittivity, $\Delta\epsilon$ is difference between static permittivity (ϵ_s) and infinite frequency permittivity (ϵ_∞), and σ_s is static conductivity. τ is relaxation time constant with 15ps value for all breast tissues. Relaxation time constant is assumed to be spatially invariant. Approximation of equation (3.2) is obtained by using procedure of [6, 7]. Numerical breast phantom is represented by K voxels after discretization. There are 40 antennas surrounding breast as shown in appendix A.2. Each antenna works as transceiver. One antenna transmits microwave signal on breast and other antennas receive scattered microwave signal due to differ-

ent breast tissues. This process is repeated for each antenna present in the system. Let us consider there are N antennas in the system. F is number of frequencies. Ideally there are N^2F measurements possible. There are only $M = (N(N-1)/2)F$ measurements possible after removing redundancy. There are N-1 receivers when first antenna transmits. There are N-2 receivers when second antenna transmits. By this way, there are channels among transmitters and receivers. By considering, N antennas, M number of channels, F number of frequencies, and K voxels equation (3.4) is obtained from equation (3.2).

$$
\begin{bmatrix}
Re(A_1^\infty) & Re(A_1^\Delta) & Re(A_1^\sigma) \\
Im(A_1^\infty) & Im(A_1^\Delta) & Im(A_1^\sigma) \\
& . & \\
& . & \\
& . & \\
Re(A_M^\infty) & Re(A_M^\Delta) & Re(A_M^\sigma) \\
Im(A_M^\infty) & Im(A_M^\Delta) & Im(A_M^\sigma)
\end{bmatrix}
\begin{bmatrix}
\delta(\epsilon_\infty) \\
\delta(\Delta\epsilon) \\
\delta(\sigma_s)
\end{bmatrix}
=
\begin{bmatrix}
Re(E_1^s) \\
Im(E_1^s) \\
. \\
. \\
. \\
Re(E_M^s) \\
Im(E_M^s)
\end{bmatrix}
\tag{3.4}
$$

In equation (3.4), $\delta(\epsilon_\infty) = (\epsilon_\infty)_k - (\epsilon_\infty)_b$, is difference between kth voxel's infinite frequency permittivity and background medium's infinite frequency permittivity, $\delta(\Delta\epsilon) = (\Delta\epsilon)_k - (\Delta\epsilon)_b$ and $\delta(\sigma_s) = (\sigma_s)_k - (\sigma_s)_b$ are defined same as above. Re(.) and Im(.) represent real part and imaginary part respectively. By comparing equation (3.4) with $A\epsilon = b$, Sizes of A, ϵ and b are $2MF \times 3K$, $3K \times 1$ and $2MF \times 1$ respectively. There are total 2MF equations, and 3K unknowns. Let's consider an example with 40 antennas, 18 frequencies, and 64000 voxels. There are 28,080 equations and 192000 unknowns in our system. It means this approximated linear system of equation (3.4) is under-determined. In equation (3.4), each element of matrix A is represented by equation (3.5) and Scattered fields column vector of right hand side is given by equation (3.6). In equation (3.5), $a_k^p(\omega_1) = \omega_1^2\mu\epsilon_0 \cdot E_y^t(\vec{r}_j|\vec{r}_m, \omega_1) \cdot IG_y(\vec{r}_n|\vec{r}_j, \omega_1)$ and $C_\infty(\omega) = 1$, $C_\Delta(\omega) = (1 + j\omega\tau)^{-1}$, $C_\sigma(\omega) = (j\omega\epsilon_0)^{-1}$. $E_y^t(\vec{r}_j|\vec{r}_m, \omega_l)$ is y direction electric field present at j^{th} voxel location due to transmitter at location $\vec{r}_m$ for angular frequency ω_l, $IG_y(\vec{r}_n|\vec{r}_j, \omega_l)$ is y direction component of the integration of the green's function

at angular frequency ω_l. Where, $\vec{r}_n$, p and k represent receiver location, particular channel number and total number of voxels respectively. Scattered electric field matrix of equation (3.4) is known due to forward simulation. Left hand side matrix A of equation (3.4) is also known. Permittivity contrast profile column matrix is only unknown in equation (3.4).

$$
A_p^e = \begin{bmatrix} C_e(\omega_1)[a_1^p(\omega_1)\ldots\ldots a_k^p(\omega_1)] \\ \cdot \\ \cdot \\ \cdot \\ C_e(\omega_F)[a_1^p(\omega_F)\ldots\ldots a_k^p(\omega_F)] \end{bmatrix}
\tag{3.5}
$$

$$
E_p^s = \begin{bmatrix} E_y^t(\vec{r}_n|\vec{r}_m,\omega_1) - E_y^i(\vec{r}_n|\vec{r}_m,\omega_1) \\ \cdot \\ \cdot \\ \cdot \\ E_y^t(\vec{r}_n|\vec{r}_m,\omega_F) - E_y^i(\vec{r}_n|\vec{r}_m,\omega_F) \end{bmatrix}
\tag{3.6}
$$

$$
C(\epsilon) = \frac{1}{2} \sum_{f=1}^{F} \sum_{n=1}^{M} |E_m^s(\vec{r}_n,\omega_f) - E_r^s(\vec{r}_n,\omega_f,\epsilon(\vec{r}'))|^2
\tag{3.7}
$$

In equation (3.7), $C(\epsilon)$ is cost function, $E_m^s(\vec{r}_n,\omega_f)$ is known scattered field (measured) at location $\vec{r}_n$ for frequency ω_f, $E_r^s(\vec{r}_n,\omega_f,\epsilon(\vec{r}'))$ is reconstructed scattered field at location $\vec{r}_n$ for frequency ω_f and dielectric profile $\epsilon(\vec{r}')$, F is the number of frequencies, M is the number of measurements (channels), $\vec{r}_n$ is receiver location, ω_f is angular frequency. Now, cost function is represented in residual form by using eqaution (3.8).

$$
C(\epsilon) = \frac{1}{2} \sum_{i=1}^{FM} |R_i|^2
\tag{3.8}
$$

The cost function of equation (3.8) is minimized in the next chapter. Sample code for inverse scattering matrix formulation is given in appendix C.1.

References

[1] E.Zastrow, S.K.Davis, M.Lazebnik, F.Kelcz, B.D.Van Veen, and S.C.Hagness, "Development of anatomically realistic numerical breast phantoms with accurate dielectric properties for modelling microwave interactions with the human breast," IEEE Transactions on Biomedical Engineering, Vol. 55, no. 12, pp. 2792-2800, 2008.

[2] M.Lazebnik, M.Okoniewski, J.H.Booske, and S.C.Hagness, "Highly accurate Debye models for normal and malignant breast tissue dielectric properties at microwave frequencies," IEEE Microwave and Wireless Components Letters, Vol. 17, no. 12, pp. 822-824, 2007.

[3] I.Khuda, S.Khatun, K.J.Reza, M.M.Rahman, M.M.Fakir, "Improved Debye Model for Experimental Approximation of Human Breast Tissue Properties at 6 GHz Ultra-Wideband Centre Frequency", International Journal of Engineering and Technology, Vol. 5, no. 6, pp. 4708-4717, 2013.

[4] J.D.Garrett, E.C.Fear, "Average dielectric property analysis of complex breast tissue with microwave transmission measurements." Sensors 15, no. 1, pp. 1199-1216, 2015.

[5] J.Bourqui, E.C.Fear, "System for bulk dielectric permittivity estimation of breast tissues at microwave frequencies." IEEE Transactions on Microwave Theory and Techniques 64, no. 9, pp. 3001-3009, 2016.

[6] D.W.Winters, J.D.Shea, P.Kosmas, B.D.Van Veen, S.C.Hagness, "Three-dimensional microwave breast imaging: dispersive dielectric properties estimation using patient-specific basis functions," IEEE Transactions on Medical Imaging, Vol. 28, no. 7, pp. 969-981, July 2009.

[7] J.D.Shea, P.Kosmas, S.C.Hagness, and B.D. Van Veen, "Three-dimensional microwave imaging of realistic numerical breast phantoms via a multiple-frequency inverse scattering technique," Medical Physics, Vol. 37, no. 8, pp. 4210-4226, 2010.

[8] N.Irishina, "Microwave medical imaging using level set techniques," PhD Thesis, University of Carlos, Spain, 2009.

[9] T.J.Colgan, S.C.Hagness, and B.D.Van Veen, "A 3-D level set method for microwave breast imaging," IEEE Transactions on Biomedical Engineering, Vol. 62, no. 10, pp. 2526-2534, 2015.

[10] H.N.Patel and D.K.Ghodgaonkar, "Study of effect of numerical breast phantom heterogeneity on dielectric profile reconstruction using microwave imaging," Progress In Electromagnetics Research M, Vol. 58, pp. 135-145, 2017.

[11] H.N.Patel and D.K.Ghodgaonkar,"3D level set based optimization of inverse scattering problem for microwave breast imaging", IEEE MTT-S International Microwave Bio Conference, 15-17 May 2017, Gothenburg, Sweden, pp. 1-4.

[12] H.N.Patel and D.K.Ghodgaonkar, "Application of 3D level set based optimization in microwave breast imaging for cancer detection" accepted in Level Set Method in Medical Imaging Segmentation, Boca Raton:Fl, USA, CRC Press.

Chapter 4

3D Level Set based Optimization

3D Level set based optimization provides better shape and dielectric properties reconstruction for microwave breast imaging. Shape reconstruction does not involve in most of the traditional optimization techniques. This limitation has been avoided by using 3D level set functions. Novel 3D level set based optimization is used to reconstruct dielectric properties as well as shape of breast images. Debye parameter values and 3D level set functions are updated to minimize cost function. Ill posed system matrix and noisy scattered fields data make 3D reconstruction very challenging. Regularization is used to overcome above challenges.

First time, level set method was proposed by Osher and Sethian as propagating fronts for Hamilton-Jacobi formulations in 1988 [1]. Osher and Fedkiw have proposed level set methods for different applications in [2]. Santosa has proposed novel level set based evolution and optimization approaches for inverse problems in [3]. Single 3D level set function based breast classification is implemented by colgan et al. in [4]. Classical reviews on level set methods for inverse problems are described in [5, 6, 7].

4.1 Theoretical Foundations

Evolution and optimization approaches are discussed in [3]. F is characteristic set of interest and its boundary is described by a function $\phi(r)$.

$$\partial F = \{r : \phi(r) = 0\} \tag{4.1}$$

A sequence of functions $\phi_k(r)$ is generated by using level set approach such that

$$F_k = F \tag{4.2}$$

In inverse scattering problem, complex permittivity is reconstructed. Consider ϵ as the unknown parameter. Relationship of $\phi(r)$ with ϵ is given by equation (4.3).

$$\epsilon(r) = \begin{cases} \epsilon_{int} & \text{for} \quad \{r : \phi(r) < 0\} \\ \epsilon_{ext} & \text{for} \quad \{r : \phi(r) > 0\} \end{cases} \tag{4.3}$$

In equation (4.3), $\epsilon(r) = \epsilon_{int}$ whenever function $\phi(r)$ is negative, $\epsilon(r) = \epsilon_{ext}$ whenever function $\phi(r)$ is positive. Advantages of representing ϵ as function $\phi(r)$ are given below.

- Priori assumptions about the topology of F are not needed. F may be made up of several disconnected subregions. F may be multiple times connected.

- Priori assumptions about the nature of F are not needed.

Representation of equation (4.3) makes linear inverse problem non-linear due to dependence of ϵ on ϕ. In equation (4.3), find $\phi(r)$ such that $A\epsilon = b$, where A and b are known. If $\phi(r)$ is changed by a small variations $\delta\phi(r)$ then r is changed by δr. This variation results in the new region denoted by F'. If variation of the equation $\phi(r)$ is equal to 0, then

$$\delta\phi + \nabla\phi \cdot \delta r = 0 \tag{4.4}$$

In figure 4.1, the unit outward normal at r is given by equation (4.5).

$$n(r) = \frac{\nabla\phi(r)}{|\nabla\phi(r)|} \tag{4.5}$$

The inner product of $\delta\epsilon$ with a test function g(x) is given by equation (4.6).

$$< \delta\epsilon, g > := \int_{R^2} \delta\epsilon(r)g(r)dr = \int_{F\cap F'} \delta\epsilon(r)g(r)dr \tag{4.6}$$

The value of $\delta\epsilon(r)$ is equal to $\epsilon_{int} - \epsilon_{ext}$ with plus or minus sign. Inner product is
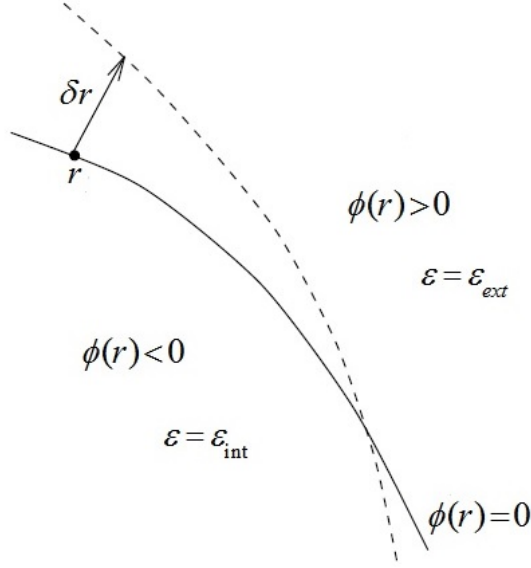
Figure 4.1: The variations of the curve $r : \phi(r) = 0$ under variation $\delta\phi(r)$.

simplified to equation (4.7) for infinitesimal $\delta\epsilon$.

$$< \delta\epsilon, g >:= \int_{\partial F} (\epsilon_{int} - \epsilon_{ext})\delta r \cdot n(r)g(r)ds(r) \tag{4.7}$$

where ds(r) is the incremental arc length. $\delta\epsilon$ is given by equation (4.8).

$$\delta\epsilon = (\epsilon_{int} - \epsilon_{ext})\frac{\nabla\phi(r)}{|\nabla\phi(r)|} \cdot \delta r \tag{4.8}$$

The dot product in above equation includes correct sign for $\delta\epsilon$. $\delta\epsilon$ will have same sign as $(\epsilon_{int} - \epsilon_{ext})$ at the point r. The opposite sign will be there if the normal component of δr is in the opposite direction of the normal.

4.1.1 Evolution Approach

In this approach, evolution equation for $\phi(r)$ is derived to solve inverse obstacle problem. The evolution equation will have property that as time t tends to infinity function $\phi(r)$ is evolved such that the associated $\epsilon(r)$ is the solution to the inverse problem. If t represent time, then level set function ϕ depends on both r and t.

$$\partial F(t) = \{r : \phi(r, t) = 0\} \tag{4.9}$$

Therefore, an evolving region is associated with $\phi(r, t)$. The cost function of equation (4.10) is to be minimized in least square sense.

$$C(\epsilon) = \frac{1}{2}\|A\epsilon - b\|_2^2 \tag{4.10}$$

The minimal requirement for the variation of $\phi(r, t)$ is that $C(\epsilon)$ be a decreasing function of t. Let's assume that each point r$\in \partial F(t)$ moves perpendicular to the surface. The variation of δr satisfies equation (4.11).

$$\delta r = \beta(r, t)\frac{\nabla \phi}{|\nabla \phi|} \tag{4.11}$$

In equation (4.11), $\beta(r, t)$ is viewed as the velocity of the surface at r. Equation (4.12) is obtained by substituting equation (4.11) into equation (4.8).

$$\delta\epsilon = (\epsilon_{int} - \epsilon_{ext})\beta(r, t) \tag{4.12}$$

The directional derivative of the function $C(\epsilon)$ in the direction $\delta\epsilon$ is given by

$$\delta C(\epsilon) = <J^T(\epsilon)(A\epsilon - b), \delta\epsilon> \tag{4.13}$$

Where $J(\epsilon)$ is Jacobian of $A\epsilon$ at ϵ. Equation (4.14) is obtained by substituting equation (4.12) into equation (4.13).

$$\delta C(\epsilon) = \int_{\partial F(t)} [J^T(\epsilon)(A\epsilon - b)](\epsilon_{int} - \epsilon_{ext})\beta(r, t)ds(r) \tag{4.14}$$

Assuming that $\epsilon_{int} > \epsilon_{ext}$, Natural choice of $\beta(r, t)$ is given by equation (4.15).

$$\beta(r, t) = -J^T(\epsilon)(A\epsilon - b) \tag{4.15}$$

Equation (4.16) for $\delta\phi(x, t)$ is determined by using equations (4.4) and (4.11).

$$\delta\phi = -\nabla\phi \cdot \delta r = -\nabla\phi \cdot (\beta(r, t)\frac{\nabla \phi}{|\nabla \phi|}) = -\beta(r, t)|\nabla \phi| \tag{4.16}$$

Any $\beta(r, t)$ satisfying equation (4.15) produce $\delta\phi$ which will reduce $C(\epsilon)$. This leads to equation of $\delta\phi$.

$$\delta\phi = [J^T(\epsilon)(A\epsilon - b)]|\nabla\phi| \tag{4.17}$$

This initial value problem for $\phi(r, t)$ is a hamilton-jacobi system as shown by equations (4.18) and (4.19).

$$\frac{\partial\phi}{\partial t} = [J^T(\epsilon)(A\epsilon - b)]|\nabla\phi| \tag{4.18}$$

$$\phi(r, 0) = \phi_0(r) \tag{4.19}$$

It is observed that evolutionary approach has following characteristics.

1. The evolution is such that $C(\epsilon)$ is non-increasing; that is $\frac{\partial}{\partial t}C(\epsilon) \leq 0$.

2. If a solution ϵ exists, then at the solution $A\epsilon = b$, so that $\frac{\partial\phi}{\partial t} = 0$ at the solution.

3. It can be viewed as the evolution in the steepest descent direction for the residual of $C(\epsilon)$

This evolution approach can be used to find solution of inverse problems.

4.1.2   Optimization Approach

In the optimization approach, sequence of surfaces $\phi_k(r)$ whose associated function $\epsilon(r)$ represent descent directions for the functional $C(\epsilon)$. It is convenient to use notation given below for this purpose.

$$\partial F_k = \{r : \phi_k(r) = 0\} \tag{4.20}$$

Consider $\phi_k(r)$ as an initial point in this approach. An update $\delta\phi(r)$ is needed to generate $\phi_{k+1}(r)$. Gauss-Newton approach is used to minimize $C(\epsilon)$. The descent update is given by $\delta\epsilon'$, where

$$J^T(\epsilon)J(\epsilon)\delta\epsilon' = J^T(\epsilon)(b - A\epsilon) \tag{4.21}$$

Equation (4.21) is an update for ϵ. Now our task is to find the associated update for ϕ. Equation (4.12) is rewritten as follows.

$$\delta\epsilon = (\epsilon_{int} - \epsilon_{ext})\beta(r) \tag{4.22}$$

For $\delta\epsilon'$, equation (4.22) can be written as equation (4.23)

$$\delta\epsilon' = (\epsilon_{int} - \epsilon_{ext})\beta(r) \tag{4.23}$$

Equation (4.24) can be obtained by rearranging equation (4.23).

$$\beta(r) = \frac{\delta\epsilon'}{(\epsilon_{int} - \epsilon_{ext})} \tag{4.24}$$

The natural choice for $\beta(r)$ is to extend the above relation to all points on R^3. Update for $\delta\phi(r)$ is given by equation (4.25).

$$\delta\phi(r) = -\frac{\delta\epsilon'}{(\epsilon_{int} - \epsilon_{ext})}|\nabla\phi_k(r)| \tag{4.25}$$

It can be shown that this is the descent direction for $C(\epsilon)$. Equation (4.24) is substituted in equation (4.14) to get .

$$\delta C(\epsilon) = -\int_{\partial F_k}[J^T(\epsilon)(A\epsilon - b)]\delta\epsilon' ds(r) \tag{4.26}$$

Equation (4.27) is obtained by substituting $\delta\epsilon'$ value of equation (4.21) in equation (4.26).

$$\delta C(\epsilon) = -\int_{\partial F_k}[J^T(\epsilon)(A\epsilon - b)][J^T(\epsilon)J(\epsilon)]^{-1}J^T(\epsilon)(b - A\epsilon)ds(r) \tag{4.27}$$

Above equation is negative if $J^T(\epsilon)J(\epsilon) > 0$. Therefore, the variation $\delta\phi(r)$ corresponds to a variation in $C(\epsilon)$ that is negative. Gauss-Newton algorithm for the inverse problem is given below.

1. Choose $\phi_0(r)$; set $k = 0$.

2. Compute associated ϵ; if $C(\epsilon) >$ tolerance, do

(i). Compute $J(\epsilon)^T J(\epsilon)\delta\epsilon' = J^T(\epsilon)(b - A\epsilon)$.

(ii). Compute $\delta\phi(r) = -\frac{\delta\epsilon'}{(\epsilon_{int} - \epsilon_{ext})}|\nabla\phi_k(r)|$.

(iii). Set k = k+1, update $\phi_{k+1}(r) = \phi_k(r) + \delta\phi(r)$.

This algorithm is implemented to find solution of inverse problem.

4.2 Single 3D Level Set Function based Optimization

Single 3D level set function based optimization is described in [4]. Reviews of level set methods for different types of inverse problems are described in [5, 6, 7]. Electromagnetic tomography for shape reconstruction is proposed by using adjoint and level set methods in [8]. Contour deformation based inverse scattering method using frequency hopping technique is given in [9]. Parametric level set method for inverse problems is described in [10, 11]. Modified level set method (MLSM) for simultaneous microwave imaging and parameter estimation is given in [12]. Single level set function is shown in figure 4.2. Figure 4.2 shows level set function which distinguish two different regions in 2D. Scenario of figure 4.2 is given as an equation.

Figure 4.2: Level set function to distinguish two different regions

$$\epsilon(r) = \epsilon^{fib}(r)H(\phi(r)) + \epsilon^{fat}(r)(1 - H(\phi(r))) \qquad (4.28)$$

In equation (4.28), $\phi(r)$ is level set function, H($\cdot$) is the unit step function, ϵ^{fib} is the complex permittivity of the fibro-glandular tissues, ϵ^{fat} is the complex permittivity of the fatty tissues. Region $\phi > 0$ is represented by $H(\phi)$ and region $\phi \leq 0$ is represented by $1 - H(\phi)$. Equations (4.29) and (4.30) represent linear relationships among Debye parameters [4].

$$\epsilon_\infty = 0.3265\epsilon_s + 1.6326 \qquad (4.29)$$

$$\sigma_s = 0.0151\epsilon_s - 0.0365 \qquad (4.30)$$

Above equations are used to reduce number of unknowns per voxel. Now, cost function of equation (3.8) is minimized in level set based optimization. The adjoint solution of level set optimization is computationally heavy. This computational cost is avoided by calculating jacobian matrix. The jacobian matrix of cost function equation (3.8) is calculated using equation (4.31) [4].

$$G_r(r|r') \circ E_r^t(r') = J(\epsilon) \qquad (4.31)$$

In equation (4.31), $G_r(r|r')$ is the MF×K green's function matrix, $E_r^t(r')$ is the MF×K total field matrix. Where M, F and K are number of measurements, number of frequencies and number of voxels respectively. The Jacobian matrix is element by element product of green's function matrix and total field matrix. Each row of the Jacobian matrix is the frechet derivative of the residuals with respect to complex permittivity ϵ. Green function calculations are given in [4, 13, 14]. The frechet derivative of the cost function is calculated by using equation (4.32) [4].

$$\nabla C(\epsilon) = J^T(\epsilon)R(\epsilon) \qquad (4.32)$$

In equation (4.32), Size of $J^T(\epsilon)$ is K×MF and size of residual is MF×1. The size of partial derivative of cost function with respect to ϵ is K×1. This method of calculating frechet derivative reduces computational complexity as compared to adjoint method [4, 8]. Only single FDTD simulation is required at every iteration in this method. Therefore, it reduces computational burden by half at every iteration. The partial derivative of equation (4.28) with respect to ϕ is computed by using equation (4.33) [4].

$$\frac{\partial \epsilon}{\partial \phi} = (\epsilon^{fib}(r) - \epsilon^{fat}(r))\delta(\phi(r)) \tag{4.33}$$

The partial derivative of equation (4.28) with respect to static permittivity of fibroglandular tissues ϵ_s^{fib} is computed by using equation (4.34) [4].

$$\frac{\partial \epsilon}{\partial \epsilon_s^{fib}} = H(\phi(r))\frac{\partial \epsilon^{fib}}{\partial \epsilon_s^{fib}} \tag{4.34}$$

The partial derivative of equation (4.28) with respect to static permittivity of fatty tissues ϵ_s^{fat} is computed by using equation (4.35) [4].

$$\frac{\partial \epsilon}{\partial \epsilon_s^{fat}} = (1 - H(\phi(r)))\frac{\partial \epsilon^{fat}}{\partial \epsilon_s^{fat}} \tag{4.35}$$

The partial derivative of cost function with respect to level set function ϕ is calculated by using equation (4.36) [4].

$$\frac{\partial C}{\partial \phi} = \nabla C(\epsilon)\frac{\partial \epsilon}{\partial \phi} \tag{4.36}$$

The partial derivative of cost function with respect to ϵ_s^{fib} is computed by using equation (4.37) [4].

$$\frac{\partial C}{\partial \epsilon_s^{fib}} = \nabla C(\epsilon)\frac{\partial \epsilon}{\partial \epsilon_s^{fib}} \tag{4.37}$$

The partial derivative of cost function with respect to ϵ_s^{fat} is computed by using equation (4.38) [4].

$$\frac{\partial C}{\partial \epsilon_s^{fat}} = \nabla C(\epsilon)\frac{\partial \epsilon}{\partial \epsilon_s^{fat}} \tag{4.38}$$

The partial derivatives obtained above are used to implement gradient based descent optimization approach as shown below [4].

$$\phi^{n+1} = \phi^n - \alpha_\phi \frac{\partial C}{\partial \phi} \tag{4.39}$$

$$(\epsilon_s^{fib})^{n+1} = (\epsilon_s^{fib})^n - \alpha_{\epsilon_s}^{fib} \frac{\partial C}{\partial \epsilon_s^{fib}} \tag{4.40}$$

$$(\epsilon_s^{fat})^{n+1} = (\epsilon_s^{fat})^n - \alpha_{\epsilon_s}^{fat} \frac{\partial C}{\partial \epsilon_s^{fat}} \tag{4.41}$$

Where n is the iteration number. The step sizes are $\alpha_\phi, \alpha_{\epsilon_s}^{fib}$, and $\alpha_{\epsilon_s}^{fat}$ are individually chosen. A priori information related to breast tissues is useful in deciding above parameters.

4.3 Two 3D Level Set Function based Optimization

Shape and dielectric property reconstruction both are important in 3D reconstructions [15, 16, 17]. 3D level set based optimization is more suitable for 3D reconstruction because it can reconstruct shape and dielectric property simultaneously. Two level set functions are used in figure 4.3 to identify four different regions. In figure
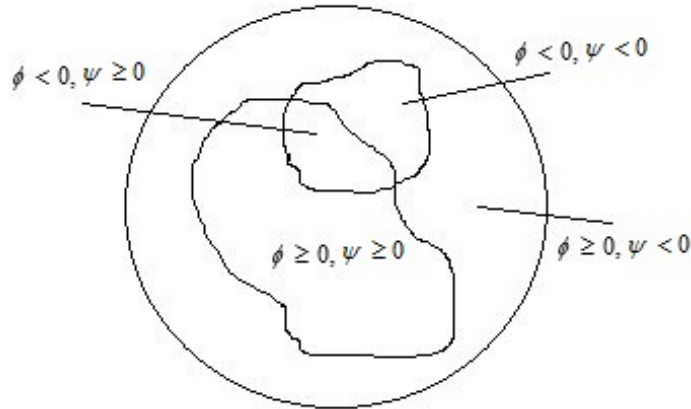
Figure 4.3: Application of two level set functions to distinguish four different regions (in 2D)

4.3, $\phi \geq 0, \psi \geq 0$, $\phi \geq 0, \psi < 0$, $\phi < 0, \psi \geq 0$ and $\phi < 0, \psi < 0$ represent healthy fatty tissues, healthy fibro-glandular tissues, malignant fatty tissues and malignant fibro-glandular tissues respectively. Scenario of figure 4.3 is expressed as equation (4.42).

$$\epsilon(r) = \epsilon^{tum}(1 - H(\phi)) + H(\phi)[\epsilon^{fib}H(\psi) + \epsilon^{fat}(1 - H(\psi))] \qquad (4.42)$$

In equation (4.42), $\epsilon^{tum}, \epsilon^{fib}$ and ϵ^{fat} are complex permittivity of tumour, fibro-glandular and fatty tissues respectively, $H()$ is unit step or heavy-side function. $\epsilon^{tum}, \epsilon^{fib}$ and ϵ^{fat} are expressed in terms of single pole Debye model. In equation (4.42), ϕ and ψ are two level set functions. 3D level set based optimization starts with an initial guess about solution. Signed distance function of initial guess is required. Steps to calculate signed distance function are given below.

- Find the edges of initial guess

- Find the positive distance inside the edge boundary

- Find the negative distance outside the edge boundary

- Normalize the distance

Signed distance function is between -1 to 1 after performing above steps. Now, this signed distance function is updated using iterative optimization approach. Sample code for signed distance fucntion generation is given in appendix C.2. Equations (4.29) and (4.30) represent linear relationships among Debye parameters. Partial derivative of equation (3.8) (cost function) with respect to permittivity is given below.

$$\frac{\partial C}{\partial \epsilon} = J^T(\epsilon)R(\epsilon) \qquad (4.43)$$

In equation (4.43), $J^T(\epsilon)$ is transpose of Jacobian matrix, $R(\epsilon)$ is residual. Jacobian matrix is calculated by element wise multiplication of green's function matrix with total electric field matrix [4, 13, 14]. Partial derivative of cost function with respect to level set function ϕ is calculated by using equation (4.44).

$$\frac{\partial C}{\partial \phi} = \frac{\partial C}{\partial \epsilon} \frac{\partial \epsilon}{\partial \phi} \qquad (4.44)$$

In equation (4.44), second partial derivative is calculated by taking partial derivative of equation (4.42) with respect to level set function ϕ.

$$\frac{\partial C}{\partial \phi} = J^T(\epsilon)R(\epsilon) \cdot \delta(\phi)(\epsilon^{fib}H(\psi) + \epsilon^{fat}(1 - H(\psi)) - \epsilon^{tum}) \tag{4.45}$$

Similarly, Partial derivative of cost function with respect to level set function ψ is calculated by using equation (4.46).

$$\frac{\partial C}{\partial \psi} = \frac{\partial C}{\partial \epsilon}\frac{\partial \epsilon}{\partial \psi} \tag{4.46}$$

In equation (4.46), second partial derivative is calculated by taking partial derivative of equation (4.42) with respect to level set function ψ.

$$\frac{\partial C}{\partial \psi} = J^T(\epsilon)R(\epsilon) \cdot (H(\phi)\delta(\psi)(\epsilon^{fib} - \epsilon^{fat})) \tag{4.47}$$

Partial derivative of cost function with respect to fibro-glandular tissue's static permittivity is given by equation (4.48).

$$\frac{\partial C}{\partial \epsilon_s^{fib}} = \frac{\partial C}{\partial \epsilon}\frac{\partial \epsilon}{\partial \epsilon^{fib}}\frac{\partial \epsilon^{fib}}{\partial \epsilon_s^{fib}} \tag{4.48}$$

Second partial derivative of equation (4.48) is calculated by taking partial derivative of equation (4.42) with respect to ϵ^{fib}. Third partial derivative of equation (4.48) is calculated using two steps. In first step, equations (4.29) and (4.30) are substituted in equation (3.3). In second step, partial derivative of resultant equation is taken with respect to ϵ_s^{fib}. Equation (4.49) is obtained by substituting partial derivatives in equation (4.48).

$$\frac{\partial C}{\partial \epsilon_s^{fib}} = J^T(\epsilon)R(\epsilon) \cdot H(\phi)H(\psi)\frac{\partial \epsilon^{fib}}{\partial \epsilon_s^{fib}} \tag{4.49}$$

Partial derivative of cost function with respect to fatty tissue's static permittivity is given by equation (4.50).

$$\frac{\partial C}{\partial \epsilon_s^{fat}} = \frac{\partial C}{\partial \epsilon}\frac{\partial \epsilon}{\partial \epsilon^{fat}}\frac{\partial \epsilon^{fat}}{\partial \epsilon_s^{fat}} \tag{4.50}$$

Equation (4.51) is obtained after calculating second and third partial derivatives of equation (4.50).

$$\frac{\partial C}{\partial \epsilon_s^{fat}} = J^T(\epsilon)R(\epsilon) \cdot H(\phi)(1 - H(\psi))\frac{\partial \epsilon^{fat}}{\partial \epsilon_s^{fat}} \tag{4.51}$$

Now, Four update equations are derived using equations (4.45), (4.47), (4.49) and (4.51).

$$\phi^{n+1} = \phi^n - \alpha_\phi \frac{\partial C}{\partial \phi} \tag{4.52}$$

$$\psi^{n+1} = \psi^n - \alpha_\psi \frac{\partial C}{\partial \psi} \tag{4.53}$$

$$\left(\epsilon_s^{fib}\right)^{n+1} = \left(\epsilon_s^{fib}\right)^n - \alpha_{\epsilon_s^{fib}}\frac{\partial C}{\partial \epsilon_s^{fib}} \tag{4.54}$$

$$\left(\epsilon_s^{fat}\right)^{n+1} = \left(\epsilon_s^{fat}\right)^n - \alpha_{\epsilon_s^{fat}}\frac{\partial C}{\partial \epsilon_s^{fat}} \tag{4.55}$$

Algorithm can not converge to solution for larger values of step size. It becomes slower due to smaller step size. Equations (4.52), (4.53), (4.54) and (4.55) are updated using four stage reconstruction strategy and frequency hopping [4, 17]. Four stage reconstruction strategy used in thesis is modified to reduce computations. First stage is an initial guess of class 3 numerical breast phantom internal structure. Second stage is reconstruction of breast tissues' shapes and dielectric profiles by using equations (4.53), (4.54) and (4.55). In third stage tumour location and shape are reconstructed by using equations (4.52) and (4.53). In last stage tumour permittivity value is decided by using equation (4.52).

4.3.1   3D Level Set based Regularized Optimization

In case of inverse scattering problem solution using ill posed system matrix and noise affected measurements, regularization is very useful [18, 19, 20]. Need of regularization is quite clear from figure.4.4. Numerical breast phantom and antenna placement of figure 4.4 are described in appendix A.1 and A.2 respectively. Sizes

of system matrix A, permittivity column vector x or ϵ and scattered electric field column vector b are $2MF \times 3K$, $3K \times 1$ and $2MF \times 1$ respectively. Additive white Gaussian noise n is added to scattered electric field vector b. Tikhonov and total
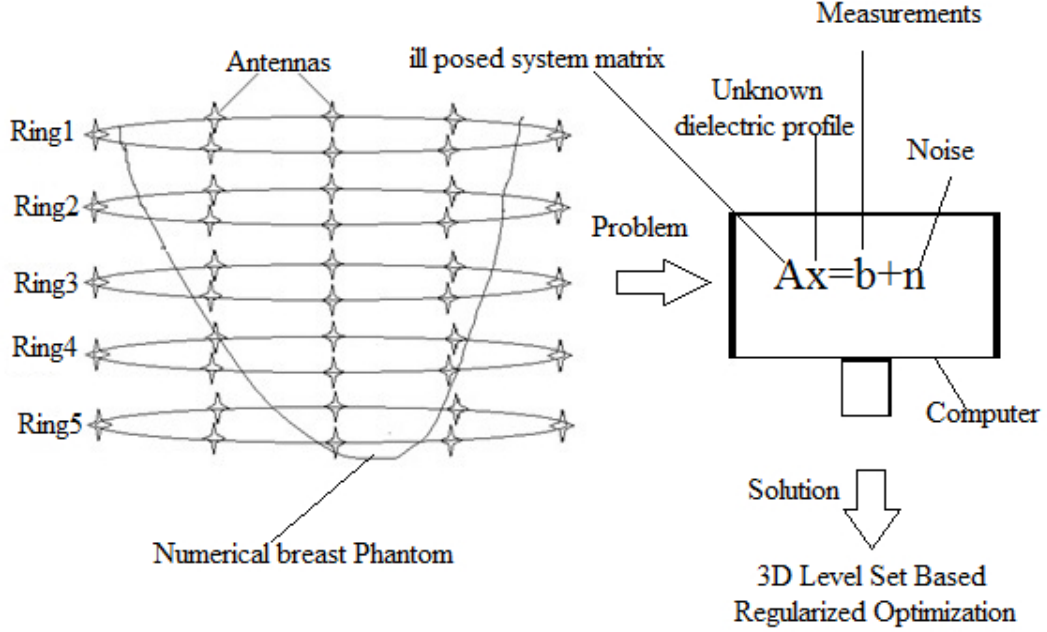
Figure 4.4: Block diagram of practical microwave breast imaging system.

variation regularization techniques are evaluated in this section. Details of both techniques are given in [20].

4.3.1.1 Tikhonov Regularization

Tikhonov regularization is very well known technique. Cost function is updated to include regularization term. Now, cost function of equation 4.56 is obtained by adding tikhonov regularization term in equation (3.8).

$$C(\epsilon) = \frac{1}{2}(\sum_{i=1}^{FM} |R_i|^2 + \lambda \|X_1\|^2) \tag{4.56}$$

In equation (4.56), λ is regularization parameter, and $\|X_1\|$ is L_2 norm of column vector X_1. Column vector X_1 contains static permittivity values for all voxels. Two things are achieved by regularization: First, Small residue is obtained with an accurate solution. Second, small solution is achieved such that the perturbation

does not affect it much. Partial derivate of cost function with respect to unknown parameter is given by equation (4.57).

$$\frac{\partial C}{\partial \epsilon} = J^T(\epsilon)R(\epsilon) + \lambda X_1 \tag{4.57}$$

In equation (4.57), $J^T(\epsilon)$ is transpose of Jacobian matrix. It is element by element multiplication of green's function matrix and total electric field matrix, $R(\epsilon)$ is residual.

4.3.1.2 Total Variation Regularization

Tikhonov regularization performs well in the situation where solution has smooth changes. It will not perform well in the case where solution has abrupt changes. Total variation regularization term is defined as shown in equation (4.58).

$$TV(X) = \sum_{j=1}^{n-1} |X_{j+1} - X_j| = \|L_1 X\|_1 \tag{4.58}$$

In equation (4.58), $\|L_1 X\|_1$ is L^1 norm of $\|L_1 X\|$. L_1 is a derivative matrix as shown by equation (4.59).

$$L_1 = \begin{bmatrix} -1 & 1 & 0 & . & . & 0 \\ 0 & -1 & 1 & 0 & . & 0 \\ 0 & 0 & -1 & 1 & 0 & . \\ . & . & 0 & . & . & . \\ . & . & . & . & . & . \\ . & . & . & 0 & -1 & 1 \\ 0 & 0 & 0 & 0 & 0 & -1 \end{bmatrix} \tag{4.59}$$

Now, equation (4.60) is obtained by replacing tikhonov regularization term with total variation regularization term.

$$C(\epsilon) = \frac{1}{2} \sum_{i=1}^{FM} |R_i|^2 + \lambda \|L_1 X\|_1 \tag{4.60}$$

65

L_1 norm is non differentiable. In order to obtain partial derivative, diagonal matrix W is used. Equation (4.61) is obtained by using the procedure of [20].

$$\frac{\partial C}{\partial \epsilon} = J^T(\epsilon)R(\epsilon) + \lambda L_1^T W L_1 x \tag{4.61}$$

$W_{j,j} = 1/|x_{j+1} - x_j|$, where $(x_{j+1} - x_j)$ is jth element of vector L_1x. Tolerance can be set on values of W to accommodate non differentiability of L_1 norm.

$$w_{j,j} = \begin{cases} \frac{1}{|X_{j+1}-X_j|} & , |X_{j+1} - X_j| \geq \epsilon \\ \frac{1}{\epsilon} & , |X_{j+1} - X_j| < \epsilon \end{cases} \tag{4.62}$$

Diagonal matrix W is calculated by using equation (4.62) in the iterative process. Cost function and it's partial derivative with respect to permittivity are changed to include regularization.

4.3.2 Steps for 3D Level Set based Optimization Implementation

Level set based optimization implementation steps are given below.

1. Convert system in matrix form $(A\epsilon = b)$

2. Calculate scattered electric field vector b using known ϵ values.

3. Add noise to scattered electric field $(\hat{b} = b + n)$.

4. Identify different regions to be reconstructed.

5. Decide number of level set functions to be used.

6. Start with the initial guess about ϵ.

7. Calculate signed distance function.

8. Calculate initial cost function $(C(\epsilon))$.

9. Calculate total electric field using 3D FDTD.

10. Calculate Jacobian matrix $(J(\epsilon))$.

11. Calculate required partial derivatives of cost function.

12. Update all equations such that the cost function is minimized.

13. If stopping criteria is satisfied then stop else repeat steps 8 to 13 by using reconstructed results of current iteration.

The above steps are implemented to reconstruct static permittivity values and shapes of breast tissues by minimizing cost function.

4.4   Simulation Parameters

Values of Debye parameters are given for different breast tissues in table 4.1 [13, 14]. These values are valid for 0.5 GHz to 3 GHz. For simplicity, only two major type of tissues are considered in class 3 numerical breast phantom [21, 22]. Five frequencies 0.5, 1, 1.5, 2 and 2.5 GHz are considered in the microwave breast imaging system simulation. Static permittivity values are found by adding $\Delta\epsilon$ to ϵ_∞. These static permittivity values are used in simulation. In microwave breast imaging using 3D level set based optimization, human breast is immersed in oil based surrounding medium because it matches the average dielectric properties of human breast. RMSE

Table 4.1: Values of Debye parameters for different breast tissues

Tissues	ϵ_∞	$\Delta\epsilon$	$\sigma_s(s/m)$
Adipose (fatty)	4.09	3.54	0.0842
Fibro-glandular	18.6	35.6	0.817
Skin	15.3	24.8	0.741
Tumour (assumed)	23.2	41	0.93
Immersion (Surrounding) medium	2.6	0	0

in complex permittivity is calculated by using equation (4.63).

$$RMSE = \sqrt{\frac{\sum\limits_{i=1}^{K}\left((\epsilon_s)_i - (\hat{\epsilon_s})_i\right)^2}{K}} \tag{4.63}$$

In equation (4.63), $(\epsilon_s)_i$ is an original static permittivity value of ith cell. $(\hat{\epsilon_s})_i$ is reconstructed permittivity value of ith cell. K is total number of cells used in the

breast phantom.

4.5 Results

Inverse scattering problem is solved for two regularization schemes to compare performance of both. SNR is 20 dB for all reconstructions. Original profile of static permittivity (ϵ_s) with 2cm×2cm×2cm tumour is shown in figure 4.5.

Figure 4.5: Coronal cross section of original static permittivity (ϵ_s) profile at (a) 1.5 cm. (b) 3 cm. (c) 4.5 cm. (d) 6 cm. (Brown dot in (b) represents 2cm×2cm×2cm tumour).

Figure 4.6: Coronal cross section of reconstructed static permittivity (ϵ_s) profile without regularization at (a) 1.5 cm. (b) 3 cm. (c) 4.5 cm. (d) 6.5 cm. (Brown dot in (b) represents tumour).

Now, these original static permittivity profile of figure 4.5 is used in simulation. Reconstructed profile of static permittivity without regularization is shown in figure 4.6. By comparing figure 4.6 with figure 4.5, it is clear that the reconstruction without regularization results in poor static permittivity profile. The size and shape parameters of the reconstructed tumour are different as compared to original tumour. Reconstructed profiles of static permittivity (ϵ_s) with tikhonov and TV regularization schemes are shown in figure 4.7 and figure 4.8 respectively.

Figure 4.7: Coronal cross section of reconstructed static permittivity (ϵ_s) profile with tikhonov regularization at (a) 1.5 cm. (b) 3 cm. (c) 4.5 cm. (d) 6.5 cm. (Brown dot in (b) represents tumour).

Figure 4.8: Coronal cross section of reconstructed static permittivity (ϵ_s) profile with TV regularization at (a) 1.5 cm. (b) 3 cm. (c) 4.5 cm. (d) 6.5 cm. (Brown dot in (b) represents tumour).

By comparing figure 4.7 with figure 4.6, it is clear that the reconstruction with tikhonov regularization results in better static permittivity profile than reconstruction without regularization. By comparing figure 4.8 with figures 4.6 and 4.7, it is clear that the reconstruction with TV regularization results in better static permittivity profile than all other reconstructions.
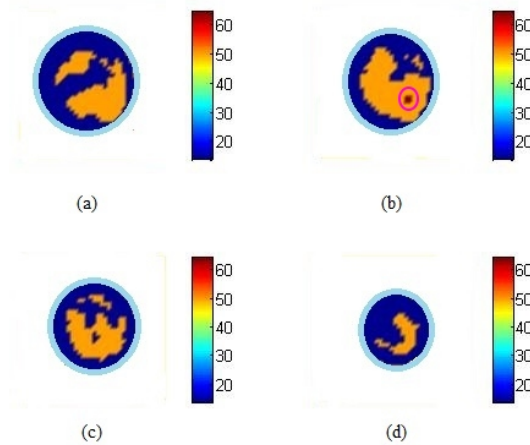
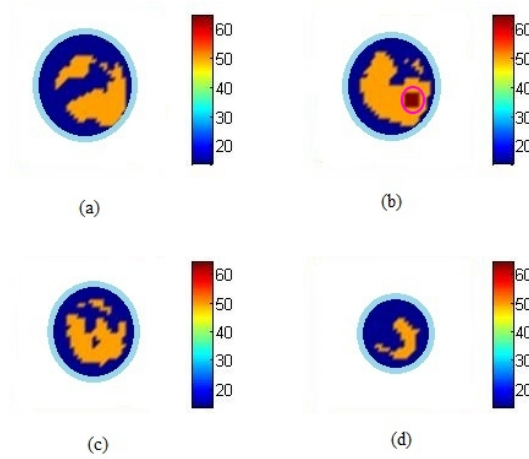

Figure 4.9: Coronal cross section of original static permittivity (ϵ_s) profile at (a) 1.5 cm. (b) 3 cm. (c) 4.5 cm. (d) 6.5 cm. (Brown dot in (b) represents 1cm×1cm×1cm tumour).
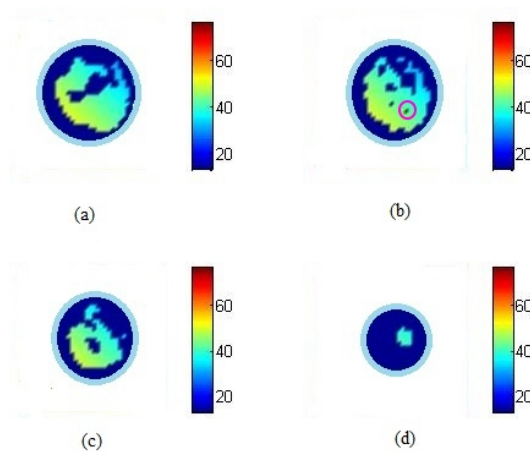
Figure 4.10: Coronal cross section of reconstructed static permittivity (ϵ_s) profile without regularization at (a) 1.5 cm. (b) 3 cm. (c) 4.5 cm. (d) 6.5 cm. (Brown dot in (b) represents tumour).

Original profile of static permittivity (ϵ_s) with 1cm×1cm×1cm tumour is shown in figure 4.9. Reconstructed profile of static permittivity without regularization is shown in figure 4.10. By comparing figure 4.9 with figure 4.10, it is clear that the reconstruction of small tumour parameters is very difficult without regularization. Reconstructed profiles of static permittivity (ϵ_s) with tikhonov and TV regularization schemes are shown in figure 4.11 and figure 4.12 respectively. By comparing figure
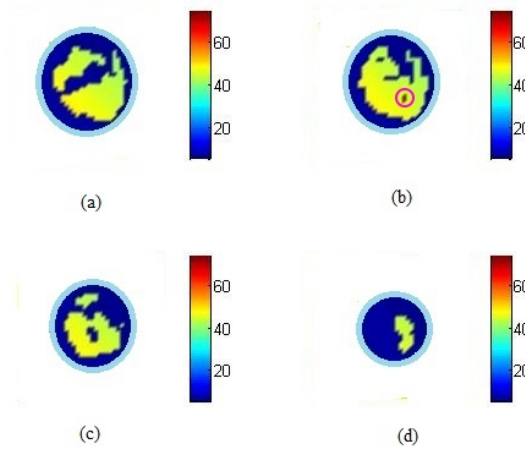
Figure 4.11: Coronal cross section of reconstructed static permittivity (ϵ_s) profile with tikhonov regularization at (a) 1.5 cm. (b) 3 cm. (c) 4.5 cm. (d) 6.5 cm. (Brown dot in (b) represents tumour).
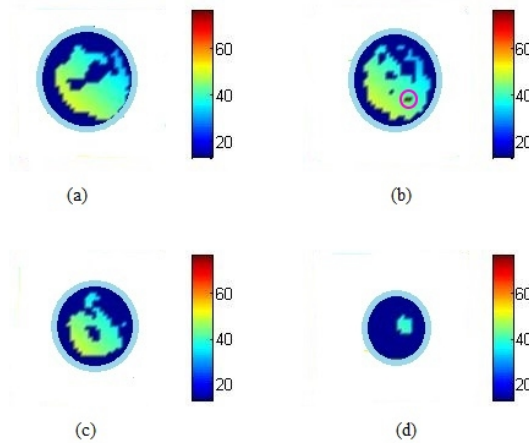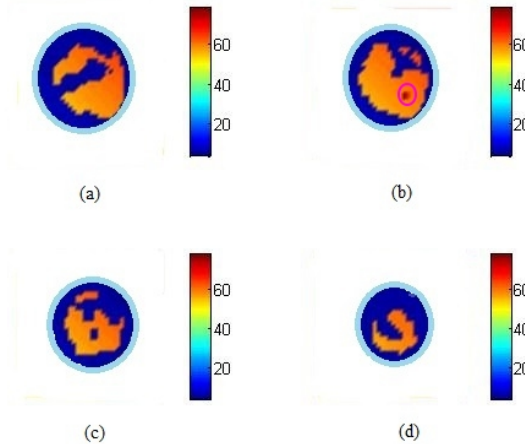

Figure 4.12: Coronal cross section of reconstructed static permittivity (ϵ_s) profile with TV regularization at (a) 1.5 cm. (b) 3 cm. (c) 4.5 cm. (d) 6.5 cm. (Brown dot in (b) represents tumour).

4.11 with figure 4.7, it is clear that the reconstruction of small tumour parameters

is difficult with tikhonov regularization. Figure 4.12 shows that the reconstruction of small tumour parameters is very good with TV regularization.

Original profile of static permittivity (ϵ_s) with 0.5cm×0.5cm×0.5cm tumour is shown in figure 4.13. Reconstructed profile of static permittivity without regular-
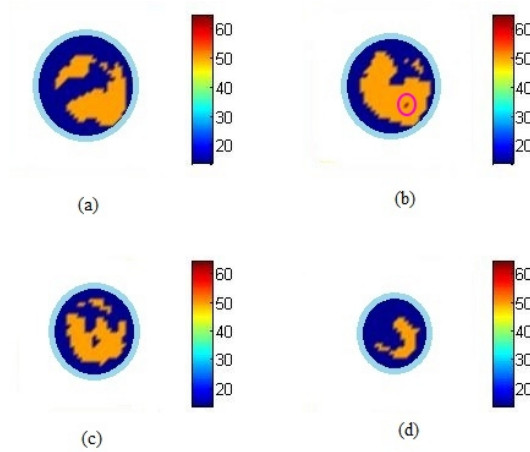
Figure 4.13: Coronal cross section of original static permittivity (ϵ_s) profile at (a) 1.5 cm. (b) 3 cm. (c) 4.5 cm. (d) 6.5 cm. (Brown dot in (b) represents 0.5cm×0.5cm×0.5cm tumour).

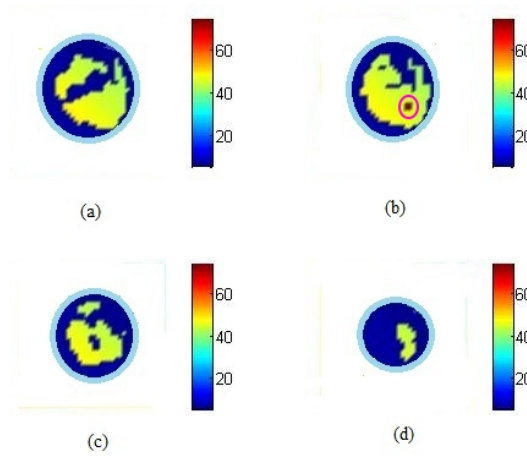ization is shown in figure 4.14. By comparing figure 4.14 with figure 4.13, it is
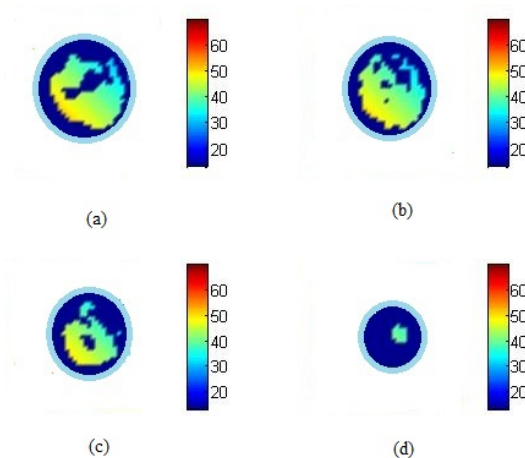
Figure 4.14: Coronal cross section of reconstructed static permittivity (ϵ_s) profile without regularization at (a) 1.5 cm. (b) 3 cm. (c) 4.5 cm. (d) 6.5 cm.

clear that the reconstruction of very small tumour parameters is impossible without

regularization. Reconstructed profiles of static permittivity (ϵ_s) with tikhonov and TV regularization schemes are shown in figure 4.15 and figure 4.16 respectively. By
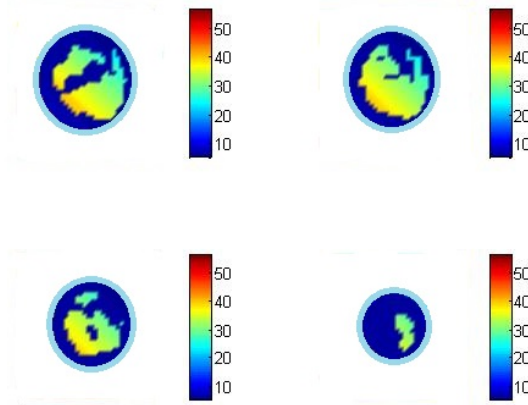
Figure 4.15: Coronal cross section of reconstructed static permittivity (ϵ_s) profile with tikhonov regularization at (a) 1.5 cm. (b) 3 cm. (c) 4.5 cm. (d) 6.5 cm.
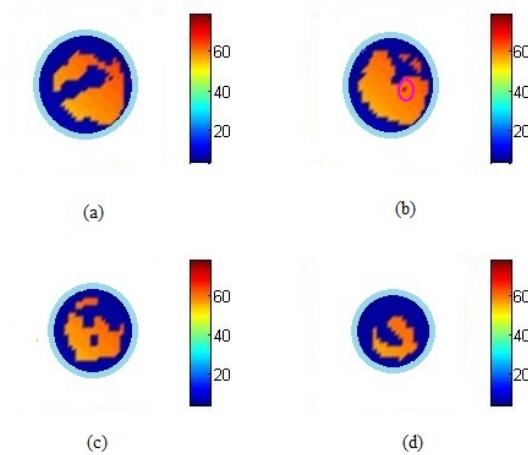
Figure 4.16: Coronal cross section of reconstructed static permittivity (ϵ_s) profile with TV regularization at (a) 1.5 cm. (b) 3 cm. (c) 4.5 cm. (d) 6.5 cm. (Brown dot in (b) represents tumour).
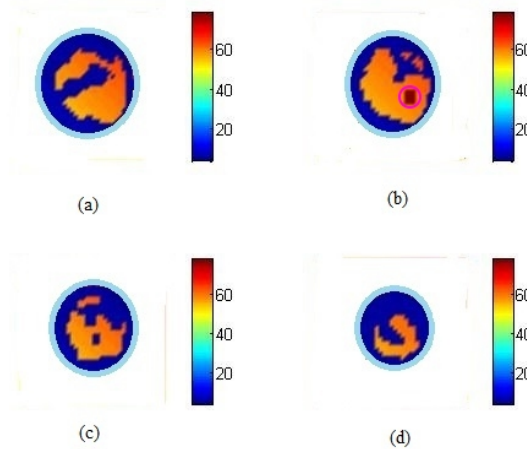
comparing figure 4.15 with figure 4.13, it is clear that the reconstruction of very small tumour parameters is almost impossible with tikhonov regularization. By comparing figure 4.16 with figure 4.13, it is clear that the reconstruction of very small tumour parameters is difficult with TV regularization. Location of very small tumour is not properly detected with TV regularization.

RMSE versus SNR graph is shown in figure 4.17 for three cases. Cost function versus number of iterations graph is shown in figure 4.18. RMSE values clearly show
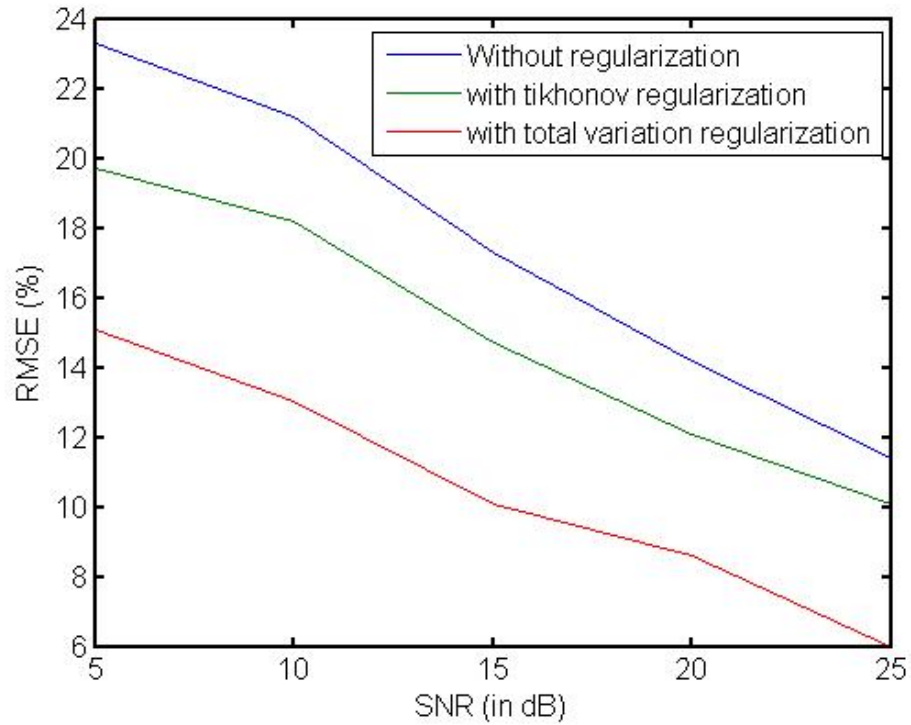
Figure 4.17: RMSE in static permittivity (ϵ_s) vs. SNR

that the performance of total variation regularization is better than the tiknonov regularization. Comparison of different algorithms are given below. Details of Gauss-
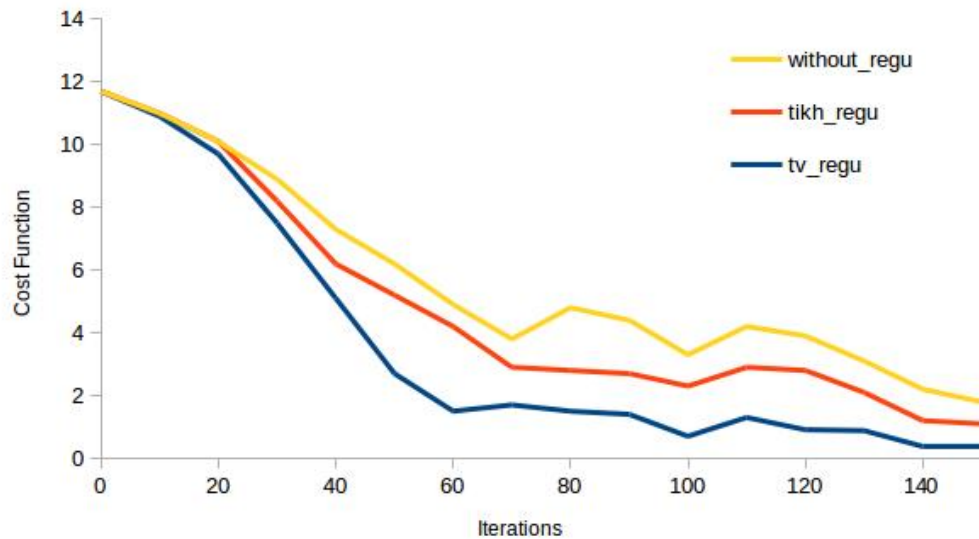
Figure 4.18: Cost vs. No. of Iterations

Newton, conjugate gradient and genetic algorithms are given in [14, 23, 24, 25, 26]. Table 4.2 clearly shows that the performance of 3D level set method is better than

Table 4.2: Comparison of RMSE for different algorithms

Methods	RMSE(%)
Gauss-Newton	24.14
Conjugate gradient method	21.62
Genetic algorithm	17.71
Level Set method	12.43

all other methods. 3D level set method has shape optimization feature which results in less error as compared to other methods.

4.6   Conclusions

3D level set based evolution and optimization approaches are described with mathematical framework for inverse scattering problems. Characteristics of evolution approach are discussed with implementation details. Gauss-Newton based optimization algorithm is described with steps for implementation. Four update equations are derived for two level set functions based optimization approach which can detect healthy and malignant breast tissues. Tikhonov and TV regularization schemes are used to improve performance of 3D level set based optimization. Shape, Size and location detection of breast tumour is possible by using 3D level set based methods.

Tikhonov regularization improve reconstruction results but its performance degrades for very small breast tumour size. The performance of TV regularization is better than Tikhonov regularization for medium, small and very small breast tumours. TV regularization reconstructs shape and size of very small tumour but it fails to reconstruct exact location of very small tumour. Total variation regularization performs better than tikhonov regularization because there are abrupt changes in the solution. Oscillations in cost function minimization are reduced by using regularization schemes which makes convergence faster.

3D level set based optimization with TV regularization is very effective for 5 dB to 25 dB SNR. In this work, 20 dB SNR is required for better microwave image reconstruction and breast tumour detection. Shape and dielectric properties both are reconstructed simultaneously in 3D level set based regularized optimization.

References

[1] S.Osher, J.A.Sethian, "Fronts propagating with curvature-dependent speed: algorithms based on Hamilton-Jacobi formulations,"Journal of Computational Physics, Vol. 79, pp. 12-49, 1988.

[2] S.Osher and R.Fedkiw, "Level set methods and dynamic implicit surfaces," Applied Mathematical Sciences, Springer-Verlag New York Inc, pp.1-142, 2003.

[3] F.Santosa, "A level-set approach for inverse problems involving obstacles," EASIM: Control, Optimization and Calculus of Variations, Vol. 1, pp. 17-33, January 1996.

[4] T.J.Colgan, S.C.Hagness, and B.D.Van Veen, "A 3-D level set method for microwave breast imaging," IEEE Transactions on Biomedical Engineering, Vol. 62, no. 10, pp. 2526-2534, 2015.

[5] M.Burger, "A level set method for inverse problems," Inverse Problems, Vol. 17, No. 5, August 2001.

[6] M.Burger, S.J.Osher, "A survey on level set methods for inverse problems and optimal design," European Journal of Applied Mathematics, Vol. 16, no. 2, pp. 263-301, April 2005.

[7] O.Dorn and D.Lesselier, "Level set methods for inverse scattering," Inverse Problems, Vol. 22, No. 4, pp. 1-79, June 2006.

[8] O.Dorn, E.L.Miller and C.M.Rappaport, "A shape reconstruction method for electromagnetic tomography using adjoint fields and level sets," Inverse Problems, Vol. 16, No. 5, October 2000.

[9] R.Ferraye, J.Y.Dauvignac, C.Pichot, "An inverse scattering method based on contour deformations by means of a level set method using frequency hopping technique," IEEE Transactions on Antennas and Propagation, Vol. 51, No. 5, pp.1100-1113, July 2003.

[10] A.Aghasi, M.Kilmer, and E.L.Miller, "Parametric level set methods for inverse problems," SIAM Journal on Imaging Sciences, Vol. 4, No. 2, pp. 618-650, 2011.

[11] O.Semerci, E.L.Miller, "A parametric level-set approach to simultaneous object identification and background reconstruction for dual-energy computed tomography," IEEE Transactions on Image Processing, Vol. 21, No. 5, pp.2719-2734, February 2012.

[12] M.R.Eskandari, M.Dehmollaian, R.Safian, "Simultaneous microwave imaging and parameter estimation using modified level-set method," IEEE Transactions on Antennas and Propagation, Vol. 64, No. 8, pp. 3554-3564, June 2016.

[13] D.W.Winters, J.D.Shea, P.Kosmas, B.D.Van Veen, S.C.Hagness, "Three-dimensional microwave breast imaging: dispersive dielectric properties estimation using patient-specific basis functions," IEEE Transactions on Medical Imaging, Vol. 28, no. 7, pp. 969-981, July 2009.

[14] J.D.Shea, P.Kosmas, S.C.Hagness, and B.D. Van Veen, "Three-dimensional microwave imaging of realistic numerical breast phantoms via a multiple-frequency inverse scattering technique," Medical Physics, Vol. 37, no. 8, pp. 4210-4226, 2010.

[15] N.Irishina, O.Dorn, M.Miguel, "A level set evolution strategy in microwave imaging for early breast cancer detection," Computers & Mathematics with Applications, Elsevier, Vol. 56, No. 3, pp. 607-618, August 2008.

[16] N.Irishina, M.Moscoso, O.Dorn, "Microwave imaging for early breast cancer detection using a shape-based strategy," IEEE Transactions on Biomedical Engineering, Vol. 56, No. 4, pp. 1143-1153, January 2009.

[17] N.Irishina, "Microwave medical imaging using level set techniques," PhD Thesis, University of Carlos, Spain, 2009.

[18] P.Hua, E.J.Woo, J.G.Webster, and W.J.Tompkins. "Iterative reconstruction methods using regularization and optimal current patterns in electrical impedance tomography," IEEE Transactions on Medical Imaging, Vol. 10, no. 4, pp. 621-628, 1991.

[19] H.Zhang, J.Huang, J.Ma, Z.Bian, Q.Feng, H.Lu, Z.Liang, and W.Chen. "Iterative reconstruction for X-ray computed tomography using prior-image induced nonlocal regularization," IEEE Transactions on Biomedical Engineering, Vol. 61, no. 9, pp. 2367-2378, 2014.

[20] S.Zhao and I.L.Al-Qadi. "Development of regularization methods on simulated ground-penetrating radar signals to predict thin asphalt overlay thickness," Signal Processing, Elsevier, Vol. 132, pp. 261-271, March 2017.

[21] E.Zastrow, S.K.Davis, M.Lazebnik, F.Kelcz, B.D.Van Veen, and S.C.Hagness, "Development of anatomically realistic numerical breast phantoms with accurate dielectric properties for modelling microwave interactions with the human breast," IEEE Transactions on Biomedical Engineering, Vol. 55, no. 12, pp. 2792-2800, 2008.

[22] M.Lazebnik, M.Okoniewski, J.H.Booske, and S.C.Hagness, "Highly accurate Debye models for normal and malignant breast tissue dielectric properties at microwave frequencies," IEEE Microwave and Wireless Components Letters, Vol. 17, no. 12, pp. 822-824, 2007.

[23] J.P.Stang, "A 3D Active Microwave Imaging System for Breast Cancer Screening" PhD Thesis, Duke University, USA, 2008.

[24] J.D.Zaeytijd, A.Franchois, C.Eyraud, and J.Geffrin, "Full-Wave Three-Dimensional Microwave Imaging With a Regularized Gauss-Newton Method-Theory and Experiment," IEEE Transactions on Antennas and Wave Propagation, Vol. 55, no. 11, pp. 3279-3292, November 2007.

[25] C.S.Park, B.S.Jeong, "Reconstruction of a high contrast and large object by using the hybrid algorithm combining a Levenberg-Marquardt algorithm and a genetic algorithm," IEEE Transactions on Magnetics, Vol. 35, no. 3, pp. 1582-1585, May 1999.

[26] T.Rubaek, P.M.Meaney, P.Meincke, and K.D.Paulsen, "Nonlinear microwave imaging for breast-cancer screening using Gauss-Newton's method and the CGLS inversion algorithm," IEEE Transactions on Antennas and Propagation, Vol. 55, no. 8, pp. 2320-2331, August 2007.

[27] H.N.Patel and D.K.Ghodgaonkar,"3D level set based optimization of inverse scattering problem for microwave breast imaging", IEEE MTT-S International Microwave Bio Conference, 15-17 May 2017, Gothenburg, Sweden, pp. 1-4.

[28] H.N.Patel and D.K.Ghodgaonkar, "Application of 3D level set based optimization in microwave breast imaging for cancer detection" accepted in Level Set Method in Medical Imaging Segmentation, Boca Raton:Fl, USA, CRC Press.

Chapter 5

3D FDTD Method

FDTD is an useful method for simultaneous acquisition of multi-frequency vector electromagnetic fields data over bandwidth of interest. FDTD method is computationally efficient because multiple frequency total electric field vector data acquisition is achieved in just one FDTD simulation. In this work, 3D FDTD is used to get multiple frequency total field vector data inside human breast model. Complex permittivity distribution of human breast model is determined by Debye model. Perfectly matched layer (PML) is required at all boundaries to absorb microwave signal. Two different sets of 3D FDTD update equations are required for implementation of Debye model and PML. In this chapter, The effect of breast cancer on electric field distribution is evaluated.

5.1 Theoretical Background

3D FDTD is used to solve forward problem due to limitations of method of moments (MoM). Maxwell's equations are solved on discrete grid in FDTD [1, 2, 3, 4]. Equations of Faraday and Ampere laws are given by equations (5.1) and (5.2).

$$\nabla \times \vec{E} = -\mu \frac{\partial \vec{H}}{\partial t} \tag{5.1}$$

$$\nabla \times \vec{H} = \epsilon \frac{\partial \vec{E}}{\partial t} \tag{5.2}$$

In equation (5.1), $\nabla \times \vec{E}$ is curl of electric field vector, $\vec{H}$ is magnetic field vector and μ is permeability of medium. In equation (5.2), $\nabla \times \vec{H}$ is curl of magnetic

field vector, $\vec{E}$ is electric field vector and ϵ is permittivity of medium. Now, finite difference approximation of Equations (5.1) and (5.2) are shown by equations (5.3) and (5.4) respectively.

$$\vec{H}_{t+\frac{\Delta t}{2}} = \vec{H}_{t-\frac{\Delta t}{2}} - \frac{\Delta t}{\mu}(\nabla \times \vec{E}_t) \tag{5.3}$$

$$\vec{E}_{t+\Delta t} = \vec{E}_t + \frac{\Delta t}{\epsilon}(\nabla \times \vec{H}_{t+\frac{\Delta t}{2}}) \tag{5.4}$$

In equation (5.3), $\vec{H}_{t+\frac{\Delta t}{2}}$ is magnetic field vector at future time step, $\vec{H}_{t-\frac{\Delta t}{2}}$ is magnetic field vector at previous time step, Δt is time step and $\nabla \times \vec{E}_t$ is curl of electric field vector at time t. In equation (5.4), $\vec{E}_{t+\Delta t}$ is electric field vector at future time step, $\vec{E}_t$ is electric field vector at current time step and $\nabla \times \vec{H}_{t+\frac{\Delta t}{2}}$ is curl of magnetic field at time $t + \frac{\Delta t}{2}$. Above equations are also known as update equations. Curl of electric field is calculated on whole discrete grid. Now, magnetic field is updated on whole grid by using equation (5.3). Curl of magnetic field is calculated on whole grid. Now, electric field is updated on whole grid by using eqaution (5.4). This updating process is repeated up to certain number of iterations. This approach is known as FDTD.
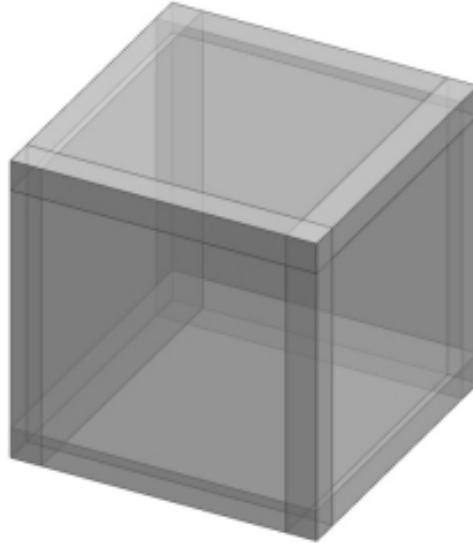
Figure 5.1: Grid for 3D FDTD [4]

$$\Delta t \propto \Delta \tag{5.5}$$

Time step is directly proportional to spatial size. Where, $\Delta x = \Delta y = \Delta z = \Delta$. Temporal accuracy increases for smaller values of time step up to several extent. Spatial step size reduction results in smaller time step values, which improve overall accuracy with longer simulation time. 3D FDTD grid is shown in figure 5.1. In figure 5.1, light grey region is used for numerical breast phantom and dark grey region at the boundary is used for perfectly matched layer (PML). All six PML boundaries are shown in figure 5.2. Dispersion is incorporated by using Debye model for numerical
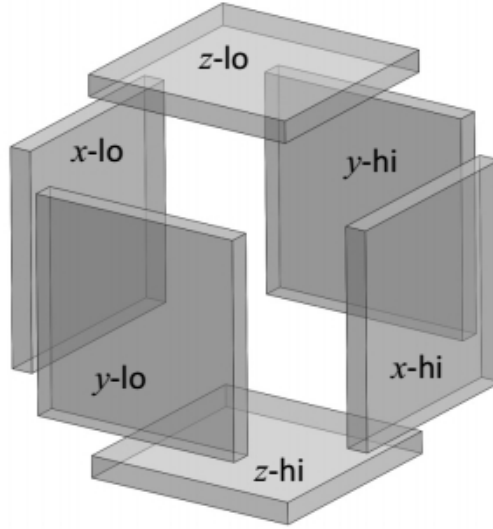
Figure 5.2: PML boundaries for 3D FDTD [4]

breast phantom region [3, 6, 7]. PML equations are required only at the boundaries. Now, two sets of electric field update equations are required. One set of electric field update equations is used for numerical breast phantom region excluding boundaries. The other set of electric field update equations is used for PML boundaries.

5.2 Electric Field Update Equations for Numerical Breast Phantom Region

Debye model is required to incorporate polarization and dispersion properties of numerical breast phantom region on grid. Electric field update equations for class III numerical breast phantom are derived for FDTD [3, 5]. Equation (5.6) represents

equation of Ampere's law after incorporating Debye model in it [3, 5, 6, 7].

$$\nabla \times \vec{H} = \epsilon_0 \epsilon_\infty j\omega \vec{E} + \sigma_s \vec{E} + j\omega \epsilon_0 \frac{\Delta \epsilon}{1 + j\omega\tau} \vec{E} \tag{5.6}$$

In equation (5.6), $\vec{H}$ is magnetic field intensity vector, $\vec{E}$ is electric field intensity vector. Equation (5.6) is converted into time domain by using inverse Fourier transform. Now, equation (5.8) is obtained by applying FDTD on this time domain equation. Derivation of equation is shown in appendix B.2. Equation (5.7) shows result of derivation.

$$\vec{E}_{t+\Delta t} = \frac{\left(1 - \frac{\sigma_s \Delta t}{2\epsilon_0 \epsilon_\infty} + \frac{\Delta t \cdot mj2}{2\delta \epsilon_0 \epsilon_\infty}\right)}{\left(1 + \frac{\sigma_s \Delta t}{2\epsilon_0 \epsilon_\infty} + \frac{\Delta t \cdot mj2}{2\delta \epsilon_0 \epsilon_\infty}\right)} \vec{E}_t + \frac{c_0 \Delta t}{2\delta \epsilon_\infty \left(1 + \frac{\sigma_s \Delta t}{2\epsilon_0 \epsilon_\infty} + \frac{\Delta t \cdot mj2}{2\delta \epsilon_0 \epsilon_\infty}\right)} \cdot \left(2\delta \nabla \times \vec{H}_{t+\frac{\Delta t}{2}} - \eta_0 (1 + mj1)\delta \vec{J}_P^t\right) \tag{5.7}$$

$$\vec{E}_{t+\Delta t} = me1 \cdot \vec{E}_t + me2 \cdot \left[(2\Delta x \cdot \nabla \times \vec{H}) - (\eta_0 \cdot (1 + mj1) \cdot \Delta x \cdot \vec{J}_P)\right] \tag{5.8}$$

In equation (5.8), $\vec{E}_{t+\Delta t}$ is electric field intensity vector at next time step, $\vec{E}_t$ is electric field intensity at current time step, $\nabla \times \vec{H}$ is curl of magnetic field intensity vector, $\vec{J}_P$ is polarization current density vector, Δx is size of voxel in x direction. Coefficient me1 is given by equation (5.9).

$$me1 = \frac{1 - \frac{\sigma_s \Delta t}{2\epsilon_0 \epsilon_\infty} + \frac{mj2 \cdot \Delta t}{2\epsilon_0 \epsilon_\infty \Delta x}}{1 + \frac{\sigma_s \Delta t}{2\epsilon_0 \epsilon_\infty} + \frac{mj2 \cdot \Delta t}{2\epsilon_0 \epsilon_\infty \Delta x}} \tag{5.9}$$

In equation (5.9), Δt is time step. Coefficient me2 is given by equation (5.10).

$$me2 = \frac{c_0 \Delta t}{2\Delta x \cdot \epsilon_\infty (1 + \frac{\sigma_s \Delta t}{2\epsilon_0 \epsilon_\infty} + \frac{mj2 \cdot \Delta t}{2\epsilon_0 \epsilon_\infty \Delta x})} \tag{5.10}$$

In equation (5.10), c_0 is velocity of light in free space. Derivation of equation (5.11) is shown in appendix B.2. Final result of derivation is shown by equation (5.11). Polarization current density update equation is given by equation (5.12).

$$\delta \vec{J}_P^{t+\Delta t} = \left(\frac{1 - \frac{1}{2N_t}}{1 + \frac{1}{2N_t}}\right) \delta \vec{J}_P^t + \left(\frac{\epsilon_0 \Delta \epsilon \delta}{N_t \Delta t \cdot (1 + \frac{1}{2N_t})}\right) (\vec{E}_{t+\Delta t} - \vec{E}_t) \tag{5.11}$$

$$\vec{J}_P^{t+\Delta t} = mj1 \cdot \vec{J}_P^t + \frac{mj2 \cdot (\vec{E}_{t+\Delta t} - \vec{E}_t)}{\Delta x} \tag{5.12}$$

In equation (5.12), $\vec{J}_P^{t+\Delta t}$ is polarization current density at next time step, $\vec{J}_P^t$ is polarization density at current time step. Coefficient mj1 is given by equation (5.13).

$$mj1 = \frac{1 - \frac{1}{2N_t}}{1 + \frac{1}{2N_t}} \tag{5.13}$$

In equation (5.13), relaxation time constant is given by $\tau = N_t \Delta t$. Coefficient mj2 is given by equation (5.14).

$$mj2 = \frac{\epsilon_0 \Delta \epsilon \Delta x}{N_t \Delta t \cdot (1 + \frac{1}{2N_t})} \tag{5.14}$$

Equations (5.12), (5.13) and (5.14) are implemented for x, y and z components of the polarization current density vector. Polarization current density vector is updated before updating electric field vector. Equations (5.8), (5.9) and (5.10) are implemented for x, y, z components of the electric field vector. Detailed derivation of electric field update equations for numerical breast phantom region is given in appendix B.2.

5.3   Electric Field Update Equations for PML Region

PML is required only at the boundaries of grid to absorb microwave signal. Electric field update equation derivation for PML region is given in [3, 5, 8]. Modified equation of Ampere's law to include PML is shown by equation (5.15).

$$\nabla \times \vec{H} = j\omega[s]\vec{D} \tag{5.15}$$

Now, matrix S is substituted in equation (5.15). Derivation of X,Y and Z components are same so only single component derivation is included in this work. X component

of above equation after substituting matrix s is shown by equation (5.16).

$$
\begin{aligned}
j\omega \left(1 + \frac{\sigma_x}{j\omega\epsilon_0}\right)^{-1} \left(1 + \frac{\sigma_y}{j\omega\epsilon_0}\right) \left(1 + \frac{\sigma_z}{j\omega\epsilon_0}\right) D_x = \\
c_0 \left[\frac{\partial H_z}{\partial y} - \frac{\partial H_y}{\partial z}\right]
\end{aligned}
\tag{5.16}
$$

Now, Equation (5.16) is used to derive final equation (5.17). Detailed derivation of electric field update equation is given in the appendix B.3.

$$
\begin{aligned}
D_x^{t+\Delta t} = \frac{\left(\frac{1}{\Delta t} - \frac{\sigma_y+\sigma_z}{2\epsilon_0} - \frac{\sigma_y\cdot\sigma_z\cdot\Delta t}{4\epsilon_0^2}\right)}{\left(\frac{1}{\Delta t} + \frac{\sigma_y+\sigma_z}{2\epsilon_0} + \frac{\sigma_y\cdot\sigma_z\cdot\Delta t}{4\epsilon_0^2}\right)} D_x^t + \frac{c_0 \cdot CH_x}{\left(\frac{1}{\Delta t} + \frac{\sigma_y+\sigma_z}{2\epsilon_0} + \frac{\sigma_y\cdot\sigma_z\cdot\Delta t}{4\epsilon_0^2}\right)} \\
+ \frac{c_0 \cdot \Delta t \cdot \sigma_x}{\left(\frac{1}{\Delta t} + \frac{\sigma_y+\sigma_z}{2\epsilon_0} + \frac{\sigma_y\cdot\sigma_z\cdot\Delta t}{4\epsilon_0^2}\right) \cdot \epsilon_0} (Ich)_x - \frac{\Delta t \cdot \sigma_y \cdot \sigma_z \cdot ID_x}{\left(\frac{1}{\Delta t} + \frac{\sigma_y+\sigma_z}{2\epsilon_0} + \frac{\sigma_y\cdot\sigma_z\cdot\Delta t}{4\epsilon_0^2}\right) \cdot \epsilon_0^2}
\end{aligned}
\tag{5.17}
$$

$$
\vec{D}_{t+\Delta t} = mdx1 \cdot \vec{D}_t + mdx2 \cdot (\nabla \times \vec{H})_x + mdx3 \cdot (Ich)_x + mdx4 \cdot (ID)_x \tag{5.18}
$$

In equation (5.18), $\vec{D}_{t+\Delta t}$ is electric field density (x component) at next time step, $\vec{D}_t$ is electric field density (x component) at previous time step, $(\nabla \times \vec{H})_x$ is x component of curl of vector H. $(Ich)_x$ is x component of integration of curl of vector H. $(ID)_x$ is x component of integration of electric field density vector D. Coefficient mdx0 is given by equation (5.19).

$$
mdx0 = \frac{1}{\Delta t} + \frac{\sigma_y + \sigma_z}{2\epsilon_0} + \frac{\sigma_y \cdot \sigma_z \cdot \Delta t}{4\epsilon_0^2} \tag{5.19}
$$

In equation (5.19), σ_y and σ_z are conductivity in y and z directions respectively. These conductivity values are non zero only in the PML region. Coefficient mdx1 is given by equation (5.20).

$$
mdx1 = \frac{1}{mdx0} \left(\frac{1}{\Delta t} - \frac{\sigma_y + \sigma_z}{2\epsilon_0} - \frac{\sigma_y \cdot \sigma_z \cdot \Delta t}{4\epsilon_0^2}\right) \tag{5.20}
$$

Coefficient mdx2 is given by equation (5.21).

$$mdx2 = \frac{c_0}{mdx0} \tag{5.21}$$

In equation (5.21), c_0 is speed of light. Coefficient mdx3 is given by equation (5.22).

$$mdx3 = \frac{c_0 \cdot \Delta t \cdot \sigma_x}{mdx0 \cdot \epsilon_0} \tag{5.22}$$

In equation (5.22), σ_x is x component of conductivity. Coefficient mdx4 is given by equation (5.23).

$$mdx4 = -\frac{\Delta t \cdot \sigma_y \cdot \sigma_z}{mdx0 \cdot \epsilon_0^2} \tag{5.23}$$

Equations (5.18) to (5.23) are implemented for x, y and z components of electric field density vector D in PML region. Electric field in PML region is updated by using simple relation between electric field density and electric field intensity.

5.4   Magnetic Field Update Equations

Human body is non magnetic, so only one set of FDTD equations are required through out the grid. Faraday's law with loss matrix s is given by equation (5.24).

$$\nabla \times \vec{E} = -j\omega\mu_0[\mu_r][s]\vec{H} \tag{5.24}$$

Equation (5.25) is obtained by applying same procedure as electric field update equation derivation

$$H_x^{t+\frac{\Delta t}{2}} = \frac{\left(\frac{1}{\Delta t} - \frac{\sigma_y+\sigma_z}{2\epsilon_0} - \frac{\sigma_y\cdot\sigma_z\cdot\Delta t}{4\epsilon_0^2}\right)}{\left(\frac{1}{\Delta t} + \frac{\sigma_y+\sigma_z}{2\epsilon_0} + \frac{\sigma_y\cdot\sigma_z\cdot\Delta t}{4\epsilon_0^2}\right)} H_x^{t-\frac{\Delta t}{2}} - \frac{c_0 \cdot CE_x}{\mu_{xx}\left(\frac{1}{\Delta t} + \frac{\sigma_y+\sigma_z}{2\epsilon_0} + \frac{\sigma_y\cdot\sigma_z\cdot\Delta t}{4\epsilon_0^2}\right)}$$
$$- \frac{c_0 \cdot \Delta t \cdot \sigma_x}{\mu_{xx}\left(\frac{1}{\Delta t} + \frac{\sigma_y+\sigma_z}{2\epsilon_0} + \frac{\sigma_y\cdot\sigma_z\cdot\Delta t}{4\epsilon_0^2}\right) \cdot \epsilon_0}(Ice)_x - \frac{\Delta t \cdot \sigma_y \cdot \sigma_z \cdot IH_x}{\left(\frac{1}{\Delta t} + \frac{\sigma_y+\sigma_z}{2\epsilon_0} + \frac{\sigma_y\cdot\sigma_z\cdot\Delta t}{4\epsilon_0^2}\right) \cdot \epsilon_0^2} \tag{5.25}$$

$$\vec{H}_{t+\frac{\Delta t}{2}} = mhx1 \cdot \vec{H}_{t-\frac{\Delta t}{2}} + mhx2 \cdot (\nabla \times \vec{E})_x + mhx3 \cdot (Ice)_x + mdx4 \cdot (IH)_x \tag{5.26}$$

In equation (5.26), $\vec{H}_{t+\frac{\Delta t}{2}}$ is magnetic field intensity (x component) at future time step, $\vec{H}_{t-\frac{\Delta t}{2}}$ is magnetic field intensity (x component) at previous time step, $(\nabla \times \vec{E})_x$ is x component of curl of electric field vector E. $(Ice)_x$ is x component of integration of curl of electric field vector E. $(IH)_x$ is x component of integration of magnetic field intensity vector H. Coefficient mhx0 is given by equation (5.27).

$$mhx0 = \frac{1}{\Delta t} + \frac{\sigma_y + \sigma_z}{2\epsilon_0} + \frac{\sigma_y \cdot \sigma_z \cdot \Delta t}{4\epsilon_0^2} \tag{5.27}$$

In equation (5.27), σ_y and σ_z are conductivity in y and z directions respectively. These conductivity values are non zero only in the PML region. Coefficient mhx1 is given by equation (5.28).

$$mhx1 = \frac{1}{mhx0} \left(\frac{1}{\Delta t} - \frac{\sigma_y + \sigma_z}{2\epsilon_0} - \frac{\sigma_y \cdot \sigma_z \cdot \Delta t}{4\epsilon_0^2} \right) \tag{5.28}$$

Coefficient mhx2 is given by equation (5.29).

$$mhx2 = -\frac{c_0}{mhx0 \cdot \mu_{xx}} \tag{5.29}$$

In equation (5.29), c_0 is speed of light. Coefficient mhx3 is given by equation (5.30).

$$mhx3 = -\frac{c_0 \cdot \Delta t \cdot \sigma_x}{mhx0 \cdot \epsilon_0 \mu_{xx}} \tag{5.30}$$

In equation (5.30), σ_x is x component of conductivity. Coefficient mhx4 is given by equation (5.31).

$$mhx4 = -\frac{\Delta t \cdot \sigma_y \cdot \sigma_z}{mhx0 \cdot \epsilon_0^2} \tag{5.31}$$

Equations (5.26) to (5.31) are implemented for x, y and z components of magnetic field intensity vector H.

5.5 Steps for FDTD Implementation

FDTD implementation steps are given below.

1. Define FDTD parameters

2. Set all fields to zero

3. Set all integration terms to zero

4. Set up numerical breast phantom on grid

5. Calculate coefficient of E field and H field update equations (including PML)

6. Start main FDTD loop

7. Update curl of electric field

8. Update magnetic field related integration terms

9. Update magnetic field using update equations

10. Insert electric field source

11. Update curl of magnetic field

12. Update electric field related integration terms

13. Update electric field using update equations

14. Insert magnetic field source

15. Apply Fourier transform to electric field

16. Visualize fields

17. Stop main FDTD loop after certain number of iterations

The proposed approaches of [9, 10, 11, 12] have used above FDTD simulation. Some of the advanced signal processing approaches are combined with FDTD in [13, 14, 15, 16]. Sample code for 3D FDTD is given in appendix C.3.

5.6 Simulation Parameters

Values of Debye parameters are given for different breast tissues in table 4.1. These values are valid for 0.5 GHz to 3 GHz. For simplicity, only two major type of tissues are considered in class 3 numerical breast phantom. Coronal cross sections of numerical breast phantom with $\Delta\epsilon$ original profile is shown in figure 5.3. The malignant tumour is assumed in the fibro-glandular tissues. Five frequencies 0.5, 1, 1.5, 2 and 2.5 GHz are considered for 3D FDTD simulation.
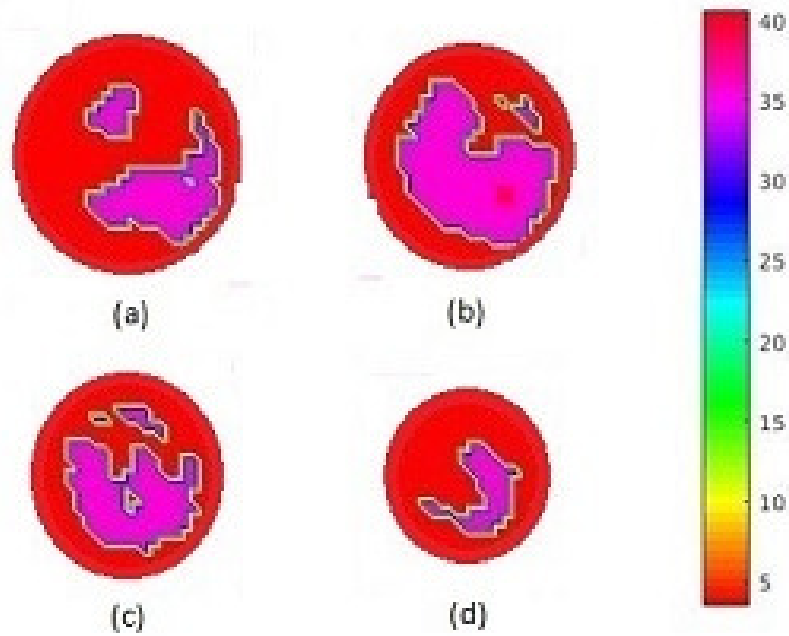
Figure 5.3: Coronal cross section of class 3 breast phantom with original profile of $\Delta\epsilon$ at (a) 1.5 cm. (b) 3 cm. (c) 4.5 cm. (d) 6 cm. (Dark pink dot of (b) indicates malignant tumour tissues)

5.7 Results

Electric field is calculated inside numerical breast phantom using FDTD simulation. Dielectric profile of figure 5.3 is used in this simulation. Electric field after 200, 400, 600 and 800 iterations are shown in figures 5.4, 5.5, 5.6 and 5.7 respectively.
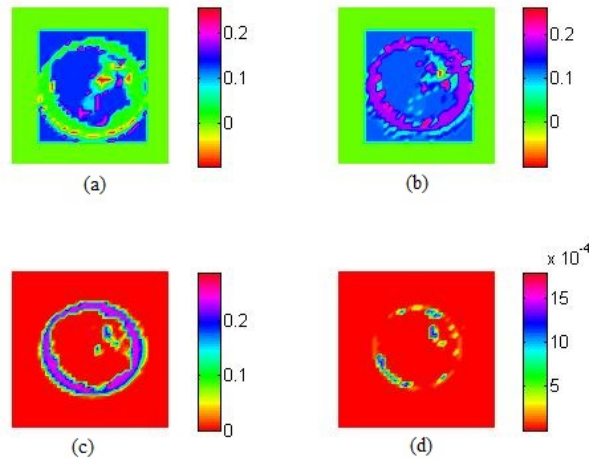
Figure 5.4: Electric field in class 3 numerical breast phantom (without cancer) after 200 iterations at (a) 1.5 cm. (b) 3 cm. (c) 4.5 cm. (d) 6 cm.
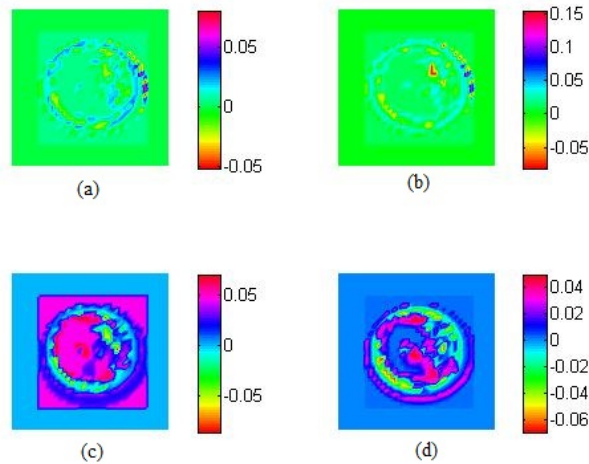
Figure 5.5: Electric field in class 3 numerical breast phantom (without cancer) after 400 iterations at (a) 1.5 cm. (b) 3 cm. (c) 4.5 cm. (d) 6 cm.

Electric field is applied as narrow Gaussian pulse. It is quite clear from figures 5.4 and 5.5 that the electric field increases up to 400 iterations. Figures 5.6 and
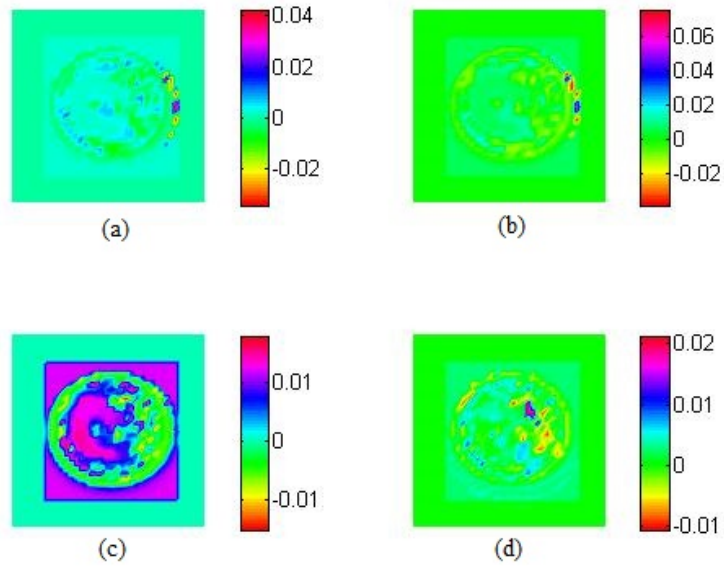
Figure 5.6: Electric field in class 3 numerical breast phantom (without cancer) after 600 iterations at (a) 1.5 cm. (b) 3 cm. (c) 4.5 cm. (d) 6 cm.
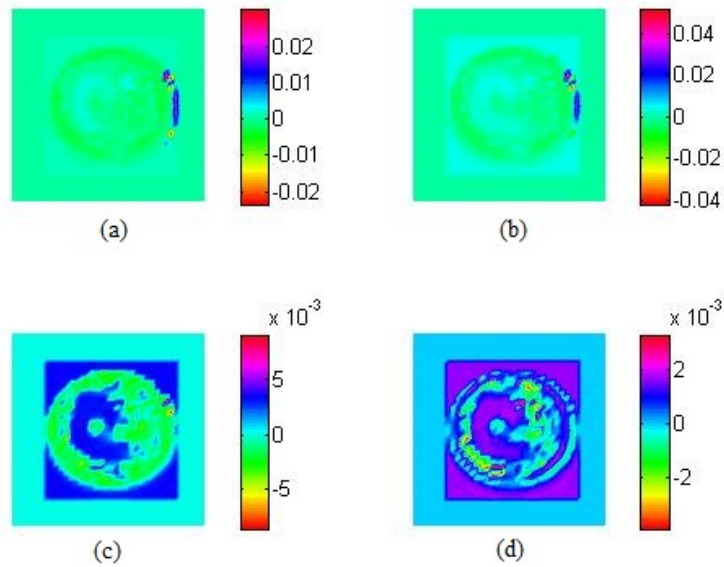
Figure 5.7: Electric field in class 3 numerical breast phantom (without cancer) after 800 iterations at (a) 1.5 cm. (b) 3 cm. (c) 4.5 cm. (d) 6 cm.

5.7 clearly show decrease in electric field after 400 iterations. Above figures clearly show validity of FDTD code. Now, malignant tumour is included in numerical breast phantom. Electric field is calculated inside numerical breast phantom with cancer.
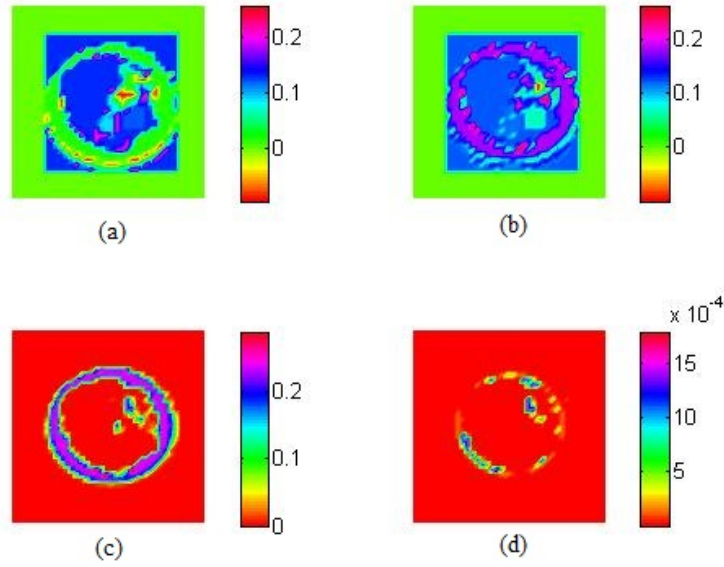
Figure 5.8: Electric field in class 3 numerical breast phantom (with cancer) after 200 iterations at (a) 1.5 cm. (b) 3 cm. (c) 4.5 cm. (d) 6 cm.
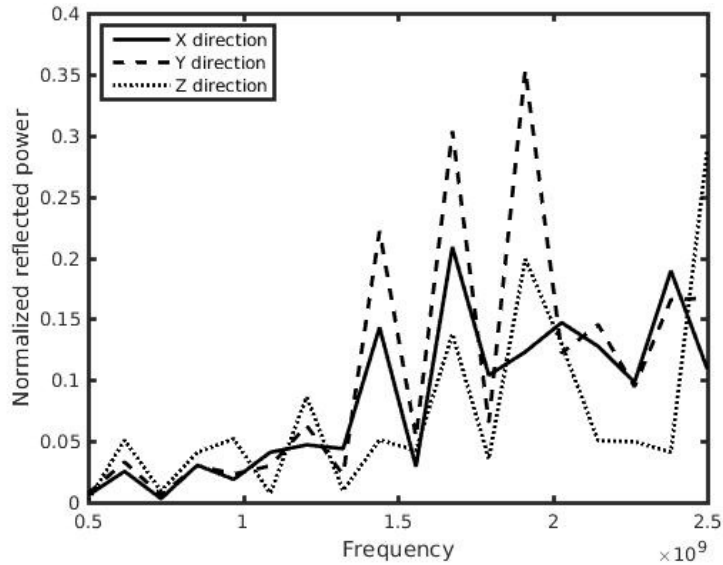
Figure 5.9: Normalized reflected power vs. frequency for different directions

Electric field after 200 iterations is shown in figure 5.8. Comparison of figure 5.4 with figure 5.8 clearly shows capability of FDTD as forward problem solver. Electric field in cancerous tissues of figure 5.8 is different. Figure 5.8 shows that electric field inside numerical breast phantom is affected due to inclusion of cancerous tissues.

Now, graph of normalized reflected power versus frequency is shown in figure 5.9. It is quite clear from figure 5.9 that normalized reflected power varies with the direction of wave propagation. This effect is due to heterogeneous nature of numerical breast phantom.

5.8 Conclusions

Debye equation is included in 3D FDTD to model polarization and dispersion properties of human breast tissues. Electric field update equations are derived for numerical breast phantom and PML regions on the grid. Magnetic field update equations are derived for the whole grid. Electric field computation in heterogeneous numerical breast phantom is very efficient using 3D FDTD method. Dispersion and polarization properties of breast tissues are easily incorporated in 3D FDTD update equations.

Electric field distribution is found in healthy and malignant breast tissues by using 3D FDTD. Malignant and healthy breast tissues have different electric field distributions. This property makes 3D FDTD suitable for microwave imaging of heterogeneous breast model. 3D FDTD solves forward problem efficiently during each iteration of 3D level set method which leads to better reconstruction of permittivity. Normalized reflected power varies with direction of wave propagation in heterogeneous numerical breast phantom.

References

[1] K.Yee, "Numerical solution of initial boundary value problems involving Maxwell's equations in isotropic media," IEEE Transactions on Antennas and Propagation, Vol. 14, no. 3, pp. 302-307, 1966.

[2] A.Taflove, "Application of the finite-difference time-domain method to sinusoidal steady-state electromagnetic-penetration problems," IEEE Transactions on Electromagnetic Compatibility, Vol. 22, no. 3, pp. 191-202, 1980.

[3] J.B.Schneider, "Understanding the Finite-Difference Time-Domain Method," pp. 33-308, www.eecs.wsu.edu/ schneidj/ufdtd, 2010.

[4] Computational electromagnetic lecture 9, available at http://emlab.utep.edu/ee5390cem/Lecture 9–Perfectly Matched Layer.pdf, accessed January 2015

[5] A.Taflove, S.C.Hagness, "Computational Electrodynamics: The Finite-difference Time-domain Method," Boston, The Artech House, pp. 81-105, 2000.

[6] M.Okonievski, M.Mrozowski, and M.A.Stuchly, "Simple treatment of multi-term dispersion in FDTD", IEEE Microwave Guided Wave Letters, Vol. 7, pp. 121-123, 1997.

[7] K.Kang , X.Chu, R.Dilmaghani and M.Ghavami, "Low-complexity Cole-Cole expression for modelling human biological tissues in FDTD method," Electronic letters, Vol.43, no. 3, 2007.

[8] S.D.Gedney,"An anisotropic perfectly matched layer-absorbing medium for the truncation of FDTD lattices," IEEE Transactions on Antennas and Propagation, Vol. 44, no. 12, pp. 1630-1639, 1996

[9] S.C.Hagness, A.Taflove, and J.E.Bridges, "Two-dimensional FDTD analysis of a pulsed microwaved confocal system for breast cancer detection: flxed-focus and antenna-array sensors," IEEE Transactions on Antennas and Propagation, vol. 45, pp. 1470-1479, 1998.

[10] S.C.Hagness, A.Taflove, and J.E.Bridges,"Three-dimensional FDTD analysis of a pulsed microwaved confocal system for breast cancer detection: design of an antenna-array element," IEEE Transactions on Antennas and Propagation, Vol. 47, pp. 783-791, 1999.

[11] E.J.Bond, X.Li, S.C.Hagness, and B.D.Van Veen, "Microwave imaging via space-time beam-forming for early detection of breast cancer," IEEE Transactions on Antennas and Propagation, Vol. 51, no. 8, pp. 1690-1705, 2003.

[12] X.Li, S.K.Davis, S.C.Hagness, D.W.Van der Weide, and B.D.Van Veen, "Microwave imaging via space-time beam-forming: Experimental investigation of tumour detection in multilayer breast phantoms," IEEE Transactions on Microwave Theory and Techniques, Vol. 52, no. 8, pp. 1856-1865, 2004.

[13] P.Kosmas and C.Rappaport, "Time reversal with FDTD method for microwave breast cancer detection," IEEE Trans. Microwave Theory and Techniques, Vol. 53, pp. 2317-2322, 2005.

[14] B.Guo, L.Jian, and H.Zmuda, "A new FDTD formulation for wave propagation in biological media with Cole-Cole model," IEEE Microwave Wireless Component Letters, Vol. 16, pp. 633-635, 2006.

[15] P.Kosmas and C.Rappaport, "FDTD-basedtime reversal for microwave breast cancer detection:Localization in three dimensions ," IEEE Transactions on Microwave Theory and Techniques, vol. 54, pp. 1921-1927, 2006.

[16] P.Kosmas and C.Rappaport, "A matched flter FDTD-based time reversal approach for microwave breast cancer detection ," IEEE Transactions on Antennas and Propagation, Vol. 54, pp. 1257-1264, 2006.

[17] H.N.Patel and D.K.Ghodgaonkar, "Study of effect of numerical breast phantom heterogeneity on dielectric profile reconstruction using microwave imaging," Progress In Electromagnetics Research M, Vol. 58, pp. 135-145, 2017.

Chapter 6

Method of Moments

Method of moments is used to solve electric field integral equation (EFIE) which estimates complex permittivity of 2048 cell human breast model. Matrix formation and inversion time should be reduced to allow large number of cells in breast model. This is achieved by symmetry exploitation using group theory which improve computational efficiency of the imaging system.

EFIE is solved by using method of moments to find scattered electric field due to human breast models. Additive white Gaussian noise is added to this electric field vector. Matrix formed by method of moments is ill posed due to presence of large number of buried cells in inverse scattering formulation [1]. Ill posed system matrix and noise are two major challenges in the solution of inverse scattering problem. Levenberg-Marquardt method is used to solve above challenges. The effects of total volume, multiple view, symmetry and number of cells on complex permittivity reconstruction are investigated in this chapter. The effect of saline and air as surrounding medium on complex permittivity reconstruction is evaluated for microwave breast imaging system.

6.1   Problem Formulation

Microwave signal is transmitted by antennas on breast. This signal is scattered due to its interaction with breast tissues. Scattered electric field at observation point

$\vec{r}$ is calculated by equation (6.1).

$$\vec{E}^s(\vec{r}) = \iiint G(\vec{r}, \vec{r'}) J(\vec{r'}) dv' \tag{6.1}$$

Equation (6.2) is obtained by substituting Green's function $G(\vec{r}, \vec{r'})$ and polarization current density $J(\vec{r'})$ in equation (6.1).

$$\vec{E}^s(\vec{r}) = k_\epsilon^2 \iiint (\epsilon_r(\vec{r'}) - 1) \vec{E}(\vec{r'}) \left[I + \frac{\nabla \nabla}{k_\epsilon^2} \right] \frac{e^{-jk_\epsilon R}}{4\pi R} dv' \tag{6.2}$$

In equation (6.2), $E(\vec{r'})$ is internal electric field at source point $\vec{r'}$, $\nabla \nabla$ is dyadic, R is the distance between observation point and source point, and k_ϵ is wave number of the immersion (surrounding) medium. Relationship among total electric field, incident electric field and scattered electric field is given by equation (6.3).

$$\vec{E}(\vec{r}) = \vec{E}^i(\vec{r}) + \vec{E}^s(\vec{r}) \tag{6.3}$$

Equation (6.4) is obtained by substituting equation (6.2) in equation (6.3).

$$-\vec{E}^i(\vec{r}) = k_\epsilon^2 \iiint (\epsilon_r(\vec{r'}) - 1) \vec{E}(\vec{r'}) \left[I + \frac{\nabla \nabla}{k_\epsilon^2} \right] \frac{e^{-jk_\epsilon R}}{4\pi R} dv' - \vec{E}(\vec{r}) \tag{6.4}$$

Now, Body is divided in N cells. Equation (6.4) is converted into matrix form of equation (6.5) by using method of moments [1, 2, 3, 4].

$$-\vec{E}^i = (A_1 R^\epsilon - I) \vec{E} \tag{6.5}$$

Volume integral of green's function is solved to obtain A_1. Size of A_1 is 3N×3N. R^ϵ is complex permittivity matrix. Size of R^ϵ is 3N×3N. $\vec{E}^i$ is incident electric field matrix in the absence of body. Size of $\vec{E}^i$ is 3N×1. $\vec{E}$ is electric field inside the body. Size of $\vec{E}$ is 3N×1. Equation (6.6) is obtained by writing $(A_1 R^\epsilon - I) = A$ in equation (6.5).

$$-\vec{E}^i = A\vec{E} \tag{6.6}$$

Equation (6.2) is converted into matrix form of equation (6.7) by using method of moments [1, 2, 3, 4].

$$\vec{E}^s = B_1 R^\epsilon \vec{E} \tag{6.7}$$

Volume integral of green's function is solved to obtain B_1. Size of B_1 is 3N×3N. $\vec{E}^s$ is scattered electric field matrix. Size of $\vec{E}^s$ is 3N×1. Equation (6.8) is obtained by writing $B_1 R^\epsilon = B$ in equation (6.7).

$$\vec{E}^s = B\vec{E} \tag{6.8}$$

Incident electric field matrix of equation (6.6) is calculated by placing source. Matrix A of equation (6.6) is known. electric field inside body is only unknown in equation (6.6). Now, electric field inside body of N cells is calculated by inverting matrix A of equation (6.6). Now matrix B and matrix E of equation (6.8) are known. Scattered electric fields at receiver locations are calculated using equation (6.8). This process is known as forward problem. In inverse problem, R^ϵ is only unknown in equation (6.7). The process of obtaining matrix R^ϵ using equation (6.7) is known as inverse problem.

6.2 Computation Reduction using Group Theory

6.2.1 Human Breast Models

Simple human breast model is shown in figure 6.1. It has 16 cells. This model is used to explain group theory. Top and bottom layers of breast model are given in figures 6.2 and 6.3 respectively. Receiver and cell numbers are given in both layers. Complex permittivity is assigned to each cell according to breast anatomy. Complex permittivity is calculated by using equation (6.9).

$$\epsilon_r^*(\omega) = \epsilon_r - j\frac{\sigma}{\omega\epsilon_0} \tag{6.9}$$

In equation 6.9, ϵ_r is relative permittivity, σ is conductivity, ϵ_0 is absolute permittivity, and ω is angular frequency.
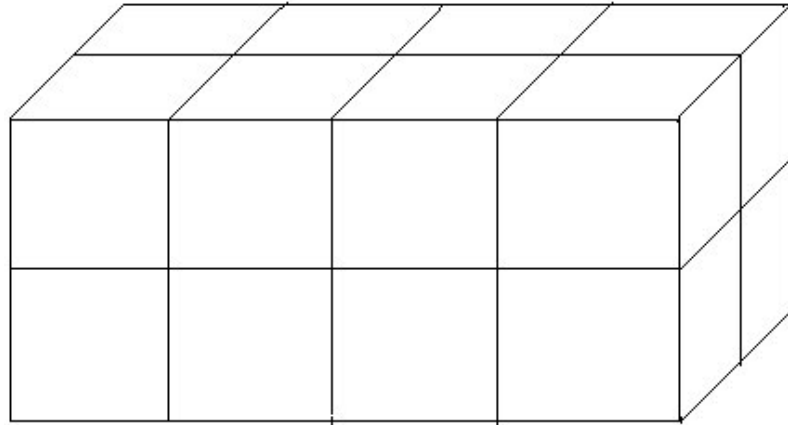
Figure 6.1: Simple human breast model
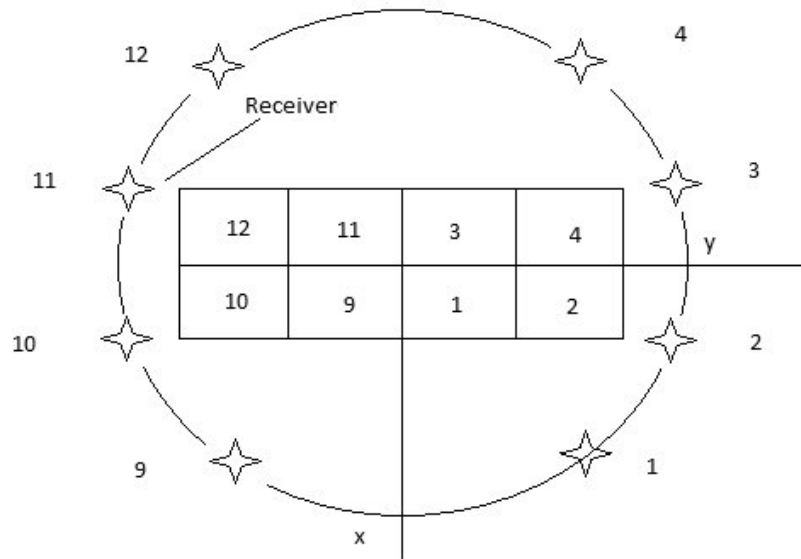
Figure 6.2: Top layer of simple breast model (bi-static system)

2D view of 64 cell breast model is shown in figure 6.4. Volume of 512 cm^3 is assumed for this model. Nipple is represented by layer 1. Skin, milk ducts, fatty tissues, and fibro-glandular tissues are represented by layer 2. Skin, fatty tissues, fibro glandular tissues, and lobules are represented by layer 3. Skin, fatty tissues, fibro-glandular tissues, cancerous tissues are represented by layer 4. In 3D, layer 1 has 4 cells, layer 2 has 16 cells, layer 3 has 20 cells and layer 4 has 24 cells. Above 64 cell model is considered in the simulation. 2D view of 38 cell model is shown in figure 6.5. It is used to evaluate performance of surrounding medium. It has one more layer as compared to 64 cell model.
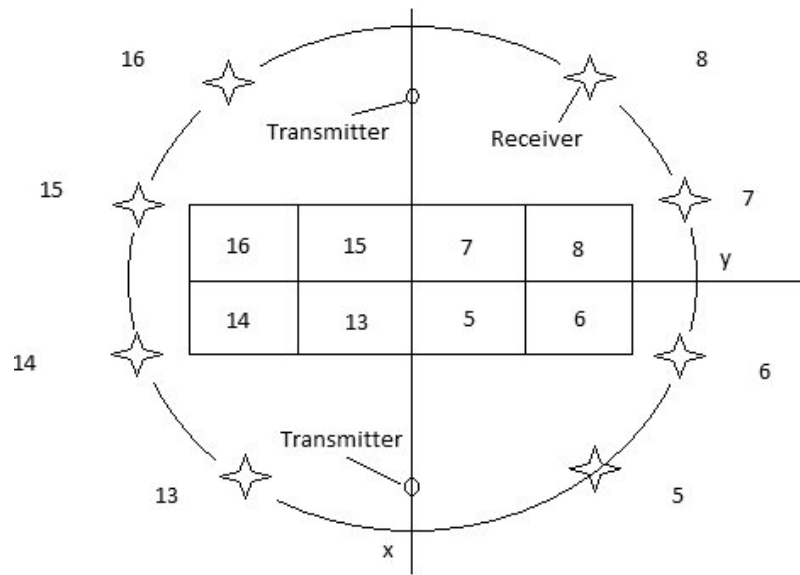
Figure 6.3: Bottom layer of simple breast model (bi-static system)
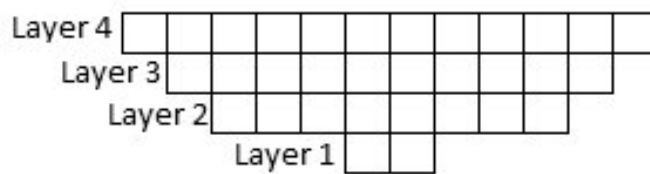
Figure 6.4: 2D view of 64 cell human breast model
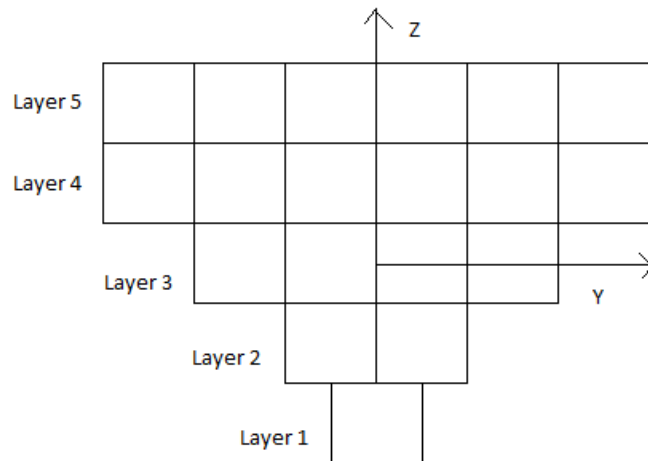
Figure 6.5: 2D view of 38 cell human breast model

6.2.2 Symmetry Exploitation using Group Theory

Matrix B_1 is calculated by solving volume integral of green's function. Sample code for integral of green's fucntion is given in appendix C.4. Structure of matrix

B_1 is shown by equation (6.10).

$$B_1 = \begin{bmatrix} b_{11} & b_{12} & \ldots & b_{1n} \\ b_{21} & b_{22} & \ldots & b_{2n} \\ \cdot & \cdot & \ldots & \cdot \\ \cdot & \cdot & \ldots & \cdot \\ b_{m1} & b_{m2} & \ldots & b_{mn} \end{bmatrix} \qquad (6.10)$$

In equation (6.10), m and n are number of receivers and cells respectively. Each element of B_1 is also 3×3 matrix.

$$b_{11} = \begin{bmatrix} b_{11}^{xx} & b_{11}^{xy} & b_{11}^{xz} \\ \\ b_{11}^{yx} & b_{11}^{yy} & b_{11}^{yz} \\ \\ b_{11}^{zx} & b_{11}^{zy} & b_{11}^{zz} \end{bmatrix} \qquad (6.11)$$

b_{11} element of matrix B_1 is shown by equation (6.11). Each element of matrix B_1 is symmetric [5, 6]. This symmetry of measurement domain is exploited by using group theory. Basic group theory operators are shown by equations (6.12), (6.13) and (6.14).

$$R_1(x, y, z) = (-x, y, z) \qquad (6.12)$$

$$R_2(x, y, z) = (x, -y, z) \qquad (6.13)$$

$$R_3(x, y, z) = (x, y, -z) \qquad (6.14)$$

Group formed by above operators is shown by equation (6.15).

$$G = \{I, R_1, R_2, R_3, R_1R_2, R_2R_3, R_3R_1, R_1R_2R_3\} \qquad (6.15)$$

Octant and Group multiplication table are described in [5, 6]. Now, consider figures 6.2 and 6.3 for next few lines. Receivers and cells numbered as 1,2 have coordinates

(x,y,z), so they are represented by identity element of group. Receivers and cells numbered as 3,4 have coordinates (-x,y,z), so they are represented by R_1 element of group. Receivers and cells numbered as 5,6 have coordinates (x,y,-z), so they are represented by R_3 element of group. Receivers and cells numbered as 7,8 have coordinates (-x,y,-z), so they are represented by $R_1 R_3$ element of group. Receivers and cells numbered as 9,10 have coordinates (x,-y,z), so they are represented by R_2 element of group. Receivers and cells numbered as 11,12 have coordinates (-x,-y,z), so they are represented by $R_1 R_2$ element of group. Receivers and cells numbered as 13,14 have coordinates (x,-y,-z), so they are represented by $R_2 R_3$ element of group. Receivers and cells numbered as 15,16 have coordinates (-x,-y,-z), so they are represented by $R_1 R_2 R_3$ element of group. Equation (6.16) represents transformation matrix [6].

$$V = \frac{1}{2\sqrt{2}} \begin{bmatrix} +I_s & +I_{s1} & +I_{s3} & -I_{s2} & +I_{s2} & -I_{s3} & -I_{s1} & -I_s \\ +I_s & +I_{s1} & -I_{s3} & +I_{s2} & +I_{s2} & -I_{s3} & +I_{s1} & +I_s \\ +I_s & -I_{s1} & +I_{s3} & +I_{s2} & +I_{s2} & +I_{s3} & -I_{s1} & +I_s \\ +I_s & -I_{s1} & -I_{s3} & -I_{s2} & +I_{s2} & +I_{s3} & +I_{s1} & -I_s \\ +I_s & +I_{s1} & +I_{s3} & -I_{s2} & -I_{s2} & +I_{s3} & +I_{s1} & +I_s \\ +I_s & +I_{s1} & -I_{s3} & +I_{s2} & -I_{s2} & +I_{s3} & -I_{s1} & -I_s \\ +I_s & -I_{s1} & +I_{s3} & +I_{s2} & -I_{s2} & -I_{s3} & +I_{s1} & -I_s \\ +I_s & -I_{s1} & -I_{s3} & -I_{s2} & -I_{s2} & -I_{s3} & -I_{s1} & +I_s \end{bmatrix} \tag{6.16}$$

Transformation matrix elements are given by equations (6.17), (6.18), (6.19) and (6.20).

$$I_s = diag(I_0, I_0, ...I_0) \tag{6.17}$$

$$I_{s1} = diag(I_1, I_1, ...I_1) \tag{6.18}$$

$$I_{s2} = diag(I_2, I_2, ...I_2) \tag{6.19}$$

$$I_{s3} = diag(I_3, I_3, ...I_3) \tag{6.20}$$

104

Now, matrices I_0, I_1, I_2 and I_3 are given by equations (6.21), (6.22), (6.23) and (6.24) respectively.

$$I_0 = \begin{bmatrix} 1 & 0 & 0 \\ 0 & 1 & 0 \\ 0 & 0 & 1 \end{bmatrix} \tag{6.21}$$

$$I_1 = \begin{bmatrix} -1 & 0 & 0 \\ 0 & 1 & 0 \\ 0 & 0 & 1 \end{bmatrix} \tag{6.22}$$

$$I_2 = \begin{bmatrix} 1 & 0 & 0 \\ 0 & -1 & 0 \\ 0 & 0 & 1 \end{bmatrix} \tag{6.23}$$

$$I_3 = \begin{bmatrix} 1 & 0 & 0 \\ 0 & 1 & 0 \\ 0 & 0 & -1 \end{bmatrix} \tag{6.24}$$

Matrices B_1, $J^p = R^\epsilon E$, and E_s are block-diagonalized by using equations (6.25), (6.26) and (6.27) respectively.

$$B_{1b} = V B_1 V^T \tag{6.25}$$

$$J_b^p = V J^p \tag{6.26}$$

$$E_b^s = V E^s \tag{6.27}$$

6.3 Inverse Scattering Problem Formulation

Inverse scattering problem is solved by using levenberg-marquardt method [7, 8, 9]. Inverse scattering problem is solved by different methods for microwave breast imaging in [10, 11, 12, 13, 14]. A model driven approach and stochastic optimization

methods are described for microwave breast imaging in [15, 16, 17]. Matrix inversion is needed per iteration in this method. Inverse scattering problem without group theory is solved by using equation (6.28).

$$[\Delta\epsilon] = (J_a^T J_a + \lambda diag(J_a^T J_a))^{-1} J_a^T (\vec{E}^s - \hat{\vec{E}}^s) \qquad (6.28)$$

In equation (6.28), J_a is Jacobian matrix. It is calculated by taking partial derivative of scattered electric field with respect to complex permittivity of each cell. $(\vec{E}^s - \hat{\vec{E}}^s)$ is residual scattered electric field column vector. $[\Delta\epsilon]$ is change in complex permittivity. It is obtained in each iteration. λ is regularization parameter or damping factor. Inverse scattering problem with group theory is solved by using equation (6.29).

$$[\Delta\epsilon] = (J_b^T J_b + \lambda diag(J_b^T J_b))^{-1} J_b^T (\vec{E_b^s} - \hat{\vec{E_b^s}}) \qquad (6.29)$$

In equation (6.29), J_b is Jacobian matrix. It is calculated by taking partial derivative of block diagonalized scattered electric field with respect to complex permittivity of each cell. $(\vec{E_b^s} - \hat{\vec{E_b^s}})$ is residual block diagonalized scattered electric field column vector.

6.4 Simulation Parameters and Noise Consideration

Simulation parameters are given for 64 cell model. Saline is used as surrounding medium. Frequency 500 MHz is considered in simulation, which provides better penetration depth and enough resolution. Complex permittivity values of table 6.1 are used to calculate volume averaged complex permittivity for each cell [18]. Cell size and number of cells vary but volume remains constant during whole simulation process. Radius of the receiver circle is 13 cm. In bi-static system, dipole antenna of 2 cm is used. Two transmitters are at 9 cm from the centre of the body. Size of receiver is same as cell size. Scattered field at receivers' locations is obtained by solving forward problem. Now, noise is added to it by using equation (6.30) and complex permittivity value of each cell is reconstructed by solving inverse scattering

Table 6.1: Complex permittivity values for different breast tissues

Biological Tissues	Complex Permittivity
Breast Fat	5.5- j1.32
Skin dry	44.92-j26.19
Skin wet	48.62-j25.32
Glandular tissues	20-j14.38
Nipple	45-j25.16
Blood vessels	46.23-j21.07
Cancerous tissues	65-j32

problem.

$$\vec{E}^s = B\vec{E} + n \tag{6.30}$$

In equation (6.30), n is additive white gaussian noise column vector. RMSE in complex permittivity is calculated by using equation (6.31).

$$RMSE = \sqrt{\frac{\sum\limits_{i=1}^{K}(\epsilon_i - \hat{\epsilon}_i)^2}{K}} \tag{6.31}$$

In equation (6.31), ϵ_i is an original permittivity value. $\hat{\epsilon}_i$ is reconstructed permittivity value. K is total number of cells used in the model.

6.5 Results

Simulation time is calculated by inverting matrix only once. Now, comparison of matrix inversion time is shown with and without group theory in table 6.2.

Table 6.2: Matrix inversion time in seconds

Number of cells	Matrix inversion time without group theory	Matrix inversion time with group theory
64	0.102	0.0872
512	0.896	0.62
1024	1.982	1.15

Table 6.2 gives clear idea about effect of group theory on matrix inversion time. Matrix inversion time is reduced by applying group theory. Graph of RMSE in
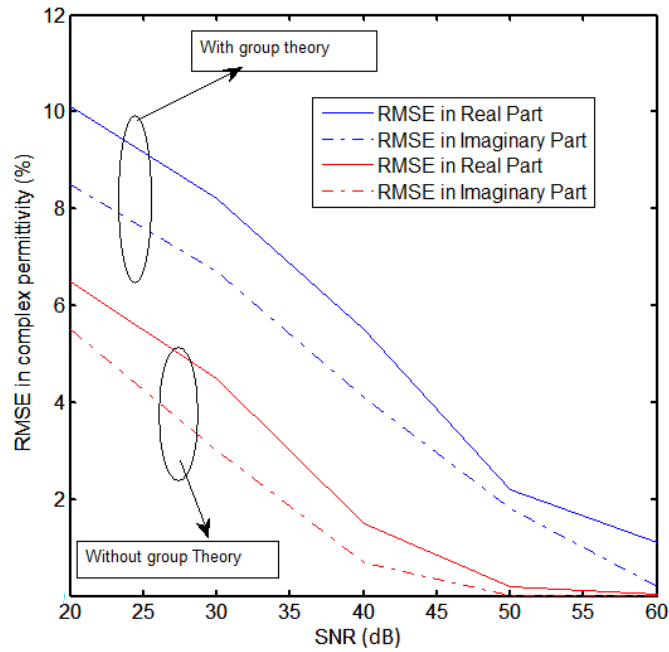
Figure 6.6: RMSE(%) in complex permittivty vs. SNR (dB) (bi-static system)

complex permittivity versus SNR is shown in figure 6.6. RMSE with group theory is higher than RMSE with out group heory. Graph of overall simulation versus number of cells is shown in figure 6.7. Overall simulation time includes time to simulate all iterations with overhead time. Overall simulation time increases with number of
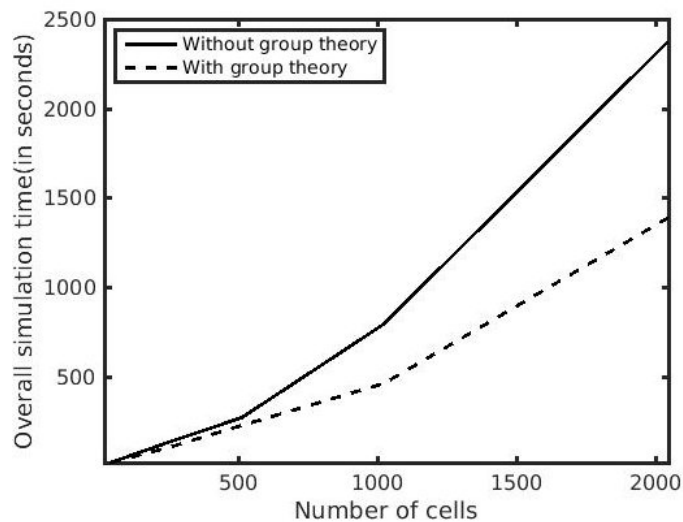
Figure 6.7: Overall simulation time vs. Number of cells

cells. Overall simulation time with group theory is less than that of without group theory. Graph of RMSE in complex permittivity versus SNR is shown in figure 6.8.

It is clear that RMSE with group theory is higher than RMSE without group theory. Graph of RMSE in complex permittivity versus SNR is shown for 38 cell model in figure 6.9. It is quite clear that saline is better surrounding medium as compare to air [1].
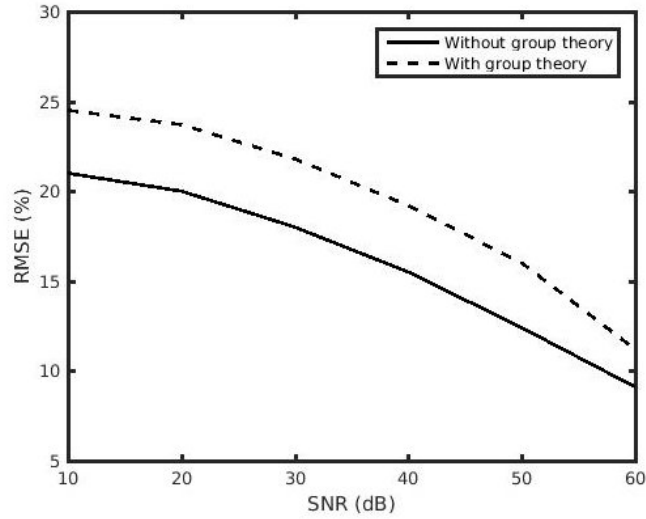
Figure 6.8: RMSE(%) in complex permittivity vs. SNR (dB) for 1024 cells (monostatic system)
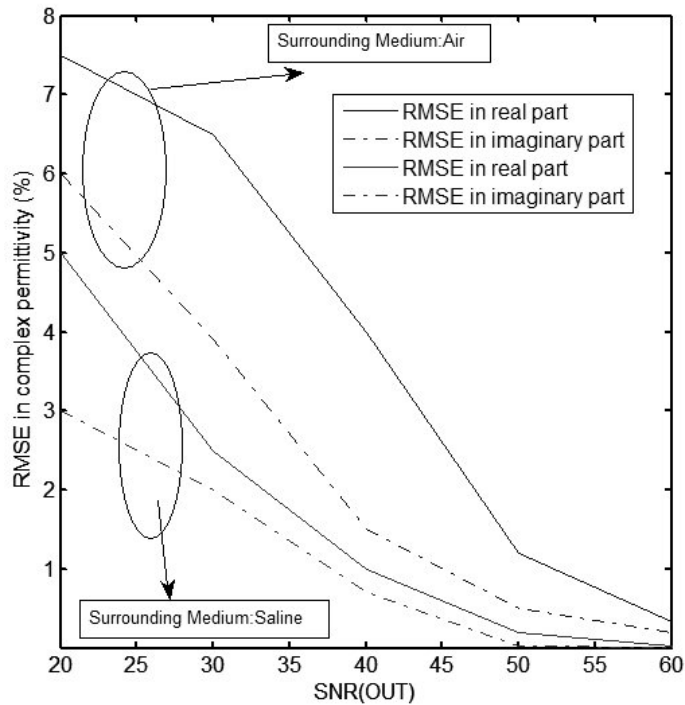
Figure 6.9: RMSE(%) in complex permittivity vs. SNR (dB) for 38 cells (bi-static system)

6.6 Conclusions

Matrix formulation is described by using method of moment for microwave breast imaging. Symmetry is exploited in microwave breast imaging system by using group theory. Overall simulation time is reduced considerably with group theory. By using group theory, approximately 30% to 35% computation time is reduced. Levenberg-Marquardt method is implemented with and without group theory. Matrix inversion with group theory is faster than without group theory because group theory converts matrices in the block diagonalized form. RMSE in complex permittivity is higher with group theory. This is considered as compensation to get computational efficiency. However, for SNR greater than 50 dB, RMSE in complex permittivity without group theory is approximately same as RMSE in complex permittivity with group theory. Overall microwave image reconstruction time is reduced by exploiting symmetry using group theory. The performance of saline is better than air as surrounding medium because it provides better matching with human breasts than air. Multiple view (mono-static system) is better than bi-static system because of redundant measurement data.

References

[1] D.K.Ghodgaonkar, O.P.Gandhi and M.J.Hagmann, "Estimation of complex permittivities of 3D inhomogeneous biological bodies," IEEE Transactions on Microwave Theory and Techniques, Vol. 31, no. 6, pp. 442-446, 1983.

[2] D.E.Livesay and K.Chen. "Electromagnetic fields induced inside arbitrarily shaped biological bodies," IEEE Transactions on Microwave Theory and Techniques, Vol. 22, no. 12, pp. 1273-1280, 1974.

[3] G.W.Hohmann, "Three dimensional induced polarization and electromagnetic modeling," Geophysics, vol. 40, no. 2, pp. 305-324, 1975.

[4] R.F.Harrington, Field Computation by Moment Methods, IEEE Press, pp.1-79, 1993.

[5] D.K.Cohoon, "Reduction of the cost of solving an Integral Equation arising in electromagnetic scattering through the use of group theory," IEEE Transactions on Antennas and Propagation, Vol. 28, no. 1, pp. 104-107,January 1980.

[6] D.K.Ghodgaonkar and R.Ismail, "Exploiting Symmetry in Electromagnetic Imaging Problems by using Group Representation Theory," Bull. Malaysian Math. Sc. Soc., Vol. 23 , no. 1, pp. 33-44, 2000.

[7] T.Rubaek, O.S.Kim, and P.Meincke, "Computational Validation of a 3-D Microwave Imaging System for Breast-Cancer Screening," IEEE Transactions on Antennas and Propagation, Vol. 57, no. 7, pp. 2105-2115, July 2009.

[8] J.D.Zaeytijd, A.Franchois, C.Eyraud, and J.Geffrin, "Full-Wave Three-Dimensional Microwave Imaging With a Regularized Gauss-Newton Method-

Theory and Experiment," IEEE Transactions on Antennas and Wave Propagation, Vol. 55, no. 11, pp. 3279-3292, November 2007.

[9] C.S.Park, B.S.Jeong, "Reconstruction of a high contrast and large object by using the hybrid algorithm combining a Levenberg-Marquardt algorithm and a genetic algorithm," IEEE Transactions on Magnetics, Vol. 35, no. 3, pp. 1582-1585, May 1999.

[10] T.Rubaek, P.M.Meaney, P.Meincke, and K.D.Paulsen, "Nonlinear microwave imaging for breast-cancer screening using Gauss-Newton's method and the CGLS inversion algorithm," IEEE Transactions on Antennas and Propagation, Vol. 55, no. 8, pp. 2320-2331, August 2007.

[11] Q.Fang, P.M.Meaney, and K.D.Paulsen. "Singular value analysis of the Jacobian matrix in microwave image reconstruction," IEEE Transactions on Antennas and Propagation, Vol. 54, no. 8, pp. 2371-2380, 2006.

[12] M.M.Ney, A.M.Smith, S.S.Stuchly, "A Solution of Electromagnetic Imaging Using Pseudoinverse Transformation," IEEE Transactions on Medical Imaging, Vol.3 , Issue: 4, pp. 155-162, Dec 1984.

[13] C.Pichot, L.Jofre, G.Peronnet, J.Bolomey, "Active microwave imaging of Inhomogeneous bodies," IEEE Transactions on Antennas and Propagation, Vol. AP-33, No. 4, pp.416-425, April 1985.

[14] L.Garnero, A.Franchois, J.Hugonin, C.Pichot, and N.Joachimowicz, "Microwave Imaging complex permittivity reconstruction by simulated annealing," IEEE Transaction on Microwave Theory and Techniques, Vol. 39, No. 11, pp.1801-1807, November 1991.

[15] K.Belkebir, R.E.Kleinman, and C.Pichot, "Microwave Imaging Location and Shape Reconstruction from Multifrequency Scattering Data," IEEE Transaction on microwave theory and techniques, Vol.45, No. 4, pp. 469-476, April 1997.

[16] S.Caorsi, G.L.Gragnani, M.Pastorino, and Mauro Rebagliati, "A Model driven

approach to microwave diagnostics in biomedical applications," IEEE Transactions on Microwave Theory and Techniques, Vol.44, No.10, October 1996.

[17] M.Pastorino, "Stochastic Optimization Methods Applied to Microwave Imaging:A Review," IEEE Transactions on Antennas and Propagation, Vol.55, No.3, pp.538-548, March 2007.

[18] D.Andreuccetti, R.Fossi and C.Petrucci: An Internet resource for the calculation of the dielectric properties of body tissues in the frequency range 10 Hz - 100 GHz. Website at http://niremf.ifac.cnr.it/tissprop/. IFAC-CNR, Florence (Italy), 1997. Based on data published by C.Gabriel et al. in 1996.

[19] D.M.Pozar, Microwave Engineering, John Wiley and sons, pp.1-243,547-593, 1989.

[20] S.A.Dianat, E.S.Saber, Advanced Linear Algebra for Engineers with MATLAB, CRC Press, pp. 1-302, 2009.

[21] H.N.Patel and D.K.Ghodgaonkar,"Computationally efficient microwave imaging of human breast model using group theory" IEEE MTT-S International Microwave and RF Conference,10-12 December 2015, Hyderabad, pp. 81-84.

[22] H.N.Patel and D.K.Ghodgaonkar,"The effect of noise on complex permittivity reconstruction in mathematical breast model", IEEE International Conference on Systems in Medicine and Biology, 4-7 January 2016, IIT Kharagpur, pp. 13-16.

Chapter 7

Conclusions and Suggestions for Future Work

7.1 Conclusions

Breast cancer incidences and mortality rate are increasing throughout the world. Microwave radiation are non ionizing as opposed to X-rays so, they offer relative safety as compared with X-rays. It is very difficult to detect cancer in class III and IV breasts by using X-rays based mammography. Microwave imaging can complement mammography due to its high contrast between malignant and healthy breast tissues.

Multiple frequency inverse scattering problem formulation of microwave breast imaging system is computationally efficient because complex number computations are avoided. 3D level set based optimization method has better shape reconstruction capability. Dielectric properties of healthy and malignant breast tissues are reconstructed by using two 3D level set functions based optimization. Performance of 3D level set based optimization is improved by using regularization. The performance of TV regularization is better than Tikhonov regularization for medium, small and very small breast tumours. TV regularization reconstructs shape and size of very small tumour but it fails to reconstruct exact location of very small tumour. Better 3D reconstruction is achieved by using regularized 3D level set based optimization for at least 20 dB SNR in measured electric field data.

Electric field computation in heterogeneous numerical breast phantom is very efficient using 3D FDTD method because it solves Maxwell's equations on grids by using iterative process. Dispersion and polarization properties of breast tissues are

easily incorporated in 3D FDTD update equations. 3D FDTD solves forward problem efficiently during each iteration of 3D level set method which leads to better reconstruction of complex permittivity. Normalized reflected power varies with direction of wave propagation in heterogeneous numerical breast phantom. FDTD can solve forward problem for multiple frequencies with millions of cells.

Microwave imaging problem can be solved at a single frequency by using method of moment. Matrix inversion is required in method of moments which imposes limitation on number of cells. So it is limited to 2048 cells. However, this limit is extended to several extent by using group theory. Symmetry is exploited in microwave breast imaging system by using group theory. By using group theory, approximately 30% to 35% computation time is reduced. Performance of saline is better than air as surrounding medium because it provides better matching than air.

FDTD method is computationally efficient and accurate as compared to MoM because there is no requirement of matrix inversion in FDTD. 3D level set based optimization is computationally efficient and accurate as compared to Levenberg-Marquardt method. Overall, better performance in complex permittivity reconstruction is achieved by using 3D level set based optimization and FDTD method.

7.2   Suggestions for Future Work

1. 3D level set based optimization can be applied to more complex numerical breast phantoms with more than two level set functions.

2. More number of frequencies can be included in the implementation of 3D level set based optimization for best complex permittivity reconstruction.

3. Hybrid algorithm can be proposed by combining 3D level set method with other algorithms (e.g.,particle swarm optimization, simulated annealing and ant colony optimization) for best complex permittivity reconstruction.

4. Multiple frequency inverse scattering problem of this work can be solved by deep learning approaches for best complex permittivity reconstruction [1].

References

[1] K.H.Jin, M.T.McCann, E.Froustey, and M.Unser, "Deep convolutional neural network for inverse problems in imaging." IEEE Transactions on Image Processing, Vol.26, No. 9, pp. 4509-4522. Sep. 2017.

Appendix A

Numerical Breast Phantom, Antenna Placement and Immersion (Surrounding) Medium

A.1 Numerical Breast Phantom

Anatomically realistic numerical breast phantoms are required to make reliable microwave breast imaging system. 3D view of class III numerical breast phantom is shown in figure A.1 [1]. Breast density classification is discussed in the introduc-

Figure A.1: 3D view of numerical breast phantom

tion. Class III or class IV numerical breast phantoms is obvious choice for testing microwave breast imaging system. Y-Z, X-Z, and X-Y views of class III numerical breast phantom are shown in figure A.2. Fibro-glandular tissues are represented by white (bright) colour and adipose tissues are represented by black or gray (dark) colour. MRI derived numerical breast phantom makes imaging system more realis-
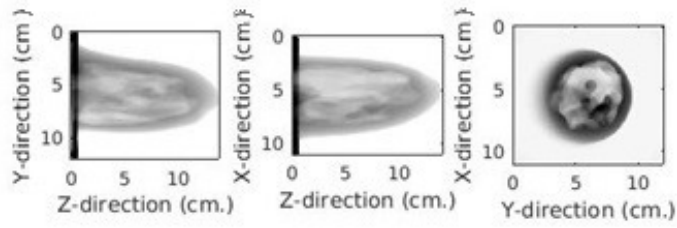
Figure A.2: Y-Z, X-Z and X-Y view of class 3 MRI derived numerical breast phantom.

tic because it captures heterogeneity well. In numerical breast phantom, dielectric properties of fibro-glandular and adipose breast tissues are assigned to regions with one and zero, respectively.

A.2 Antenna Placement Surrounding Numerical Breast Phantom

Antenna placement surrounding numerical breast phantom for inverse scattering problem formulation is discussed in this appendix. Antenna placement is shown in figure A.3. Middle point of numerical breast phantom is origin of coordinate system.
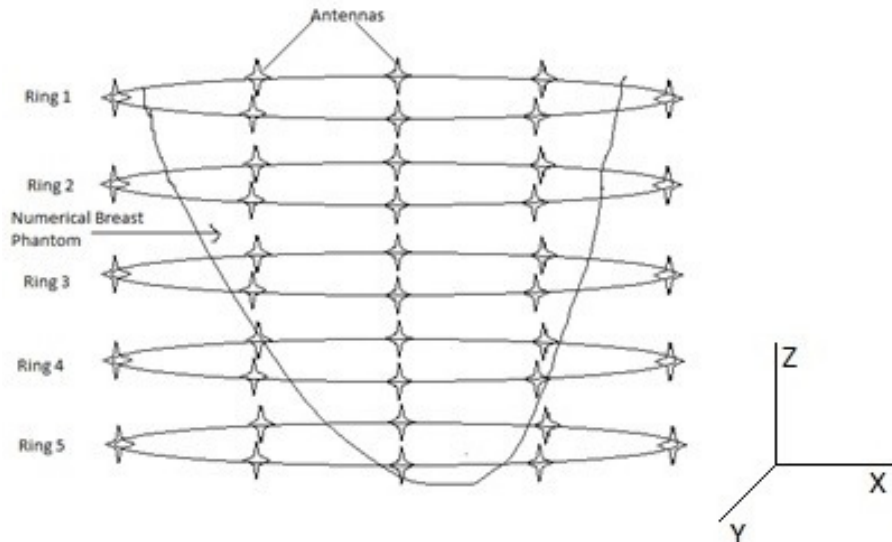
Figure A.3: Antenna placement surrounding the numerical breast phantom.

There are five rings of antennas around numerical breast phantom [2]. Each circular ring has eight short dipole of length 1cm, which lead to 40 antennas in the system.

Distance between two consecutive rings is 3 cm. Radius of each ring is 6 cm.

A.3   Immersion (Surrounding) Medium

Surrounding medium is required in microwave breast imaging system for better matching with human breast model. Oil based surrounding medium is considered in this microwave breast imaging system [2, 3]. Infinite frequency permittivity (ϵ_∞) of this surrounding medium is 2.6 because it matches the average dielectric properties of the human breast tissues. Difference permittivity ($\Delta\epsilon$) and static conductivity (σ_s) are zero for this surrounding medium.

Method of moment is a frequency domain method. Saline is used as surrounding medium in method of moments [4]. Performance of saline is better than air as surrounding medium because it provides better matching than air. Error in complex permittivity reconstruction is less for saline as surounding medium.

References

[1] Zastrow, E., S. K. Davis, M. Lazebnik, F. Kelcz, B. D. Van Veen, and S. C. Hagness, "Development of anatomically realistic numerical breast phantoms with accurate dielectric properties for modelling microwave interactions with the human breast," IEEE Transactions on Biomedical Engineering, Vol. 55, no. 12, pp. 2792-2800, 2008.

[2] J. D., Shea, P. Kosmas, S. C. Hagness, and B. D. Van Veen, "Three-dimensional microwave imaging of realistic numerical breast phantoms via a multiple-frequency inverse scattering technique," Medical Physics, Vol. 37, no. 8, pp. 4210-4226, 2010.

[3] H.N.Patel and D.K.Ghodgaonkar,"3D level set based optimization of inverse scattering problem for microwave breast imaging", IEEE MTT-S International Microwave Bio Conference, 15-17 May 2017, Gothenburg, Sweden, pp. 1-4.

[4] D.K.Ghodgaonkar, O.P.Gandhi and M.J.Hagmann, "Estimation of complex permittivities of 3D inhomogeneous biological bodies," IEEE Transactions on Microwave Theory and Techniques, Vol. 31, no. 6, pp. 442-446, 1983.

Appendix B

Important Derivations

B.1 Debye Model

The biological molecules are polar molecules with relaxation frequencies in the range of high frequency (HF) to microwave frequencies. Complex permittivity of human breast tissues is function of temperature and frequency. Temperature is assumed to be constant. Dispersion and polarization effect of human breast tissues are incorporated by using single pole Debye model given by equation (B.4).

Transient response of dielectric medium is shown in figure B.1 [1]. D is electric
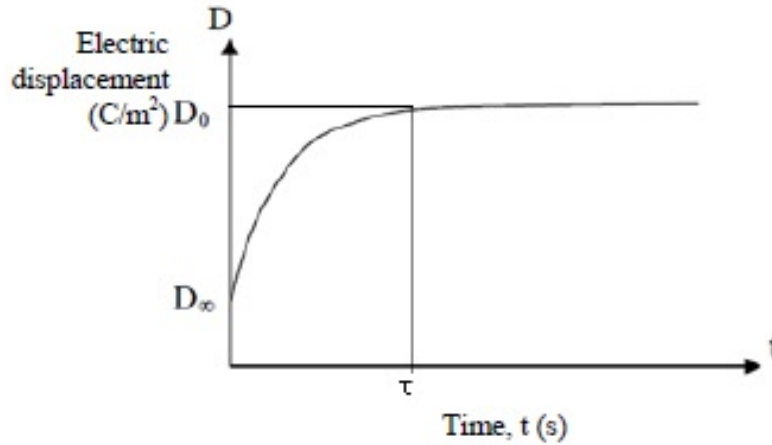
Figure B.1: Transient response of dielectric medium.

displacement, τ is relaxation time constant. D_∞ is initial value of electric displacement. D_0 is final value of electric displacement. Situation of figure B.1 is expressed

in terms of equation (B.1).

$$D = D_\infty + (D_0 - D_\infty)(1 - e^{-\frac{t}{\tau}}) \tag{B.1}$$

Now, equation (B.2) is obtained by substituting $D = \epsilon_0 \epsilon_r E$, $D_\infty = \epsilon_0 \epsilon_\infty E$ and $D_0 = \epsilon_0 \epsilon_s E$ in equation (B.1).

$$\epsilon_r = \epsilon_\infty + (\epsilon_s - \epsilon_\infty)(1 - e^{-\frac{t}{\tau}}) \tag{B.2}$$

In equation (B.2), ϵ_r is relative permittivity, ϵ_∞ is infinite (high) frequency permittivity, ϵ_s is static (low) frequency permittivity. Now, equation (B.3) is obtained by applying Laplace transform to equation (B.2).

$$\frac{\epsilon_r}{s} = \frac{\epsilon_\infty}{s} + \frac{(\epsilon_s - \epsilon_\infty)}{s} - \frac{(\epsilon_s - \epsilon_\infty)}{s + \frac{1}{\tau}} \tag{B.3}$$

In order to obtain equation (B.4), equation (B.3) is simplified after multiplying both sides by s and substituting $s = j\omega$.

$$\epsilon_r = \epsilon_\infty + \frac{(\epsilon_s - \epsilon_\infty)}{1 + j\omega\tau} \tag{B.4}$$

B.2   Derivation of Electric Field Update Equations for Numerical Breast Phantom Region

FDTD electric field update equation is derived by using polarization density equation. The polarization property of human breast tissues is included by substituting Debye model into the ampere's law equation. All derivations are done by assuming air as surrounding medium. In case of specific surrounding medium replace impedance and velocity of light values according to surrounding medium.

$$\nabla \times \vec{H} = \epsilon_0 \epsilon_\infty j\omega \vec{E} + j\omega\epsilon_0 \frac{\Delta\epsilon}{1 + j\omega\tau} \vec{E} + \sigma_s \vec{E} \tag{B.5}$$

σ_s is static conductivity. $\Delta\epsilon$ is difference between static permittivity and infinite permittivity. Equation (B.6) is obtained by rearranging equation (B.5).

$$\nabla \times \vec{H} = \epsilon_0\epsilon_\infty j\omega\vec{E} + +\sigma_s\vec{E} + j\omega\epsilon_0\frac{\Delta\epsilon}{1+j\omega\tau}\vec{E} \tag{B.6}$$

Polarization current density equation is important for derivation of the FDTD electric field update equations. Equation of polarization current density is given below.

$$\vec{J}_p = j\omega\epsilon_0\frac{\Delta\epsilon}{1+j\omega\tau}\vec{E} \tag{B.7}$$

$\vec{J}_p$ is polarization current density vector and $\vec{E}$ is electric field intensity vector. Equation (B.8) is obtained by rearranging equation (B.7).

$$\vec{J}_p(1+j\omega\tau) = j\omega\epsilon_0\Delta\epsilon\vec{E} \tag{B.8}$$

By applying Inverse Fourier transform.

$$\vec{J}_p + \tau\frac{\partial\vec{J}_p}{\partial t} = \epsilon_0\Delta\epsilon\frac{\partial\vec{E}}{\partial t} \tag{B.9}$$

Now, By applying FDTD [2] and rearranging terms

$$\frac{\tau}{\Delta t}\vec{J}_P^{t+\Delta t}\left(1+\frac{\Delta t}{2\tau}\right) = \frac{\tau}{\Delta t}\vec{J}_P^t\left(1-\frac{\Delta t}{2\tau}\right) + \epsilon_0\Delta\epsilon\frac{\vec{E}_{t+\Delta t}-\vec{E}_t}{\Delta t} \tag{B.10}$$

Whatever the time-constant τ is, it can be expressed as multiple of the time-step, $\tau = N_t\Delta t$ where N_t does not need to be an integer. Put $\tau = N_t\Delta t$ and multiplying both sides by $\Delta x = \delta$

$$\delta\vec{J}_P^{t+\Delta t} = \left(\frac{1-\frac{1}{2N_t}}{1+\frac{1}{2N_t}}\right)\delta\vec{J}_P^t + \left(\frac{\epsilon_0\Delta\epsilon\delta}{N_t\Delta t\cdot(1+\frac{1}{2N_t})}\right)(\vec{E}_{t+\Delta t}-\vec{E}_t) \tag{B.11}$$

$$\delta\vec{J}_P^{t+\Delta t} = (mj1)\delta\vec{J}_P^t + (mj2)(\vec{E}_{t+\Delta t}-\vec{E}_t) \tag{B.12}$$

123

Divide both sides by $\Delta x = \delta$ to get polarization current density equation.

$$\delta \vec{J}_P^{t+\frac{\Delta t}{2}} = \frac{\delta \vec{J}_P^{t+\Delta t} + \delta \vec{J}_P^t}{2} \tag{B.13}$$

By applying Inverse Fourier transform to equation (B.6)

$$\nabla \times \vec{H}_{t+\frac{\Delta t}{2}} = \epsilon_0 \epsilon_\infty \frac{\partial \vec{E}}{\partial t} + \sigma_s \vec{E} + \vec{J}_P^{t+\frac{\Delta t}{2}} \tag{B.14}$$

By applying FDTD and Multiplying both sides by $\Delta x = \delta$.

$$\delta \nabla \times \vec{H}_{t+\frac{\Delta t}{2}} = \delta \epsilon_0 \epsilon_\infty \frac{\vec{E}_{t+\Delta t} - \vec{E}_t}{\Delta t} + \delta \sigma_s \frac{\vec{E}_{t+\Delta t} + \vec{E}_t}{2} + \delta \vec{J}_P^{t+\frac{\Delta t}{2}} \tag{B.15}$$

By substituting $\delta J_P^{t+\frac{\Delta t}{2}}$ in above equation

$$\delta \nabla \times \vec{H}_{t+\frac{\Delta t}{2}} = \delta \epsilon_0 \epsilon_\infty \frac{\vec{E}_{t+\Delta t} - \vec{E}_t}{\Delta t} + \delta \sigma_s \frac{\vec{E}_{t+\Delta t} + \vec{E}_t}{2} +$$
$$1/2[(1+mj1)\delta \vec{J}_P^t + mj2(\vec{E}_{t+\Delta t} - \vec{E}_t)] \tag{B.16}$$

By rearranging above equation after normalizing electric field vector.

$$\frac{\delta \epsilon_0 \epsilon_\infty}{\Delta t}\left(1 + \frac{\sigma_s \Delta t}{2\epsilon_0 \epsilon_\infty} + \frac{\Delta t \cdot mj2}{2\delta \epsilon_0 \epsilon_\infty}\right)\vec{E}_{t+\Delta t} =$$
$$\frac{\delta \epsilon_0 \epsilon_\infty}{\Delta t}\left(1 - \frac{\sigma_s \Delta t}{2\epsilon_0 \epsilon_\infty} + \frac{\Delta t \cdot mj2}{2\delta \epsilon_0 \epsilon_\infty}\right)\vec{E}_t +$$
$$\frac{\delta}{\eta_0}\nabla \times \vec{H}_{t+\frac{\Delta t}{2}} - \frac{1}{2}(1+mj1)\delta \vec{J}_P^t \tag{B.17}$$

Electric field update equation is given by equation (B.18)

$$\vec{E}_{t+\Delta t} = \frac{\left(1 - \frac{\sigma_s \Delta t}{2\epsilon_0 \epsilon_\infty} + \frac{\Delta t \cdot mj2}{2\delta \epsilon_0 \epsilon_\infty}\right)}{\left(1 + \frac{\sigma_s \Delta t}{2\epsilon_0 \epsilon_\infty} + \frac{\Delta t \cdot mj2}{2\delta \epsilon_0 \epsilon_\infty}\right)}\vec{E}_t + \frac{c_0 \Delta t}{2\delta \epsilon_\infty \left(1 + \frac{\sigma_s \Delta t}{2\epsilon_0 \epsilon_\infty} + \frac{\Delta t \cdot mj2}{2\delta \epsilon_0 \epsilon_\infty}\right)} \cdot$$
$$\left(2\delta \nabla \times \vec{H}_{t+\frac{\Delta t}{2}} - \eta_0(1+mj1)\delta \vec{J}_P^t\right) \tag{B.18}$$

By substituting $\dfrac{\left(1-\frac{\sigma_s\Delta t}{2\epsilon_0\epsilon\infty}+\frac{\Delta t\cdot mj2}{2\delta\epsilon_0\epsilon\infty}\right)}{\left(1+\frac{\sigma_s\Delta t}{2\epsilon_0\epsilon\infty}+\frac{\Delta t\cdot mj2}{2\delta\epsilon_0\epsilon\infty}\right)} = me1$ and $\dfrac{c_0\Delta t}{2\delta\epsilon\infty\left(1+\frac{\sigma_s\Delta t}{2\epsilon_0\epsilon\infty}+\frac{\Delta t\cdot mj2}{2\delta\epsilon_0\epsilon\infty}\right)} = me2$

$$\vec{E}_{t+\Delta t} = me1\cdot\vec{E}_t + me2\cdot[(2\Delta x\cdot\nabla\times\vec{H}_{t+\frac{\Delta t}{2}})-$$
$$(\eta_0\cdot(1+mj1)\cdot\Delta x\cdot\vec{J}_P^t)] \tag{B.19}$$

B.3   Derivation of Electric Field Update Equations for PML Region

PML is required at grid boundaries to avoid reflection of microwave signals in FDTD. Artificial losses in x direction is given below [3, 4].

$$S_x = \begin{bmatrix} \left(1+\frac{\sigma_x}{j\omega\epsilon_0}\right)^{-1} & 0 & 0 \\ 0 & \left(1+\frac{\sigma_x}{j\omega\epsilon_0}\right) & 0 \\ 0 & 0 & \left(1+\frac{\sigma_x}{j\omega\epsilon_0}\right) \end{bmatrix} \tag{B.20}$$

σ_x in above matrix is defined as below.

$$\sigma_x = \frac{0.5\epsilon_0}{\Delta t}\left(\frac{x}{L_x}\right)^3 \tag{B.21}$$

In above equation, L_x is length of PML in x direction. x is particular cell number of PML. Artificial losses in Y direction is given below.

$$S_y = \begin{bmatrix} \left(1+\frac{\sigma_y}{j\omega\epsilon_0}\right) & 0 & 0 \\ 0 & \left(1+\frac{\sigma_y}{j\omega\epsilon_0}\right)^{-1} & 0 \\ 0 & 0 & \left(1+\frac{\sigma_y}{j\omega\epsilon_0}\right) \end{bmatrix} \tag{B.22}$$

In above equation, L_y is length of PML in z direction. z is particular cell number of PML. Artificial losses in Z direction is given below.

$$S_z = \begin{bmatrix} \left(1+\frac{\sigma_z}{j\omega\epsilon_0}\right) & 0 & 0 \\ 0 & \left(1+\frac{\sigma_z}{j\omega\epsilon_0}\right) & 0 \\ 0 & 0 & \left(1+\frac{\sigma_z}{j\omega\epsilon_0}\right)^{-1} \end{bmatrix} \tag{B.23}$$

Artificial losses in all three directions can be combined as

$$[S] = [S_x][S_y][S_z] \tag{B.24}$$

Ampere law equation can be written to incorporate artificial losses in all directions.

$$\nabla \times \vec{H} = j\omega[S]\vec{D} \tag{B.25}$$

Writing x component of above equation after substituting [S] in it.

$$j\omega \left(1 + \frac{\sigma_x}{j\omega\epsilon_0}\right)^{-1} \left(1 + \frac{\sigma_y}{j\omega\epsilon_0}\right) \left(1 + \frac{\sigma_z}{j\omega\epsilon_0}\right) D_x = \\ \left[\frac{\partial H_z}{\partial y} - \frac{\partial H_y}{\partial z}\right] \tag{B.26}$$

By substituting $\left[\frac{\partial H_z}{\partial y} - \frac{\partial H_y}{\partial z}\right] = (CH)_x$ and rearranging terms.

$$j\omega \left(1 + \frac{\sigma_y}{j\omega\epsilon_0}\right) \left(1 + \frac{\sigma_z}{j\omega\epsilon_0}\right) D_x = \left(1 + \frac{\sigma_x}{j\omega\epsilon_0}\right)(CH)_x \tag{B.27}$$

Equation (B.28) by simplifying equation (B.27).

$$j\omega D_x + \frac{\sigma_y + \sigma_z}{\epsilon_0} D_x + \frac{\sigma_y\sigma_z}{j\omega\epsilon_0^2} D_x = (CH)_x + \frac{\sigma_x}{j\omega\epsilon_0}(CH)_x \tag{B.28}$$

By applying Inverse Fourier Transform

$$\frac{\partial}{\partial t} D_x + \frac{\sigma_y + \sigma_z}{\epsilon_0} D_x + \frac{\sigma_y\sigma_z}{\epsilon_0^2} \int_{-\infty}^{t} D_x d\tau = (CH)_x + \\ \frac{\sigma_x}{\epsilon_0} \int_{-\infty}^{t} (CH)_x d\tau \tag{B.29}$$

By applying FDTD and normalizing electric field density component.

$$\frac{D_x^{t+\Delta t} - D_x^t}{\Delta t} + \frac{\sigma_y + \sigma_z}{\epsilon_0} \frac{D_x^{t+\Delta t} + D_x^t}{2} + \frac{\sigma_y\sigma_z\Delta t}{\epsilon_0^2} \left[\frac{D_x^{t+\Delta t} + D_x^t}{4} + \sum_{T=0}^{t} D_x\right] \\ = c_0 CH_x + \frac{c_0\sigma_x}{\epsilon_0} \sum_{T=0}^{t+\frac{\Delta t}{2}} CH_x \tag{B.30}$$

By rearranging above equation.

$$
\begin{aligned}
D_x^{t+\Delta t} = {} & \frac{\left(\frac{1}{\Delta t} - \frac{\sigma_y + \sigma_z}{2\epsilon_0} - \frac{\sigma_y \cdot \sigma_z \cdot \Delta t}{4\epsilon_0^2}\right)}{\left(\frac{1}{\Delta t} + \frac{\sigma_y + \sigma_z}{2\epsilon_0} + \frac{\sigma_y \cdot \sigma_z \cdot \Delta t}{4\epsilon_0^2}\right)} D_x^t + \frac{c_0 \cdot CH_x}{\left(\frac{1}{\Delta t} + \frac{\sigma_y + \sigma_z}{2\epsilon_0} + \frac{\sigma_y \cdot \sigma_z \cdot \Delta t}{4\epsilon_0^2}\right)} \\
& + \frac{c_0 \cdot \Delta t \cdot \sigma_x}{\left(\frac{1}{\Delta t} + \frac{\sigma_y + \sigma_z}{2\epsilon_0} + \frac{\sigma_y \cdot \sigma_z \cdot \Delta t}{4\epsilon_0^2}\right) \cdot \epsilon_0} (Ich)_x - \frac{\Delta t \cdot \sigma_y \cdot \sigma_z \cdot ID_x}{\left(\frac{1}{\Delta t} + \frac{\sigma_y + \sigma_z}{2\epsilon_0} + \frac{\sigma_y \cdot \sigma_z \cdot \Delta t}{4\epsilon_0^2}\right) \cdot \epsilon_0^2}
\end{aligned}
\tag{B.31}
$$

Electric field can be updated as given below.

$$
E_x = \frac{D_x}{\epsilon_{xx}}
\tag{B.32}
$$

Electric field update equations in y and z directions are obtained by repeating above procedure.

B.4   Power Calculations

Power calculations is extremely important to validate the implementation. Steps are given below to calculate power [2].

- Transverse wave vector expansion

$$
\vec{k}_{xy}(m,n) = k_x(m)\hat{x} + k_y(n)\hat{y}
\tag{B.33}
$$

$k_x(m)\hat{x}$ and $k_y(n)\hat{y}$ are wave vectors in above equation.

$$
k_x(m) = \frac{2\pi m}{S_x}
\tag{B.34}
$$

S_x is total number of cells in x direction. m is varying from $-S_x/2$ to $+S_x/2$.

$$
k_y(n) = \frac{2\pi n}{S_y}
\tag{B.35}
$$

S_y is total number of cells in y direction. n is varying from $-S_y/2$ to $+S_y/2$.

- Longitudinal wave vector expansion for reflection and transmission.

$$k_{zr}(m,n) = \sqrt{(k_0 n_{ref})^2 - k_x^2(m) - k_y^2(n)} \qquad \text{(B.36)}$$

$$k_{zt}(m,n) = \sqrt{(k_0 n_{tm})^2 - k_x^2(m) - k_y^2(n)} \qquad \text{(B.37)}$$

k_0 is wave number for free space. n_{ref} and n_{tm} are refractive indices of reflection and transmission respectively on grid.

- Normalize reflected and transmitted fields using source field

- Calculate spatial harmonics $Sp_{xr}, Sp_{yr}, Sp_{xt}, Sp_{yt}$ by using FFT.

- Now find Sp_z.

$$Sp_{zr} = -(k_x. * Sp_{xr} + k_y. * Sp_{yr})./k_{zr} \qquad \text{(B.38)}$$

$$Sp_{zt} = -(k_x. * Sp_{xt} + k_y. * Sp_{yt})./k_{zt} \qquad \text{(B.39)}$$

- Calculate diffraction efficiencies

$$Spref = abs(Sp_{xr}).^2 + abs(Sp_{yr}).^2 + abs(Sp_{zr}).^2 \qquad \text{(B.40)}$$

$$Sptrn = abs(Sp_{xt}).^2 + abs(Sp_{yt}).^2 + abs(Sp_{zt}).^2 \qquad \text{(B.41)}$$

$$ref = real(k_{zr}/kzinc). * Spref \qquad \text{(B.42)}$$

$$trn = real(k_{zt}/kzinc). * Sptrn \qquad \text{(B.43)}$$

$$REF(nfreq) = sum(ref(:)) \qquad \text{(B.44)}$$

$$TRN(nfreq) = sum(trn(:)) \qquad\qquad (B.45)$$

REF and TRN are reflected and transmitted powers due to numerical breast phantom.

References

[1] Ikram-e-Khuda, Sabira Khatun, Khondker Jahid Reza, Md. Mijanur Rahman, Md.Moslemuddin Fakir, "Improved Debye Model for Experimental Approximation of Human Breast Tissue Properties at 6 GHz Ultra-Wideband Centre Frequency", International Journal of Engineering and Technology, Vol. 5, no. 6, pp. 4708-4717, 2013.

[2] John B. Schneider, "Understanding the Finite-Difference Time-Domain Method," pp. 33-308, www.eecs.wsu.edu/ schneidj/ufdtd, 2010.

[3] Gedney, S. D., "An anisotropic perfectly matched layer-absorbing medium for the truncation of FDTD lattices," IEEE Transactions on Antennas and Propagation, Vol. 44, no. 12, pp. 1630-1639, 1996

[4] Computational electromagnetic lecture 9, available at http://emlab.utep.edu/ee5390cem/Lecture 9–Perfectly Matched Layer.pdf, accessed January 2015

Appendix C

MATLAB Sample Codes

C.1 Multiple Frequency Inverse Scattering Problem Formulation

Multiple frequency inverse scattering matrix formulation is implemented by this code.

```
clc;
clear all;
close all;

u0 = 4*pi*10^-9;
mu0 = u0;
e0 = 8.854*10^-14;
del_l = 0.5;
a = ((3/(4*pi))^(1/3))*del_l;
u1 = [1 0 0];
u2 = [0 1 0];
u3 = [0 0 1];
dx = 0.5;
dy = 0.5;
dz = 0.5;
Nx1 = 40;
Ny1 = 40;
```

```
Nz1 = 40;
c=3e10;
Nv = Nx1*Ny1*Nz1;
Nfreq = 4;
f = 5e8;
f1 = 5e8;
f2 = 2e8;
Na = 40;
MF = Na*Nfreq;
freq = linspace(f1,f2,Nfreq);
k= 2*pi./(c./freq);
w = 2*pi.*freq;
xn = zeros(Nv,Nfreq);
yn = zeros(Nv,Nfreq);
zn = zeros(Nv,Nfreq);
ed = zeros(Nx1,Ny1,Nz1);
einf = ones(Nx1,Ny1,Nz1);
sigd =  zeros(Nx1,Ny1,Nz1);
tau = 15e-12;
w = 2*pi.*freq;
cinf = 1;
cdel = 1./(1+1i*w.*tau);
csig = 1./(1i*w.*e0);
L = 0.01;
Iz = 0.000001;
n = 377;
i0 =0.000001;
l=0.01;
Na=40;
N = 40;
```

```matlab
[z, y, x] = ndgrid(.5:N); %// note reverse order to ...
   get desired order of result
vc1 = [x(:) y(:) z(:)]; %// desired result
m(1:64000,1:3) = 20;
vc2 = m-vc1;
vc = vc2*0.5;
for i=1:Nv
    rL(:,:,i)=vc(i,:);
end

for i = 1:5
rm(:,:,1+8*(i-1)) = [15 0 6.75-4*(i-1)];
rm(:,:,2+8*(i-1)) = [10.61 10.61 6.75-4*(i-1)];
rm(:,:,3+8*(i-1))= [0 15 6.75-4*(i-1)];
rm(:,:,4+8*(i-1)) = [-10.61 10.61 6.75-4*(i-1)];
rm(:,:,5+8*(i-1))= [-15 0 6.75-4*(i-1)];
rm(:,:,6+8*(i-1)) = [-10.61 -10.61 6.75-4*(i-1)];
rm(:,:,7+8*(i-1)) = [0 -15 6.75-4*(i-1)];
rm(:,:,8+8*(i-1)) = [10.61 -10.61 6.75-4*(i-1)];
end

for m = 1:Na
  for p = 1:Nfreq
    for n = 1:Nv
     r=((rL(1,1,n)-rm(1,1,m))^2+(rL(1,2,n)-rm(1,2,m))^2+
        (rL(1,3,n)-rm(1,3,m))^2)^0.5;
     r=1;
     x1 = rL(1,1,n)-rm(1,1,m);
     y1 = rL(1,2,n)-rm(1,2,m);
     c = k(p)*r;
     d = 1/c;
```

```matlab
        e = 1/c.^2;
        er(n,p) = ...
            ((n*i0*l*x1)/(2*pi*r^3))*(1-1i*d)*exp(-1i*c);
        eth(n,p) = ((1i*n*k(p)*i0*l*y1)/(4*pi*r^2))*...
                    (1-1i*d-e)*exp(-1i*c);
        ephi(n,p) = 0;
    end
  end


 [x,y,z] = sph2cart(eth,ephi,er);
 xn = xn+x;
 yn=yn+y;
 zn=zn+z;
end


for m=1:Nv
 rfx1(:,:,m) = rL(:,:,m) + ( (-1)^1*(del_l/2)).*u1;
 rfx2(:,:,m) = rL(:,:,m) + ( (-1)^2*(del_l/2)).*u1;
 rfy1(:,:,m) = rL(:,:,m) + ( (-1)^1*(del_l/2)).*u2;
 rfy2(:,:,m) = rL(:,:,m) + ( (-1)^2*(del_l/2)).*u2;
 rfz1(:,:,m) = rL(:,:,m) + ( (-1)^1*(del_l/2)).*u3;
 rfz2(:,:,m) = rL(:,:,m) + ( (-1)^2*(del_l/2)).*u3;
end



for m=1:Na
  for n =1:Nv
    rml(m,n) = ((rm(1,1,m)-rL(1,1,n))^2 +
                (rm(1,2,m)-rL(1,2,n))^2 +
                (rm(1,3,m)-rL(1,3,n))^2)^0.5;
    rx1(m) = ((rm(1,1,m)-rfx1(1,1,m))^2 +
```

```
                   (rm(1,2,m)-rfx1(1,2,m))^2 +
                   (rm(1,3,m)-rfx1(1,3,m))^2)^0.5;
      rx2(m) = ((rm(1,1,m)-rfx2(1,1,m))^2 +
                   (rm(1,2,m)-rfx2(1,2,m))^2 +
                   (rm(1,3,m)-rfx2(1,3,m))^2)^0.5;
      ry1(m) = ((rm(1,1,m)-rfy1(1,1,m))^2 +
                   (rm(1,2,m)-rfy1(1,2,m))^2 +
                   (rm(1,3,m)-rfy1(1,3,m))^2)^0.5;
      ry2(m) = ((rm(1,1,m)-rfy2(1,1,m))^2 +
                   (rm(1,2,m)-rfy2(1,2,m))^2 +
                   (rm(1,3,m)-rfy2(1,3,m))^2)^0.5;
      rz1(m) = ((rm(1,1,m)-rfz1(1,1,m))^2 +
                   (rm(1,2,m)-rfz1(1,2,m))^2 +
                   (rm(1,3,m)-rfz1(1,3,m))^2)^0.5;
      rz2(m) = ((rm(1,1,m)-rfz2(1,1,m))^2 +
                   (rm(1,2,m)-rfz2(1,2,m))^2 +
                   (rm(1,3,m)-rfz2(1,3,m))^2)^0.5;
   end
end


for m = 1:Na
 for n =1:Nv
   for p = 1:Nfreq
   [y,z] = meshgrid(rL(1,2,n)-(del_l/2):dy:
           rL(1,2,n)+(del_l/2),rL(1,3,n)-(del_l/2):dz:
           rL(1,3,n)+(del_l/2));
   [x,z1] = meshgrid(rL(1,1,n)-(del_l/2):dx:
           rL(1,1,n)+(del_l/2),
           rL(1,3,n)-(del_l/2):dz:rL(1,3,n)+(del_l/2));
   [x1,y1] = meshgrid(rL(1,1,n)-(del_l/2):dx:
```

```matlab
                rL(1,1,n)+(del_l/2),
                rL(1,2,n)-(del_l/2):dy:rL(1,2,n)+(del_l/2));


%   "Gmlxx element"
    rxx1_n = ((rm(1,1,m)-rfx1(1,1,n)).^2 +
        (rm(1,2,m)-y).^2 + (rm(1,3,m)-z).^2).^0.5;
    rxx2_n = ((rm(1,1,m)-rfx2(1,1,n)).^2 +
        (rm(1,2,m)-y).^2 + (rm(1,3,m)-z).^2).^0.5;
    Gxx1=((1+1i*k(p).*rxx1_n)./(4*pi.*(rxx1_n).^3)).*
        exp(-1i*k(p).*rxx1_n).*(rm(1,1,m)-rfx1(1,1,n));
    Gxx2=((1+1i*k(p).*rxx2_n)./(4*pi.*(rxx2_n).^3)).*
        exp(-1i*k(p).*rxx2_n).*(rm(1,1,m)-rfx2(1,1,n));
    IGxx1 = sum(sum(Gxx1))*(dy*dz);
    IGxx2= sum(sum(Gxx2))*(dy*dz);
    B1(p+(m-1)*4,1+(n-1)*1) = ...
        ((exp(-1i*k(p).*rml(m,n)))./
    (k(p).*rml(m,n)))*
    (sin(k(p)*a)-(k(p)*a*cos(k(p)*a)))-IGxx1+IGxx2;
    A1(p+(m-1)*4,1+(n-1)*1) = exp(-1i*k(p)*a)*
        (1+(1i*k(p)*a))-1;
   end
  end
 end
xn  = xn';
[Ogn] = VOXELISE(Nx1,Ny1,Nz1,
        'ClassIII_printed_phantom.stl','xyz');
Ogn = +Ogn;


delx1 = 1;
dely1 = 1;
delz1 = 1;
```

```matlab
xa = (1:Nx1)*delx1;
xa = xa-mean(xa);


ya = (1:Ny1)*dely1;
ya = ya-mean(ya);


za = (1:Nz1)*delz1;
za = za-mean(za);


r = 12;


r2 = 15;
[Xa,Ya,Za] = meshgrid(xa,ya,za);



A =  ((Xa+1).^2+(Ya).^2) <= r^2;
B= +A;
A2 = ((Xa).^2+(Ya).^2) <= r2^2;
B2 = +A2;

for nz=1:Nz1
  for nx=1:Nx1
    for ny = 1:Ny1
      if(Ogn(nx,ny,nz)==0&&B(nx,ny,nz)==1)
        ed(nx,ny,nz) = 35.6;
        einf(nx,ny,nz) = 18.6-2.6;
        sigd(nx,ny,nz) = 0.00817;
      elseif(Ogn(nx,ny,nz)==1&&B(nx,ny,nz)==1)
        ed(nx,ny,nz) = 3.54;
        einf(nx,ny,nz) = 4.09-2.6;
```

```
              sigd(nx,ny,nz) = 0.000842;
          else
              einf(nx,ny,nz) =2.6;
              ed(nx,ny,nz)=1;
              sigd(nx,ny,nz) = 0.0001;
          end
      end
  end
end


for nx = 1:Nx1
    for ny = 1:Ny1
        for nz = 1:Nz1
          deinf(((Nx1*Ny1)*(nx-1))+(Ny1*(ny-1))+nz,1)=
          einf(nx,ny,nz);
          dedel(((Nx1*Ny1)*(nx-1))+(Ny1*(ny-1))+nz,1)=
          ed(nx,ny,nz);
          dsigs(((Nx1*Ny1)*(nx-1))+(Ny1*(ny-1))+nz,1)=
          sigd(nx,ny,nz);
        end
    end
end


x = [deinf;dedel;dsigs];


for nm = 1:Na
    for nk = 1:Nv
      nf =1 ;
      Ain(1+(nm-1)*Nfreq,nk) = cinf*w(nf)^2*mu0*e0*
              B1(1+(nm-1)*Nfreq,nk)*xn(nf,nk);
      Adel(1+(nm-1)*Nfreq,nk) = cdel(nf)*(w(nf)^2)*mu0*e0*
```

```
            B1(1+(nm-1)*Nfreq,nk)*xn(nf,nk);
   Asig(1+(nm-1)*Nfreq,nk) = csig(nf)*(w(nf)^2)*mu0*e0*
            B1(1+(nm-1)*Nfreq,nk)*xn(nf,nk);


nf = 2;


Ain(2+(nm-1)*Nfreq,nk) = cinf*w(nf)^2*mu0*e0*
         B1(2+(nm-1)*Nfreq,nk)*xn(nf,nk);
Adel(2+(nm-1)*Nfreq,nk) = cdel(nf)*(w(nf)^2)*mu0*e0*
        B1(2+(nm-1)*Nfreq,nk)*xn(nf,nk);
Asig(2+(nm-1)*Nfreq,nk) = csig(nf)*(w(nf)^2)*mu0*e0*
         B1(2+(nm-1)*Nfreq,nk)*xn(nf,nk);


nf = 3;


Ain(3+(nm-1)*Nfreq,nk) = cinf*w(nf)^2*mu0*e0*
       B1(3+(nm-1)*Nfreq,nk)*xn(nf,nk);
Adel(3+(nm-1)*Nfreq,nk) = cdel(nf)*(w(nf)^2)*mu0*e0*
       B1(3+(nm-1)*Nfreq,nk)*xn(nf,nk);
Asig(3+(nm-1)*Nfreq,nk) = csig(nf)*(w(nf)^2)*mu0*e0*
      B1(3+(nm-1)*Nfreq,nk)*xn(nf,nk);


nf = 4;


Ain(4+(nm-1)*Nfreq,nk) = cinf*w(nf)^2*mu0*e0*
      B1(4+(nm-1)*Nfreq,nk)*xn(nf,nk);
Adel(4+(nm-1)*Nfreq,nk) = cdel(nf)*(w(nf)^2)*mu0*e0*
      B1(4+(nm-1)*Nfreq,nk)*xn(nf,nk);
Asig(4+(nm-1)*Nfreq,nk) = csig(nf)*(w(nf)^2)*mu0*e0*
     B1(4+(nm-1)*Nfreq,nk)*xn(nf,nk);
end
```

```matlab
    end


for nm = 1:MF
  for nk = 1:Nv
    A11(1+(nm-1)*2,nk) = real(Ain(nm,nk));
    A11(2+(nm-1)*2,nk) = imag(Ain(nm,nk));
    A22(1+(nm-1)*2,nk) = real(Adel(nm,nk));
    A22(2+(nm-1)*2,nk) = imag(Adel(nm,nk));
    A33(1+(nm-1)*2,nk) = real(Asig(nm,nk));
    A33(2+(nm-1)*2,nk) = imag(Asig(nm,nk));
  end
end


A= [A11 A22 A33];


b = A*x;
```

C.2   Signed Distance Function Generation

Signed distance function calculation is extremely important in 3D level set based optimization. Signed distance function is implemented by using this code.

```matlab
clear all;
close all;
clc;

% Initialize FDTD Parameters
Nx = 80;
Ny = 80;
Nz = 80;
Sx = 20;
Sy = 20;
Sz = 20;
c0a = 3e10;
f = 7e8;
nimp = 377;
e0 = 8.854e-14;
mu0 = 4*pi*1e-9;
NPML = [20 20 20 20 20 20];
delx = 0.5;%Sx/Nx
dely = 0.5;%Sy/Ny;
delz = 0.5;%Sz/Nz;
delt = 9e-12;
%T = 1.11e-08;
steps = 1500;%4000;
%steps = 5;
delts = 13.5e-12;
```

```matlab
[X,Y,Z] = meshgrid(1:Nx,1:Ny,1:Nz);
z0 = (mu0/e0)^0.5;
Nx1 = 40;
Ny1 = 40;
Nz1 = 40;
[X1,Y1,Z1] = meshgrid(1:Nx1,1:Ny1,1:Nz1);
sdfth=zeros(Nx,Ny,Nz);
sdfd=zeros(Nx,Ny,Nz);
sdf=zeros(Nx,Ny);
sdfe=zeros(Nx,Ny,Nz);
Og = zeros(Nx,Ny,Nz);
delx1 = 1;%Sx/Nx
dely1 = 1;%Sy/Ny;
delz1 = 1;%Sz/Nz;
%Voxelise the STL:
nx1 = 21;
nx2 = 60;
ny1 = 21;
ny2 = 60;
nz1 = 21;
nz2 = 60;
[Ogn] = VOXELISE(Nx1,Ny1,Nz1,
'ClassIII_printed_phantom.stl','xyz');
Ogn = +Ogn;
Ogn = 1-Ogn;

for nx = 21:60
    for ny = 21:60
        for nz = 21:60
            Og(nx,ny,nz) = Ogn(nx-20,ny-20,nz-20);
        end
```

```matlab
        end
end


for nz = 21:60
    sdf = Og(34:42,36:44,nz);
    sdfe(34:42,36:44,nz) = edge(sdf);
end


sdfd(27:55,25:52,:) = bwdist(sdfe(27:55,25:52,:));


for nz = 21:60
  for ny = 21:60
    for nx = 21:60
     if (Og(nx,ny,nz)==0)
        sdfth(nx,ny,nz) = -1*sdfd(nx,ny,nz);
      elseif(Og(nx,ny,nz)==1)
        sdfth(nx,ny,nz) = 1*sdfd(nx,ny,nz);
     end
    end
  end
end


for nx = 21:60
  for ny = 21:60
    for nz = 21:60
      if (sdfth(nx,ny,nz)>=15)
        sdfth(nx,ny,nz)=15;
      end
      if (sdfth(nx,ny,nz)<=-15)
        sdfth(nx,ny,nz)=-15;
      end
```

```matlab
        end
    end
end

sdfth = sdfth/15;
figure('color','w')
slice(sdfth,[],[],32);
whitebg('w')
shading interp
colormap gray
colorbar
axis off
view(2)
```

C.3 3D FDTD

3D FDTD electric field and magnetic filed update equations are used on discrete grid to find electric field profile in the numerical breast phantom. 3D FDTD is implemented to visualize electric field by using this code.

```
clear all;
close all;
clc;
% Initialize FDTD Parameters
Nx = 40;
Ny = 40;
Nz = 40;
Sx = 20;
Sy = 20;
Sz = 20;
c0a = 3e10;
iNx = 25;
iNy = 25;
iNz = 25;
m=0;
nimp = 377;
e0 = 8.854e-14;
mu0 = 4*pi*1e-9;
NPML = [5 5 5 5 5 5];
delx = 0.5;%Sx/Nx
dely = 0.5;%Sy/Ny;
delz = 0.5;%Sz/Nz;
delt1 = 1.8e-12;
delt = 5*delt1;
%T = 1.11e-08;
```

```matlab
steps = 1000;%4000;
%steps = 5;
delts1 = 2.7e-12;
delts = 5*delts1;
ft1 = 7;
ft2 = 34;
ft11 = 7;
ft22 = 34;
Ae = 0.4;
Ah = -0.4/233;
[X,Y,Z] = meshgrid(1:Nx,1:Ny,1:Nz);
z0 = (mu0/e0)^0.5;
Nx1 = 40;
Ny1 = 40;
Nz1 = 40;
delx1 = 1;%Sx/Nx
dely1 = 1;%Sy/Ny;
delz1 = 1;%Sz/Nz;
%Voxelise the STL:
nx1 = 7;
nx2 = 34;
ny1 = 7;
ny2 = 34;
nz1 = 1;
nz2 = 40;
[x1,y1,z1] = meshgrid(1:Nx1,1:Ny1,1:Nz1);
einfx1 = zeros(40,40,40);
edx1 = zeros(40,40,40);
sigdx11 = zeros(40,40,40);
[Ogn] = VOXELISE(Nx,Ny,Nz,
'ClassIII_printed_phantom.stl','xyz');
```

146

```matlab
%Ogn = 1-Ogn;
Og = zeros(Nx,Ny,Nz);
Bn = zeros(Nx,Ny,Nz);
B1n = zeros(Nx,Ny,Nz);
xa = (1:Nx)*delx1;
xa = xa-mean(xa);
ya = (1:Ny)*dely1;
ya = ya-mean(ya);
za = (1:Nz)*delz1;
za = za-mean(za);
r = 12;
r1 = 13;
[Xa,Ya,Za] = meshgrid(xa,ya,za);
    A =  ((Xa+1).^2+(Ya).^2) <= r^2;
    A1 =  ((Xa+1).^2+(Ya).^2) <= r1^2;
    B= +A;
    B1 = +A1;
    B1 = and(B1,Ogn);
    B4 = or(B1,Ogn);
% Initalize Reflection and transmittance parameters
Nfreq = 20;
f1 = 5e8;
f2 = 2.5e9;
FREQ = linspace(f1,f2,Nfreq);
k = exp(-1i*2*pi*delt.*FREQ);
tau = 0.5/f2;
t0 = 6*tau;
k0= (2*pi)./(c0a./FREQ);
srcfx = zeros(iNx,iNy,Nfreq);
srcfy = zeros(iNx,iNy,Nfreq);
srcfxy = zeros(iNx,iNz,Nfreq);
```

```matlab
srcfzy = zeros(iNx,iNz,Nfreq);
srcfyx = zeros(iNy,iNz,Nfreq);
srcfzx = zeros(iNy,iNz,Nfreq);
nref = 7;
ntra = 34;
P=  (-(floor((iNx)/2)):(floor((iNx)/2)))';
M = (-(floor((iNy)/2)):(floor((iNy)/2)))';
N =(-(floor((iNz)/2)):(floor((iNz)/2)))';
kx = -2*pi*P/12.5;
ky = -2*pi*M/12.5;
kz = -2*pi*N/12.5;
[kxz,kyz] = meshgrid(kx,ky);
[kyx,kzx] = meshgrid(kz,ky);
[kxy,kzy] = meshgrid(kz,kx);


% Initialize all fields and integrations to zero

Hx = zeros(Nx,Ny,Nz);
Hy = zeros(Nx,Ny,Nz);
Hz = zeros(Nx,Ny,Nz);
Ex = zeros(Nx,Ny,Nz);
Ey = zeros(Nx,Ny,Nz);
Ez = zeros(Nx,Ny,Nz);
Dx = zeros(Nx,Ny,Nz);
Dy = zeros(Nx,Ny,Nz);
Dz = zeros(Nx,Ny,Nz);
Icex = zeros(Nx,Ny,Nz);
Icey = zeros(Nx,Ny,Nz);
Icez = zeros(Nx,Ny,Nz);
IHx = zeros(Nx,Ny,Nz);
IHy = zeros(Nx,Ny,Nz);
```

```
IHz = zeros(Nx,Ny,Nz);
Ichx = zeros(Nx,Ny,Nz);
Ichy = zeros(Nx,Ny,Nz);
Ichz = zeros(Nx,Ny,Nz);
IDx = zeros(Nx,Ny,Nz);
IDy = zeros(Nx,Ny,Nz);
IDz = zeros(Nx,Ny,Nz);
Exsrc = zeros(Nx,Ny,Nz);
Eysrc = zeros(Nx,Ny,Nz);
Exsrcy = zeros(Nx,Ny,Nz);
Ezsrcy = zeros(Nx,Ny,Nz);
Eysrcx = zeros(Nx,Ny,Nz);
Ezsrcx = zeros(Nx,Ny,Nz);
Hxsrc = zeros(Nx,Ny,Nz);
Hysrc = zeros(Nx,Ny,Nz);
Hxsrcy = zeros(Nx,Ny,Nz);
Hzsrcy = zeros(Nx,Ny,Nz);
Hysrcx = zeros(Nx,Ny,Nz);
Hzsrcx = zeros(Nx,Ny,Nz);
muxx = ones(Nx,Ny,Nz);
muyy = ones(Nx,Ny,Nz);
muzz = ones(Nx,Ny,Nz);
exx = ones(Nx,Ny,Nz);
eyy = ones(Nx,Ny,Nz);
ezz = ones(Nx,Ny,Nz);
einfx = ones(Nx,Ny,Nz);
einfy = ones(Nx,Ny,Nz);
einfz = ones(Nx,Ny,Nz);
Ntx = ones(Nx,Ny,Nz);
Nty = ones(Nx,Ny,Nz);
Ntz = ones(Nx,Ny,Nz);
```

149

```
ed = zeros(Nx,Ny,Nz);
einf = ones(Nx,Ny,Nz);
sigd =  zeros(Nx,Ny,Nz);
edx = zeros(Nx,Ny,Nz);
edy = zeros(Nx,Ny,Nz);
edz = zeros(Nx,Ny,Nz);
cjjx =  zeros(Nx,Ny,Nz);
cjex = zeros(Nx,Ny,Nz);
cjjy =  zeros(Nx,Ny,Nz);
cjey = zeros(Nx,Ny,Nz);
cjjz =  zeros(Nx,Ny,Nz);
cjez = zeros(Nx,Ny,Nz);
sigdx1 = zeros(Nx,Ny,Nz);
sigdy1 = zeros(Nx,Ny,Nz);
sigdz1 = zeros(Nx,Ny,Nz);
jpx = zeros(Nx,Ny,Nz);
jpy = zeros(Nx,Ny,Nz);
jpz = zeros(Nx,Ny,Nz);
srcx = zeros(iNx,iNy);
srcy = zeros(iNx,iNy);

for nz=nz1:nz2
  for nx=nx1:nx2
    for ny = ny1:ny2
     if (mod(nz,10)==0)
      m= m+3;
      r = 12-m;
      r1 = 13-m;
      A2 =  ((Xa+1).^2+(Ya).^2) <= r^2;
      A3 = ((Xa+1).^2+(Ya).^2) <= r1^2;
      B2 = +A2;
```

```matlab
            B3 = +A3;
          end
        end
    end
end
%


for nz=nz1:nz2
    for nx=nx1:nx2
        for ny = ny1:ny2
            if(Ogn(nx,ny,nz)==0&&B1(nx,ny,nz)==0)
             edx(nx,ny,nz) = 35.6;
             einfx(nx,ny,nz) = 18.6;
             sigdx1(nx,ny,nz) = 0.00817;
            elseif(Ogn(nx,ny,nz)==1 && B1(nx,ny,nz)==1)
             edx(nx,ny,nz) = 3.54;
             einfx(nx,ny,nz) = 4.09;
             sigdx1(nx,ny,nz) = 0.000842;
            end
        end
    end
end

for nz=nz1:nz2
  for ny=ny1:ny2
    for nx = nx1:nx2
      edz(nx,ny,nz) = edx(nz,nx,ny);
      einfz(nx,ny,nz) = einfx(nz,nx,ny);
      sigdz1(nx,ny,nz) = sigdx1(nz,nx,ny);
    end
  end
```

```matlab
    end


for ny=ny1:ny2
  for nx=nx1:nx2
    for nz = nz1:nz2
     edy(nx,ny,nz) = edx(ny,nx,nz);
     einfy(nx,ny,nz) = einfx(ny,nx,nz);
     sigdy1(nx,ny,nz) = sigdx1(ny,nx,nz);
    end
  end
end



for nx =nx1:nx2
  for ny=ny1:ny2
    for nz =nz1:nz2
     if(Bn(nx,ny,nz)>0.6)
       Ntx(nx,ny,nz) = 1.667;
       Nty(nx,ny,nz) = 1.667;
       Ntz(nx,ny,nz) = 1.667;
     end
   end
  end
end

% Build UPML on grid

Nx2 = 2*Nx;
Ny2 = 2*Ny;
Nz2 = 2*Nz;
```

```matlab
sigx = zeros(Nx2,Ny2,Nz2);

for nx = 1:2*NPML(1)
 nx1 = 2*NPML(1)-nx+1;
 sigx(nx1,:,:) = (0.5*e0/delt)*(nx/2/NPML(1))^3;
end

for nx = 1:2*NPML(2)
 nx1 = Nx2-2*NPML(2)+nx;
 sigx(nx1,:,:) = (0.5*e0/delt)*(nx/2/NPML(2))^3;
end

sigy = zeros(Nx2,Ny2,Nz2);

for ny = 1:2*NPML(3)
  ny1 = 2*NPML(3)-ny+1;
  sigy(:,ny1,:) = (0.5*e0/delt)*(ny/2/NPML(3))^3;
end

for ny = 1:2*NPML(4)
  ny1 = Ny2-2*NPML(4)+ny;
  sigy(:,ny1,:) = (0.5*e0/delt)*(ny/2/NPML(4))^3;
end

sigz = zeros(Nx2,Ny2,Nz2);

for nz = 1:2*NPML(5)
  nz1 = 2*NPML(5)-nz+1;
  sigz(:,:,nz1) = (0.5*e0/delt)*(nz/2/NPML(5))^3;
end
```

```matlab
for nz = 1:2*NPML(6)
  nz1 = Nz2-2*NPML(6)+nz;
  sigz(:,:,nz1) = (0.5*e0/delt)*(nz/2/NPML(6))^3;
end



% Calculate UPML update coeffieicnts
sighxx = sigx(1:2:Nx2,2:2:Ny2,2:2:Nz2);
sighyx = sigy(1:2:Nx2,2:2:Ny2,2:2:Nz2);
sighzx = sigz(1:2:Nx2,2:2:Ny2,2:2:Nz2);


sighxy = sigx(2:2:Nx2,1:2:Ny2,2:2:Nz2);
sighyy = sigy(2:2:Nx2,1:2:Ny2,2:2:Nz2);
sighzy = sigz(2:2:Nx2,1:2:Ny2,2:2:Nz2);


sighxz = sigx(2:2:Nx2,2:2:Ny2,1:2:Nz2);
sighyz = sigy(2:2:Nx2,2:2:Ny2,1:2:Nz2);
sighzz = sigz(2:2:Nx2,2:2:Ny2,1:2:Nz2);


sigdxx = sigx(2:2:Nx2,1:2:Ny2,1:2:Nz2);
sigdyx = sigy(2:2:Nx2,1:2:Ny2,1:2:Nz2);
sigdzx = sigz(2:2:Nx2,1:2:Ny2,1:2:Nz2);


sigdxy = sigx(1:2:Nx2,2:2:Ny2,1:2:Nz2);
sigdyy = sigy(1:2:Nx2,2:2:Ny2,1:2:Nz2);
sigdzy = sigz(1:2:Nx2,2:2:Ny2,1:2:Nz2);


sigdxz = sigx(1:2:Nx2,1:2:Ny2,2:2:Nz2);
sigdyz = sigy(1:2:Nx2,1:2:Ny2,2:2:Nz2);
sigdzz = sigz(1:2:Nx2,1:2:Ny2,2:2:Nz2);
```

```
for nx = 1:Nx
        for ny = 1:Ny
                for nz = 1:Nz


mhx0(nx,ny,nz)=(1/delt)+((sighyx(nx,ny,nz)+sighzx(nx,ny,nz))/
 (2*e0))+(sighyx(nx,ny,nz)*sighzx(nx,ny,nz)*delt/(4*e0^2));
mhx1(nx,ny,nz) = (1/mhx0(nx,ny,nz))*((1/delt)-
((sighyx(nx,ny,nz)+sighzx(nx,ny,nz))/(2*e0))-
 (sighyx(nx,ny,nz)*sighzx(nx,ny,nz)*delt/(4*e0^2)));
%mhx2(nx,ny,nz) = ...
    -(1/mhx0(nx,ny,nz))*(c0a/(muxx(nx,ny,nz)*
einfx(nx,ny,nz)));
mhx2(nx,ny,nz) = ...
    -(1/mhx0(nx,ny,nz))*(c0a/(muxx(nx,ny,nz)));
mhx3(nx,ny,nz) = ...
    -(1/mhx0(nx,ny,nz))*(c0a*delt*sighxx(nx,ny,nz)/
 (e0*muxx(nx,ny,nz)));
mhx4(nx,ny,nz) = ...
    -(1/mhx0(nx,ny,nz))*(delt*sighyx(nx,ny,nz)
*sighzx(nx,ny,nz)/e0^2);


mhy0(nx,ny,nz) = (1/delt)+((sighxy(nx,ny,nz)+
sighzy(nx,ny,nz))/(2*e0))+
((sighxy(nx,ny,nz)*sighzy(nx,ny,nz)*delt)/(4*e0^2));
mhy1(nx,ny,nz) = (1/mhy0(nx,ny,nz))*((1/delt)-
((sighxy(nx,ny,nz)+sighzy(nx,ny,nz))/(2*e0))-
(sighxy(nx,ny,nz)*sighzy(nx,ny,nz)*delt/(4*e0^2)));
%mhy2(nx,ny,nz) = ...
    -(1/mhy0(nx,ny,nz))*(c0a/(muyy(nx,ny,nz)
*einfy(nx,ny,nz)));
```

```
mhy2(nx,ny,nz) = ...
    -(1/mhy0(nx,ny,nz))*(c0a/(muyy(nx,ny,nz)));
mhy3(nx,ny,nz) = ...
    -(1/mhy0(nx,ny,nz))*(c0a*delt*sighyy(nx,ny,nz)/
(e0*muyy(nx,ny,nz)));
mhy4(nx,ny,nz) = ...
    -(1/mhy0(nx,ny,nz))*(delt*sighxy(nx,ny,nz)*
sighzy(nx,ny,nz)/e0^2);


mhz0(nx,ny,nz) = (1/delt)+((sighxz(nx,ny,nz)+
sighyz(nx,ny,nz))/(2*e0))+
(sighxz(nx,ny,nz)*sighyz(nx,ny,nz)*delt/(4*e0^2));
mhz1(nx,ny,nz) = (1/mhz0(nx,ny,nz))*((1/delt)-
((sighxz(nx,ny,nz)+sighyz(nx,ny,nz))/(2*e0))-
(sighxz(nx,ny,nz)*sighyz(nx,ny,nz)*delt/(4*e0^2)));
%mhz2(nx,ny,nz) = -(1/mhz0(nx,ny,nz))*
(c0a/(muzz(nx,ny,nz)*einfz(nx,ny,nz)));
mhz2(nx,ny,nz) = ...
    -(1/mhz0(nx,ny,nz))*(c0a/(muzz(nx,ny,nz)));
mhz3(nx,ny,nz) = -(1/mhz0(nx,ny,nz))*
(c0a*delt*sighzz(nx,ny,nz)/(e0*muzz(nx,ny,nz)));
mhz4(nx,ny,nz) = -(1/mhz0(nx,ny,nz))*
(delt*sighxz(nx,ny,nz)*sighyz(nx,ny,nz)/e0^2);


mdx0(nx,ny,nz) = (1/delt)+((sigdyx(nx,ny,nz)+
sigdzx(nx,ny,nz))/(2*e0))+
(sigdyx(nx,ny,nz)*sigdzx(nx,ny,nz)*delt/(4*e0^2));
mdx1(nx,ny,nz) = (1/mdx0(nx,ny,nz))*((1/delt)-
((sigdyx(nx,ny,nz)+sigdzx(nx,ny,nz))/(2*e0))-
(sigdyx(nx,ny,nz)*sigdzx(nx,ny,nz)*delt/(4*e0^2)));
mdx2(nx,ny,nz) = c0a/(mdx0(nx,ny,nz));
```

```
mdx3(nx,ny,nz) = (1/mdx0(nx,ny,nz))*
(c0a*delt*sigdxx(nx,ny,nz)/(e0));
mdx4(nx,ny,nz) = -(1/mdx0(nx,ny,nz))*
(delt*sigdyx(nx,ny,nz)*sigdzx(nx,ny,nz)/e0^2);


mdy0(nx,ny,nz) = (1/delt)+((sigdxy(nx,ny,nz)+
sigdzy(nx,ny,nz))/(2*e0))+
(sigdxy(nx,ny,nz)*sigdzy(nx,ny,nz)*delt/(4*e0^2));
mdy1(nx,ny,nz) = (1/mdy0(nx,ny,nz))*((1/delt)-
((sigdxy(nx,ny,nz)+sigdzy(nx,ny,nz))/(2*e0))-
(sigdxy(nx,ny,nz)*sigdzy(nx,ny,nz)*delt/(4*e0^2)));
mdy2(nx,ny,nz) = c0a/(mdy0(nx,ny,nz));
mdy3(nx,ny,nz) = (1/mdy0(nx,ny,nz))*
(c0a*delt*sigdyy(nx,ny,nz)/(e0));
mdy4(nx,ny,nz) = -(1/mdy0(nx,ny,nz))*
(delt*sigdxy(nx,ny,nz)*sigdzy(nx,ny,nz)/e0^2);


mdz0(nx,ny,nz) = (1/delt)+((sigdxz(nx,ny,nz)+
sigdyz(nx,ny,nz))/(2*e0))+
(sigdxz(nx,ny,nz)*sigdyz(nx,ny,nz)*delt/(4*e0^2));
mdz1(nx,ny,nz) = (1/mdz0(nx,ny,nz))*((1/delt)-
((sigdxz(nx,ny,nz)+sigdyz(nx,ny,nz))/(2*e0))-
(sigdxz(nx,ny,nz)*sigdyz(nx,ny,nz)*delt/(4*e0^2)));
mdz2(nx,ny,nz) = c0a/(mdz0(nx,ny,nz));
mdz3(nx,ny,nz) = (1/mdz0(nx,ny,nz))*
(c0a*delt*sigdzz(nx,ny,nz)/(e0));
mdz4(nx,ny,nz) = -(1/mdz0(nx,ny,nz))*
(delt*sigdxz(nx,ny,nz)*sigdyz(nx,ny,nz)/e0^2);
    end
  end
end
```

```matlab
% Calculate Polarization current density update ...
    coefficients


for nx = 1:Nx
 for ny = 1:Ny
   for nz = 1:Nz
     cjjx(nx,ny,nz) = (1-(1/(2*Ntx(nx,ny,nz))))/
     (1+(1/(2*Ntx(nx,ny,nz))));
     cjex(nx,ny,nz) = ((1/Ntx(nx,ny,nz))/
     (1+(1/(2*Ntx(nx,ny,nz)))))*
     (e0*edx(nx,ny,nz)*delx/delt);
     cjjy(nx,ny,nz) = (1-(1/(2*Nty(nx,ny,nz))))/
     (1+(1/(2*Nty(nx,ny,nz))));
     cjey(nx,ny,nz) = ((1/Nty(nx,ny,nz))/
     (1+(1/(2*Nty(nx,ny,nz)))))*
     (e0*edy(nx,ny,nz)*dely/delt);
     cjjz(nx,ny,nz) = (1-(1/(2*Ntz(nx,ny,nz))))/
     (1+(1/(2*Ntz(nx,ny,nz))));
     cjez(nx,ny,nz) = ((1/Ntz(nx,ny,nz))/
     (1+(1/(2*Ntz(nx,ny,nz)))))*
     (e0*edz(nx,ny,nz)*delz/delt);
    end
   end
end


% Calculate E field update coefieicents (for Breast)

for nx = 1:Nx
  for ny = 1:Ny
    for nz = 1:Nz
```

```
e11x(nx,ny,nz)=(1-(sigdx1(nx,ny,nz)*delt/
(2*e0*einfx(nx,ny,nz)))+
(cjex(nx,ny,nz)*delt/(2*delx*e0*einfx(nx,ny,nz))))/...
(1+(sigdx1(nx,ny,nz)*delt/(2*e0*einfx(nx,ny,nz)))+
(cjex(nx,ny,nz)*delt/(2*delx*e0*einfx(nx,ny,nz))));

e12x(nx,ny,nz)= (c0a*delt)/(2*delx*einfx(nx,ny,nz)*
(1+(sigdx1(nx,ny,nz)*delt/
(2*e0*einfx(nx,ny,nz)))+(cjex(nx,ny,nz)*delt/
(2*delx*e0*einfx(nx,ny,nz)))));

e11y(nx,ny,nz)=(1-(sigdy1(nx,ny,nz)*delt/
(2*e0*einfy(nx,ny,nz)))+
(cjey(nx,ny,nz)*delt/(2*dely*e0*einfy(nx,ny,nz))))/...
(1+(sigdy1(nx,ny,nz)*delt/(2*e0*einfy(nx,ny,nz)))+
(cjey(nx,ny,nz)*delt/(2*dely*e0*einfy(nx,ny,nz))));

e12y(nx,ny,nz)= (c0a*delt)/(2*dely*einfy(nx,ny,nz)*
(1+(sigdy1(nx,ny,nz)*delt/(2*e0*einfy(nx,ny,nz)))+
(cjey(nx,ny,nz)*delt/(2*dely*e0*einfy(nx,ny,nz)))));

e11z(nx,ny,nz)=(1-(sigdz1(nx,ny,nz)*delt/
(2*e0*einfz(nx,ny,nz)))+
(cjez(nx,ny,nz)*delt/(2*delz*e0*einfz(nx,ny,nz))))/...
(1+(sigdz1(nx,ny,nz)*delt/(2*e0*einfz(nx,ny,nz)))+
(cjez(nx,ny,nz)*delt/(2*delz*e0*einfz(nx,ny,nz))));
e12z(nx,ny,nz)=(c0a*delt)/(2*delz*einfz(nx,ny,nz)*
(1+(sigdz1(nx,ny,nz)*delt/(2*e0*einfz(nx,ny,nz)))
+(cjez(nx,ny,nz)*delt/(2*delz*e0*einfz(nx,ny,nz)))));
    end
  end
```

```matlab
end

% Main FDTD Loop

for T=1:steps

%Cex (curl of Ex)


for nx = 1:Nx
 for ny = 1:Ny-1
   for nz = 1:Nz-1
    Cex(nx,ny,nz) = ((Ez(nx,ny+1,nz)-Ez(nx,ny,nz))/dely)-
    ((Ey(nx,ny,nz+1)-Ey(nx,ny,nz))/delz);
   end
    Cex(nx,ny,Nz) = ((Ez(nx,ny+1,Nz)-Ez(nx,ny,Nz))/dely)-
    ((0-Ey(nx,ny,Nz))/delz);
    Cex(nx,ny,nref) = ...
       ((Ez(nx,ny+1,nref)-Ez(nx,ny,nref))/dely)-
    ((Ey(nx,ny,nref+1)-Ey(nx,ny,nref))/delz)+
    (Eysrc(nx,ny,nref+1)/delz);
  end
  for nz =1:Nz-1
   Cex(nx,Ny,nz) = ...
      ((0-Ez(nx,Ny,nz))/dely)-((Ey(nx,Ny,nz+1)-
   Ey(nx,Ny,nz))/delz);
   Cex(nx,nref,nz) = ...
      ((Ez(nx,nref+1,nz)-Ez(nx,nref,nz))/dely)-
   ((Ey(nx,nref,nz+1)-Ey(nx,nref,nz))/delz)-
   (Ezsrcy(nx,nref+1,nz)/dely);
   end
```

160

```matlab
        Cex(nx,Ny,Nz) = ...
            ((0-Ez(nx,Ny,Nz))/dely)-((0-Ey(nx,Ny,Nz))/delz);
end


%  Cey (Curl of Ey)

for ny = 1:Ny
    for nx = 1:Nx-1
        for nz = 1:Nz-1
          Cey(nx,ny,nz) = ...
              ((Ex(nx,ny,nz+1)-Ex(nx,ny,nz))/delz)-
            ((Ez(nx+1,ny,nz)-Ez(nx,ny,nz))/delx);
        end
      Cey(nx,ny,Nz) = ...
          ((0-Ex(nx,ny,Nz))/delz)-((Ez(nx+1,ny,Nz)-
        Ez(nx,ny,Nz))/delx);
      Cey(nx,ny,nref) = ...
          ((Ex(nx,ny,nref+1)-Ex(nx,ny,nref))/delz)-
        ((Ez(nx+1,ny,nref)-Ez(nx,ny,nref))/delx)-
        (Exsrc(nx,ny,nref+1)/delz);
      end
    for nz =1:Nz-1
      Cey(Nx,ny,nz) = ((Ex(Nx,ny,nz+1)-Ex(Nx,ny,nz))/delz)-
        ((0-Ez(Nx,ny,nz))/delx);
      Cey(nref,ny,nz) = ...
          ((Ex(nref,ny,nz+1)-Ex(nref,ny,nz))/delz)-
        ((Ez(nref+1,ny,nz)-Ez(nref,ny,nz))/delx)+
        (Ezsrcx(nref+1,ny,nz)/delx);
    end
```

```matlab
        Cey(Nx,ny,Nz) = ...
            ((0-Ex(Nx,ny,Nz))/delz)-((0-Ez(Nx,ny,Nz))/delx);
end


% Cez(curl of Ez)


for nz = 1:Nz
  for nx = 1:Nx-1
    for ny = 1:Ny-1
      Cez(nx,ny,nz) = ...
          ((Ey(nx+1,ny,nz)-Ey(nx,ny,nz))/delx)-
        ((Ex(nx,ny+1,nz)-Ex(nx,ny,nz))/dely);
      end
    Cez(nx,Ny,nz) = ((Ey(nx+1,Ny,nz)-Ey(nx,Ny,nz))/delx)-
    ((0-Ex(nx,Ny,nz))/dely);
    Cez(nx,nref,nz) = ...
        ((Ey(nx+1,nref,nz)-Ey(nx,nref,nz))/delx)-
    ((Ex(nx,nref+1,nz)-Ex(nx,nref,nz))/dely)+
    (Exsrcy(nx,nref+1,nz)/dely);
  end
  for ny =1:Ny-1
   Cez(Nx,ny,nz) = ...
       ((0-Ey(Nx,ny,nz))/delx)-((Ex(Nx,ny+1,nz)-
   Ex(Nx,ny,nz))/dely);
   Cez(nref,ny,nz) = ...
       ((Ey(nref+1,ny,nz)-Ey(nref,ny,nz))/delx)-
   ((Ex(nref,ny+1,nz)-Ex(nref,ny,nz))/dely)-
   (Eysrcx(nref+1,ny,nz)/delx);
  end
  Cez(Nx,Ny,nz) = ...
      ((0-Ey(Nx,Ny,nz))/delx)-((0-Ex(Nx,Ny,nz))/dely);
```

```matlab
end


  % insert Electric field of Source


for nx = ft1:ft2
 for ny = ft11:ft22
  Exsrc(nx,ny,nref+1) = ...
     Ae*1.5*exp(-(((5*delt1*T)-t0)/(tau))^2);
  Eysrc(nx,ny,nref+1) = ...
     Ae*1.5*exp(-(((5*delt1*T)-t0)/(tau))^2);
 end
end
  % integration terms


for nx = 1:NPML(1)
 for ny = 1:NPML(1)
  for nz = 1:NPML(1)
   Icex(nx,ny,nz) = Icex(nx,ny,nz) + Cex(nx,ny,nz);
   IHx(nx,ny,nz) = IHx(nx,ny,nz) + Hx(nx,ny,nz);
   Icey(nx,ny,nz) = Icey(nx,ny,nz) + Cey(nx,ny,nz);
   IHy(nx,ny,nz) = IHy(nx,ny,nz)+ Hy(nx,ny,nz);
%  Icez(nx,ny,nz) = Icez(nx,ny,nz) + Cez(nx,ny,nz);
%  IHz(nx,ny,nz) = IHz(nx,ny,nz)+ Hz(nx,ny,nz);
  end
 end
end


for nx = Nx-NPML(1)+1:Nx
 for ny = Ny-NPML(1)+1:Ny
  for nz = Nz-NPML(1)+1:Nz
   Icex(nx,ny,nz) = Icex(nx,ny,nz) + Cex(nx,ny,nz);
```

163

```matlab
         IHx(nx,ny,nz) = IHx(nx,ny,nz) + Hx(nx,ny,nz);
         Icey(nx,ny,nz) = Icey(nx,ny,nz) + Cey(nx,ny,nz);
         IHy(nx,ny,nz) = IHy(nx,ny,nz)+ Hy(nx,ny,nz);
%    Icez(nx,ny,nz) = Icez(nx,ny,nz) + Cez(nx,ny,nz);
%    IHz(nx,ny,nz) = IHz(nx,ny,nz)+ Hz(nx,ny,nz);
       end
    end
end


  % update H



for nx = 1:Nx
 for ny = 1:Ny
  for nz = 1:Nz
   Hx(nx,ny,nz) =(mhx1(nx,ny,nz)*Hx(nx,ny,nz))+
   (mhx2(nx,ny,nz)*Cex(nx,ny,nz))+
   (mhx3(nx,ny,nz)*Icex(nx,ny,nz))+
   (mhx4(nx,ny,nz)*IHx(nx,ny,nz));
   Hy(nx,ny,nz) = (mhy1(nx,ny,nz)*Hy(nx,ny,nz))+
   (mhy2(nx,ny,nz)*Cey(nx,ny,nz))+
   (mhy3(nx,ny,nz)*Icey(nx,ny,nz))+
   (mhy4(nx,ny,nz)*IHy(nx,ny,nz));
   % Hz(nx,ny,nz) = (mhz1(nx,ny,nz)*Hz(nx,ny,nz))+
   (mhz2(nx,ny,nz)*Cez(nx,ny,nz))+
   (mhz3(nx,ny,nz)*Icez(nx,ny,nz))+
   (mhz4(nx,ny,nz)*IHz(nx,ny,nz));
   end
  end
end
```

```matlab
% Chx (Curl of Hx)

for nx = 1:Nx
  for ny = 2:Ny
    for nz = 2:Nz
      Chx(nx,ny,nz) = ...
          ((Hz(nx,ny,nz)-Hz(nx,ny-1,nz))/dely)-
        ((Hy(nx,ny,nz)-Hy(nx,ny,nz-1))/delz);
      end
    Chx(nx,ny,1) = ((Hz(nx,ny,1)-Hz(nx,ny-1,1))/dely)-
    ((Hy(nx,ny,1)-0)/delz);
    Chx(nx,ny,nref+1) ...
       =((Hz(nx,ny,nref+1)-Hz(nx,ny-1,nref+1))/dely)-
    ((Hy(nx,ny,nref+1)-Hy(nx,ny,nref))/delz)+
    (Hysrc(nx,ny,nref)/delz);
  end
  for nz =2:Nz
    Chx(nx,1,nz) =((Hz(nx,1,nz)-0)/dely)-((Hy(nx,1,nz)-
    Hy(nx,1,nz-1))/delz);
    Chx(nx,nref+1,nz) ...
       =((Hz(nx,nref+1,nz)-Hz(nx,nref,nz))/dely)-
    ((Hy(nx,nref+1,nz)-Hy(nx,nref+1,nz-1))/delz)-
    (Hzsrcy(nx,nref,nz)/dely);
  end
    Chx(nx,1,1) = ...
       ((Hz(nx,1,1)-0)/dely)-((Hy(nx,1,1)-0)/delz);
end

  %Chy (Curl of Hy)
for ny = 1:Ny
 for nx = 2:Nx
```

```matlab
    for nz = 2: Nz
     Chy(nx,ny,nz) = ((Hx(nx,ny,nz)-Hx(nx,ny,nz-1))/delz)-
     ((Hz(nx,ny,nz)-Hz(nx-1,ny,nz))/delx);
    end
     Chy(nx,ny,1) = ((Hx(nx,ny,1)-0)/delz)-
     ((Hz(nx,ny,1)-Hz(nx-1,ny,1))/delx);
     Chy(nx,ny,nref+1) = ...
        ((Hx(nx,ny,nref+1)-Hx(nx,ny,nref))/delz)-
     ((Hz(nx,ny,nref+1)-Hz(nx-1,ny,nref+1))/delx)-
     (Hxsrc(nx,ny,nref)/delz);
   end
    for nz =2: Nz
     Chy(1,ny,nz) = ((Hx(1,ny,nz)-Hx(1,ny,nz-1))/delz)-
     ((Hz(1,ny,nz)-0)/delx);
     Chy(nref+1,ny,nz) = ((Hx(nref+1,ny,nz)-
     Hx(nref+1,ny,nz-1))/delz)-
     ((Hz(nref+1,ny,nz)-Hz(nref,ny,nz))/delx)+
     (Hzsrcx(nref,ny,nz)/delx);
    end
     Chy(1,ny,1) = ...
        ((Hx(1,ny,1)-0)/delz)-((Hz(1,ny,1)-0)/delx);
end

%Chz (Curl of Hz)

for nz = 1: Nz
 for nx = 2: Nx
  for ny = 2: Ny
   Chz(nx,ny,nz) = ((Hy(nx,ny,nz)-Hy(nx-1,ny,nz))/delx)-
   ((Hx(nx,ny,nz)-Hx(nx,ny-1,nz))/dely);
  end
```

```matlab
    Chz(nx,1,nz) = ((Hy(nx,1,nz)-Hy(nx-1,1,nz))/delx)-...
    ((Hx(nx,1,nz)-0)/dely);
     Chz(nx,nref+1,nz) = ...
        ((Hy(nx,nref+1,nz)-Hy(nx-1,nref+1,nz))/delx)-...
     ((Hx(nx,nref+1,nz)-Hx(nx,nref,nz))/dely)+...
     (Hxsrcy(nx,nref,nz)/dely);
   end
   for ny =2:Ny
    Chz(1,ny,nz) = ((Hy(1,ny,nz)-0)/delx)-...
    ((Hx(1,ny,nz)-Hx(1,ny,nz))/dely);
    Chz(nref+1,ny,nz) = ...
        ((Hy(nref+1,ny,nz)-Hy(nref,ny,nz))/delx)-...
    ((Hx(nref+1,ny,nz)-Hx(nref+1,ny-1,nz))/dely)-...
    (Hysrcx(nref,ny,nz)/delx);
   end
    Chz(1,1,nz) = ...
        ((Hy(1,1,nz)-0)/delx)-((Hx(1,1,nz)-0)/dely);
end

% Insert Magnetic field of Source

for nx = ft1:ft2
   for ny = ft11:ft22
    Hxsrc(nx,ny,nref) = ...
        Ah*1.5*exp(-(((5*delt1*T)-t0+delts)/...
    (tau))^2);
    Hysrc(nx,ny,nref) = ...
        Ah*1.5*exp(-(((5*delt1*T)-t0+delts)/...
    (tau))^2);
   end
end
```

```matlab
% integration terms

for nx = 1:NPML(1)
 for ny = 1:NPML(1)
  for nz = 1:NPML(1)
   Ichx(nx,ny,nz) = Ichx(nx,ny,nz) + Chx(nx,ny,nz);
   IDx(nx,ny,nz) = IDx(nx,ny,nz) + Dx(nx,ny,nz);
   Ichy(nx,ny,nz) = Ichy(nx,ny,nz) + Chy(nx,ny,nz);
   IDy(nx,ny,nz) = IDy(nx,ny,nz)+ Dy(nx,ny,nz);
%   Ichz(nx,ny,nz) = Ichy(nx,ny,nz) + Chz(nx,ny,nz);
%   IDz(nx,ny,nz) = IDz(nx,ny,nz)+ Dz(nx,ny,nz);
  end
 end
end

for nx = Nx-NPML(1)+1:Nx
 for ny = Ny-NPML(1)+1:Ny
  for nz = Nz-NPML(1)+1:Nz
   Ichx(nx,ny,nz) = Ichx(nx,ny,nz) + Chx(nx,ny,nz);
   IDx(nx,ny,nz) = IDx(nx,ny,nz) + Dx(nx,ny,nz);
   Ichy(nx,ny,nz) = Ichy(nx,ny,nz) + Chy(nx,ny,nz);
   IDy(nx,ny,nz) = IDy(nx,ny,nz)+ Dy(nx,ny,nz);
%   Ichz(nx,ny,nz) = Ichy(nx,ny,nz) + Chz(nx,ny,nz);
%   IDz(nx,ny,nz) = IDz(nx,ny,nz)+ Dz(nx,ny,nz);
  end
 end
end

 % Update D in the UPML
```

```matlab
for nx = 1:NPML(1)
  for ny = 1:NPML(1)
    for nz = 1:NPML(1)
      Dx(nx,ny,nz) = (mdx1(nx,ny,nz)*Dx(nx,ny,nz))+
      (mdx2(nx,ny,nz)*Chx(nx,ny,nz))+
      (mdx3(nx,ny,nz)*Ichx(nx,ny,nz))+
      (mdx4(nx,ny,nz)*IDx(nx,ny,nz));
      Dy(nx,ny,nz) = (mdy1(nx,ny,nz)*Dy(nx,ny,nz))+
      (mdy2(nx,ny,nz)*Chy(nx,ny,nz))+
      (mdy3(nx,ny,nz)*Ichy(nx,ny,nz))+
      (mdy4(nx,ny,nz)*IDy(nx,ny,nz));
      % Dz(nx,ny,nz) = (mdz1(nx,ny,nz)*Dz(nx,ny,nz))+
      (mdz2(nx,ny,nz)*Chz(nx,ny,nz))+
      (mdz3(nx,ny,nz)*Ichz(nx,ny,nz))+
      (mdz4(nx,ny,nz)*IDz(nx,ny,nz));
      Ex(nx,ny,nz) = (1/exx(nx,ny,nz))*Dx(nx,ny,nz);
      Ey(nx,ny,nz) = (1/eyy(nx,ny,nz))*Dy(nx,ny,nz);
      % Ez(nx,ny,nz) = (1/ezz(nx,ny,nz))*Dz(nx,ny,nz);
      end
    end
end

% Update E in the numerical breast phantom

for nx = NPML(1)+1:Nx-NPML(1)
  for ny = NPML(1)+1:Ny-NPML(1)
    for nz = NPML(1)+1:Nz-NPML(1)
    Etmpx(nx,ny,nz)= Ex(nx,ny,nz);
    Etmpy(nx,ny,nz)= Ey(nx,ny,nz);
    % Etmpz(nx,ny,nz)= Ez(nx,ny,nz);
    Ex(nx,ny,nz) = (e11x(nx,ny,nz)*Ex(nx,ny,nz))+
```

```matlab
        (e12x(nx,ny,nz)*((2*delx*Chx(nx,ny,nz))-
        ((z0)*(1+cjjx(nx,ny,nz))*delx*jpx(nx,ny,nz))));
        Ey(nx,ny,nz) = (e11y(nx,ny,nz)*Ey(nx,ny,nz))+
        (e12y(nx,ny,nz)*((2*dely*Chy(nx,ny,nz))-
        ((z0)*(1+cjjy(nx,ny,nz))*dely*jpy(nx,ny,nz))));
        % Ez(nx,ny,nz) = (e11z(nx,ny,nz)*Ez(nx,ny,nz))+
          (e12z(nx,ny,nz)*((2*delz*Chz(nx,ny,nz))-
          ((z0)*(1+cjjz(nx,ny,nz))*delz*jpz(nx,ny,nz))));


        jpx(nx,ny,nz) = (cjjx(nx,ny,nz)*jpx(nx,ny,nz))+
        (cjex(nx,ny,nz)*(Ex(nx,ny,nz)-Etmpx(nx,ny,nz))/delx);
        jpy(nx,ny,nz) = (cjjy(nx,ny,nz)*jpy(nx,ny,nz))+
        (cjey(nx,ny,nz)*(Ey(nx,ny,nz)-Etmpy(nx,ny,nz))/dely);
       %jpz(nx,ny,nz) = (cjjz(nx,ny,nz)*jpz(nx,ny,nz))+
        (cjez(nx,ny,nz)*(Ez(nx,ny,nz)-Etmpz(nx,ny,nz))/delz);
          end
      end
  end


% Update D in the UPML

for nx = (Nx-NPML(1)+1):Nx
 for ny = (Ny-NPML(1)+1):Ny
   for nz = (Nz-NPML(1)+1):Nz
      Dx(nx,ny,nz) = (mdx1(nx,ny,nz)*Dx(nx,ny,nz))+
      (mdx2(nx,ny,nz)*Chx(nx,ny,nz))+
      (mdx3(nx,ny,nz)*Ichx(nx,ny,nz))+
      (mdx4(nx,ny,nz)*IDx(nx,ny,nz));
      Dy(nx,ny,nz) = (mdy1(nx,ny,nz)*Dy(nx,ny,nz))+
      (mdy2(nx,ny,nz)*Chy(nx,ny,nz))+
      (mdy3(nx,ny,nz)*Ichy(nx,ny,nz))+
```

```matlab
               (mdy4(nx,ny,nz)*IDy(nx,ny,nz));
%    Dz(nx,ny,nz) = (mdz1(nx,ny,nz)*Dz(nx,ny,nz))+
               (mdz2(nx,ny,nz)*Chz(nx,ny,nz))+
               (mdz3(nx,ny,nz)*Ichz(nx,ny,nz))+
               (mdz4(nx,ny,nz)*IDz(nx,ny,nz));

        Ex(nx,ny,nz) = (1/exx(nx,ny,nz))*Dx(nx,ny,nz);
        Ey(nx,ny,nz) = (1/eyy(nx,ny,nz))*Dy(nx,ny,nz);
%    Ez(nx,ny,nz) = (1/ezz(nx,ny,nz))*Dz(nx,ny,nz);
      end
   end
end


if (mod(T,100)==0)

  fig=figure;
  h1 = subplot(2,2,1);
  slice(X,Y,Z,Ey,[],[],8);
  shading interp
  colormap hsv
  axis equal tight
  axis off;
  caxis auto
  colorbar
  view(2)
  movegui(h1,'onscreen');
 set(gca,'nextplot','replacechildren');
 set(gcf,'Renderer','zbuffer');
 drawnow;
 hold all;
```

```matlab
h2 = subplot(2,2,2);
slice(X,Y,Z,Ey,[],[],13);
shading interp
colormap hsv
 axis equal tight
 axis off;
 caxis auto
 colorbar
 view(2)

 movegui(h2,'onscreen');
 set(gca,'nextplot','replacechildren');
 set(gcf,'Renderer','zbuffer');
 drawnow;
 hold all;

h3 = subplot(2,2,3);
slice(X,Y,Z,Ey,[],[],21);
  shading interp
  colormap hsv
  axis equal tight
  axis off;
  caxis auto
  colorbar
  view(2)
 movegui(h3,'onscreen');
 set(gca,'nextplot','replacechildren');
 set(gcf,'Renderer','zbuffer');
 drawnow;
 hold all;
```

```matlab
h4 = subplot(2,2,4);
slice(X,Y,Z,Ey,[],[],31);
  shading interp
  colormap hsv
  axis equal tight
  axis off;
  caxis auto
  colorbar
  view(2)
 movegui(h4,'onscreen');
 set(gca,'nextplot','replacechildren');
 set(gcf,'Renderer','zbuffer');
 drawnow;
 hold all;
 end
end
```

C.4 Integral of Green's Function for Method of Moments

Forward problem is solved by method of moment for electromagnetic imaging. Integral of green's function is required in method of moments. Integral of green's function is calculated by this code.

```
clc;
clear all;
close all;
u0 = 4*pi*10^-9;
mu0 = u0;
e0 = 8.854*10^-14;
del_l = 0.5;
a = ((3/(4*pi))^(1/3))*del_l;
u1 = [1 0 0];
u2 = [0 1 0];
u3 = [0 0 1];
dx = 0.5;
dy = 0.5;
dz = 0.5;
%c1 = input('Enter number of cells:');
Nx1 = 40;
Ny1 = 40;
Nz1 = 40;
c=3e10;
Nv = Nx1*Ny1*Nz1;
Nfreq = 4;
f = 5e8;
f1 = 5e8;
```

```matlab
f2 = 2e9;
Na = 40;
MF = Na*Nfreq;
freq = linspace(f1,f2,Nfreq);
k= 2*pi./(c./freq);
w = 2*pi.*freq;
xn = zeros(Nv,1);
yn = zeros(Nv,1);
zn = zeros(Nv,1);
ed = zeros(Nx1,Ny1,Nz1);
einf = ones(Nx1,Ny1,Nz1);
sigd =  zeros(Nx1,Ny1,Nz1);
 tau = 15e-12;
 w = 2*pi.*freq;
cinf = 1;
cdel = 1./(1+1i*w.*tau);
csig = 1./(1i*w.*e0);
%k(p) = 2*pi/(c/f);
L = 1;
Iz = 0.000001;
n = 377;
i0 =0.000001;
l=1;
p=1;
%Na=40;
N = 40;
[z, y, x] = ndgrid(.5:N); %// note reverse order to ...
   get desired order of result
vc1 = [x(:) y(:) z(:)]; %// desired result

m(1:64000,1:3) = 20;
```

```matlab
vc2 = m-vc1;
vc = vc2*0.5;


for i=1:Nv


    rL(:,:,i)=vc(i,:);
end


for i = 1:5
rm(:,:,1+8*(i-1)) = [15 0 6.75-4*(i-1)];
rm(:,:,2+8*(i-1)) = [10.61 10.61 6.75-4*(i-1)];
rm(:,:,3+8*(i-1))= [0 15 6.75-4*(i-1)];
rm(:,:,4+8*(i-1)) = [-10.61 10.61 6.75-4*(i-1)];
rm(:,:,5+8*(i-1))= [-15 0 6.75-4*(i-1)];
rm(:,:,6+8*(i-1)) = [-10.61 -10.61 6.75-4*(i-1)];
rm(:,:,7+8*(i-1)) = [0 -15 6.75-4*(i-1)];
rm(:,:,8+8*(i-1)) = [10.61 -10.61 6.75-4*(i-1)];
end


for m = 1:Na
 for n = 1:Nv
  r = ((rL(1,1,n)-rm(1,1,m))^2+(rL(1,2,n)-rm(1,2,m))^2+
  (rL(1,3,n)-rm(1,3,m))^2)^0.5;
  x1 = rL(1,1,n)-rm(1,1,m);
  y1 = rL(1,2,n)-rm(1,2,m);
  c = k(p)*r;
  d = 1/c;
  e = 1/c.^2;
  er(n,1) = ((n*i0*l*x1)/(2*pi*r^3))*(1-1i*d)*exp(-1i*c);
  eth(n,1) = ((1i*n*k(p)*i0*l*y1)/(4*pi*r^2))*
  (1-1i*d-e)*exp(-1i*c);
```

```matlab
        ephi(n,1) = 0;
         end
    [x,y,z] = sph2cart(eth,ephi,er);
    xn = xn+x;
    yn=yn+y;
    zn=zn+z;
end


for m=1:Nv
    rfx1(:,:,m) = rL(:,:,m) + ( (-1)^1*(del_l/2)).*u1;
    rfx2(:,:,m) = rL(:,:,m) + ( (-1)^2*(del_l/2)).*u1;
    rfy1(:,:,m) = rL(:,:,m) + ( (-1)^1*(del_l/2)).*u2;
    rfy2(:,:,m) = rL(:,:,m) + ( (-1)^2*(del_l/2)).*u2;
    rfz1(:,:,m) = rL(:,:,m) + ( (-1)^1*(del_l/2)).*u3;
    rfz2(:,:,m) = rL(:,:,m) + ( (-1)^2*(del_l/2)).*u3;
end


for m=1:Na
 for n =1:Nv
  rml(m,n) =((rm(1,1,m)-rL(1,1,n))^2 + ...
     (rm(1,2,m)-rL(1,2,n))^2+
  (rm(1,3,m)-rL(1,3,n))^2)^0.5;
  rx1(m) =((rm(1,1,m)-rfx1(1,1,m))^2 + ...
     (rm(1,2,m)-rfx1(1,2,m))^2+
  (rm(1,3,m)-rfx1(1,3,m))^2)^0.5;
  rx2(m) =((rm(1,1,m)-rfx2(1,1,m))^2 + ...
     (rm(1,2,m)-rfx2(1,2,m))^2+
  (rm(1,3,m)-rfx2(1,3,m))^2)^0.5;
  ry1(m) =((rm(1,1,m)-rfy1(1,1,m))^2 + ...
     (rm(1,2,m)-rfy1(1,2,m))^2+
  (rm(1,3,m)-rfy1(1,3,m))^2)^0.5;
```

177

```matlab
    ry2(m)  =((rm(1,1,m)-rfy2(1,1,m))^2 + ...
        (rm(1,2,m)-rfy2(1,2,m))^2+
    (rm(1,3,m)-rfy2(1,3,m))^2)^0.5;
    rz1(m)  =((rm(1,1,m)-rfz1(1,1,m))^2 + ...
        (rm(1,2,m)-rfz1(1,2,m))^2+
    (rm(1,3,m)-rfz1(1,3,m))^2)^0.5;
    rz2(m)  =((rm(1,1,m)-rfz2(1,1,m))^2 + ...
        (rm(1,2,m)-rfz2(1,2,m))^2+
    (rm(1,3,m)-rfz2(1,3,m))^2)^0.5;
  end
end

% Generation of Matrix B1 and A1

for m = 1:Na
  for n =1:Nv
   [y,z]=meshgrid(rL(1,2,n)-(del_l/2):dy:rL(1,2,n)+
   (del_l/2),rL(1,3,n)-(del_l/2):dz:rL(1,3,n)+(del_l/2));
   [x,z1]=meshgrid(rL(1,1,n)-(del_l/2):dx:rL(1,1,n)+
   (del_l/2),rL(1,3,n)-(del_l/2):dz:rL(1,3,n)+(del_l/2));
   [x1,y1]=meshgrid(rL(1,1,n)-(del_l/2):dx:rL(1,1,n)+
   (del_l/2),rL(1,2,n)-(del_l/2):dy:rL(1,2,n)+(del_l/2));
   %  "Gmlxx element"

   rxx1_n =((rm(1,1,m)-rfx1(1,1,n)).^2 + ...
       (rm(1,2,m)-y).^2 +
   (rm(1,3,m)-z).^2).^0.5;
   rxx2_n =((rm(1,1,m)-rfx2(1,1,n)).^2 + ...
       (rm(1,2,m)-y).^2 +
   (rm(1,3,m)-z).^2).^0.5;
   Gxx1  =((1+1i*k(p).*rxx1_n)./(4*pi.*(rxx1_n).^3)).*
```

```matlab
exp(-1i*k(p).*rxx1_n).*(rm(1,1,m)-rfx1(1,1,n));
Gxx2 =((1+1i*k(p).*rxx2_n)./(4*pi.*(rxx2_n).^3)).*
exp(-1i*k(p).*rxx2_n).*(rm(1,1,m)-rfx2(1,1,n));
IGxx1 = sum(sum(Gxx1))*(dy*dz);
IGxx2= sum(sum(Gxx2))*(dy*dz);
B1(1+(m-1)*3,1+(n-1)*3)=((exp(-1i*k(p).*rml(m,n)))./
(k(p).*rml(m,n)))*
(sin(k(p)*a)-(k(p)*a*cos(k(p)*a)))-IGxx1+IGxx2;
%display(IGxx1);


%  "Gmlxy element"
rxx1_n =((rm(1,1,m)-x).^2 + ...
   (rm(1,2,m)-rfy1(1,2,n)).^2 +
(rm(1,3,1)-z1).^2).^0.5;
rxx2_n =((rm(1,1,m)-x).^2 + ...
   (rm(1,2,m)-rfy2(1,2,n)).^2 +
(rm(1,3,1)-z1).^2).^0.5;
Gxx1 =((1+1i*k(p).*rxx1_n)./(4*pi.*(rxx1_n).^3)).*
exp(-1i*k(p).*rxx1_n).*(rm(1,1,m)-x);
Gxx2 =((1+1i*k(p).*rxx2_n)./(4*pi.*(rxx2_n).^3)).*
exp(-1i*k(p).*rxx2_n).*(rm(1,1,m)-x);
IGxy1 =sum(sum(Gxx1))*(dx*dz);
IGxy2 =sum(sum(Gxx2))*(dx*dz);
B1(1+(m-1)*3,2+(n-1)*3) = ((exp(-1i*k(p).*rml(m,n)))./
(k(p).*rml(m,n)))*
(sin(k(p)*a)-(k(p)*a*cos(k(p)*a)))-IGxy1+IGxy2;
%display(IGxy1);


%  "Gmlxz element"
rxx1_n = ((rm(1,1,m)-x1).^2 + (rm(1,2,m)-y1).^2 +
(rm(1,3,m)-rfz1(1,3,n)).^2).^0.5;
```

```matlab
rxx2_n = ((rm(1,1,m)-x1).^2 + (rm(1,2,m)-y1).^2 +
(rm(1,3,m)-rfz2(1,3,n)).^2).^0.5;
Gxx1 = ((1+1i*k(p).*rxx1_n)./(4*pi.*(rxx1_n).^3)).*
exp(-1i*k(p).*rxx1_n).*(rm(1,1,m)-x1);
Gxx2 = ((1+1i*k(p).*rxx2_n)./(4*pi.*(rxx2_n).^3)).*
exp(-1i*k(p).*rxx2_n).*(rm(1,1,m)-x1);
IGxz1 = sum(sum(Gxx1))*(dx*dy);
IGxz2 = sum(sum(Gxx2))*(dx*dy);
B1(1+(m-1)*3,3+(n-1)*3) =((exp(-1i*k(p).*rml(m,n)))./
(k(p).*rml(m,n)))*
(sin(k(p)*a)-(k(p)*a*cos(k(p)*a)))-IGxz1+IGxz2;


%  "Gmlyx element"
rxx1_n = ((rm(1,1,m)-rfx1(1,1,n)).^2 + ...
   (rm(1,2,m)-y).^2 +
(rm(1,3,m)-z).^2).^0.5;
rxx2_n = ((rm(1,1,m)-rfx2(1,1,n)).^2 + ...
   (rm(1,2,m)-y).^2 +
(rm(1,3,m)-z).^2).^0.5;
Gxx1 = ((1+1i*k(p).*rxx1_n)./(4*pi.*(rxx1_n).^3)).*
exp(-1i*k(p).*rxx1_n).*(rm(1,2,m)-y);
Gxx2 = ((1+1i*k(p).*rxx2_n)./(4*pi.*(rxx2_n).^3)).*
exp(-1i*k(p).*rxx2_n).*(rm(1,2,m)-y);
IGyx1 = sum(sum(Gxx1))*(dy*dz);
IGyx2 = sum(sum(Gxx2))*(dy*dz);
B1(2+(m-1)*3,1+(n-1)*3) = ((exp(-1i*k(p).*rml(m,n)))./
(k(p).*rml(m,n)))*
(sin(k(p)*a)-(k(p)*a*cos(k(p)*a)))-IGyx1+IGyx2;


%  "Gmlyy element"
```

```
rxx1_n = ((rm(1,1,m)-x).^2 + ...
    (rm(1,2,m)-rfy1(1,2,n)).^2 +
(rm(1,3,m)-z1).^2).^0.5;
rxx2_n = ((rm(1,1,m)-x).^2 + ...
    (rm(1,2,m)-rfy2(1,2,n)).^2 +
(rm(1,3,m)-z1).^2).^0.5;
Gxx1 = ((1+1i*k(p).*rxx1_n)./(4*pi.*(rxx1_n).^3)).*
exp(-1i*k(p).*rxx1_n).*(rm(1,2,m)-rfy1(1,2,n));
Gxx2 = ((1+1i*k(p).*rxx2_n)./(4*pi.*(rxx2_n).^3)).*
exp(-1i*k(p).*rxx2_n).*(rm(1,2,m)-rfy2(1,2,n));
IGyy1 = sum(sum(Gxx1))*(dx*dz);
IGyy2 = sum(sum(Gxx2))*(dx*dz);
B1(2+(m-1)*3,2+(n-1)*3) = ((exp(-1i*k(p).*rml(m,n)))./
(k(p).*rml(m,n)))*
(sin(k(p)*a)-(k(p)*a*cos(k(p)*a)))-IGyy1+IGyy2;

% "Gmlyz element"
rxx1_n = ((rm(1,1,m)-x1).^2 + (rm(1,2,m)-y1).^2 +
(rm(1,3,m)-rfz1(1,3,n)).^2).^0.5;
rxx2_n = ((rm(1,1,m)-x1).^2 + (rm(1,2,m)-y1).^2 +
(rm(1,3,m)-rfz2(1,3,n)).^2).^0.5;
Gxx1 = ((1+1i*k(p).*rxx1_n)./(4*pi.*(rxx1_n).^3)).*
exp(-1i*k(p).*rxx1_n).*(rm(1,2,m)-y1);
Gxx2 = ((1+1i*k(p).*rxx2_n)./(4*pi.*(rxx2_n).^3)).*
exp(-1i*k(p).*rxx2_n).*(rm(1,2,m)-y1);
IGyz1 = sum(sum(Gxx1))*(dx*dy);
IGyz2 = sum(sum(Gxx2))*(dx*dy);
B1(2+(m-1)*3,3+(n-1)*3) = ((exp(-1i*k(p).*rml(m,n)))./
(k(p).*rml(m,n)))*
(sin(k(p)*a)-(k(p)*a*cos(k(p)*a)))-IGyz1+IGyz2;
```

```matlab
% "Gmlzx element"
rxx1_n = ((rm(1,1,m)-rfx1(1,1,n)).^2 + ...
    (rm(1,2,m)-y).^2 +
(rm(1,3,m)-z).^2).^0.5;
rxx2_n = ((rm(1,1,m)-rfx2(1,1,n)).^2 + ...
    (rm(1,2,m)-y).^2 +
(rm(1,3,m)-z).^2).^0.5;
Gxx1 = ((1+1i*k(p).*rxx1_n)./(4*pi.*(rxx1_n).^3)).*
exp(-1i*k(p).*rxx1_n).*(rm(1,3,m)-z);
Gxx2 = ((1+1i*k(p).*rxx2_n)./(4*pi.*(rxx2_n).^3)).*
exp(-1i*k(p).*rxx2_n).*(rm(1,3,m)-z);
IGzx1 = sum(sum(Gxx1))*(dy*dz);
IGzx2 = sum(sum(Gxx2))*(dy*dz);
B1(3+(m-1)*3,1+(n-1)*3) = ((exp(-1i*k(p).*rml(m,n)))./
(k(p).*rml(m,n)))*
(sin(k(p)*a)-(k(p)*a*cos(k(p)*a)))-IGzx1+IGzx2;

% "Gmlzy element"
rxx1_n = ((rm(1,1,m)-x).^2 + ...
    (rm(1,2,m)-rfy1(1,2,n)).^2 +
(rm(1,3,m)-z1).^2).^0.5;
rxx2_n = ((rm(1,1,m)-x).^2 + ...
    (rm(1,2,1)-rfy2(1,2,n)).^2 +
(rm(1,3,m)-z1).^2).^0.5;
Gxx1 = ((1+1i*k(p).*rxx1_n)./(4*pi.*(rxx1_n).^3)).*
exp(-1i*k(p).*rxx1_n).*(rm(1,3,m)-z1);
Gxx2 = ((1+1i*k(p).*rxx2_n)./(4*pi.*(rxx2_n).^3)).*
exp(-1i*k(p).*rxx2_n).*(rm(1,3,m)-z1);
IGzy1 = sum(sum(Gxx1))*(dx*dz);
IGzy2 = sum(sum(Gxx2))*(dx*dz);
B1(3+(m-1)*3,2+(n-1)*3) = ((exp(-1i*k(p).*rml(m,n)))./
```

```matlab
(k(p).*rml(m,n)))*
(sin(k(p)*a)-(k(p)*a*cos(k(p)*a)))-IGzy1+IGzy2;
% "Gmlzz element"
rxx1_n = ((rm(1,1,m)-x1).^2 + (rm(1,2,m)-y1).^2 +
(rm(1,3,m)-rfz1(1,3,n)).^2).^0.5;
rxx2_n = ((rm(1,1,m)-x1).^2 + (rm(1,2,m)-y1).^2 +
(rm(1,3,m)-rfz2(1,3,n)).^2).^0.5;
Gxx1 = ((1+1i*k(p).*rxx1_n)./
(4*pi.*(rxx1_n).^3)).*
exp(-1i*k(p).*rxx1_n).*(rm(1,3,m)-rfz1(1,3,n));
Gxx2 = ((1+1i*k(p).*rxx2_n)./(4*pi.*(rxx2_n).^3)).*
exp(-1i*k(p).*rxx2_n).*(rm(1,3,m)-rfz2(1,3,n));
IGzz1 =sum(sum(Gxx1))*(dx*dy);
IGzz2 = sum(sum(Gxx2))*(dx*dy);
B1(3+(m-1)*3,3+(n-1)*3) = ((exp(-1i*k(p).*rml(m,n)))./
(k(p).*rml(m,n)))*
(sin(k(p)*a)-(k(p)*a*cos(k(p)*a)))-IGzz1+IGzz2;

A1(1+(m-1)*3,1+(n-1)*3) = ...
   exp(-1i*k(p)*a)*(1+(1i*k(p)*a))-1;
A1(1+(m-1)*3,2+(n-1)*3) = ((exp(-1i*k(p).*rml(m,n)))/
(k(p).*rml(m,n)))*(sin(k(p)*a)-(k(p)*a*cos(k(p)*a)));
A1(1+(m-1)*3,3+(n-1)*3) = ((exp(-1i*k(p).*rml(m,n)))/
(k(p).*rml(m,n)))*(sin(k(p)*a)-(k(p)*a*cos(k(p)*a)));
A1(2+(m-1)*3,1+(n-1)*3) = ((exp(-1i*k(p).*rml(m,n)))/
(k(p).*rml(m,n)))*(sin(k(p)*a)-(k(p)*a*cos(k(p)*a)));
 A1(2+(m-1)*3,2+(n-1)*3) = ...
    exp(-1i*k(p)*a)*(1+(1i*k(p)*a))-1;
 A1(2+(m-1)*3,3+(n-1)*3) = ((exp(-1i*k(p).*rml(m,n)))/
 (k(p).*rml(m,n)))*(sin(k(p)*a)-(k(p)*a*cos(k(p)*a)));
 A1(3+(m-1)*3,1+(n-1)*3) = ((exp(-1i*k(p).*rml(m,n)))/
```

```
            (k(p).*rml(m,n)))*(sin(k(p)*a)-(k(p)*a*cos(k(p)*a)));
            A1(3+(m-1)*3,2+(n-1)*3) = ((exp(-1i*k(p).*rml(m,n)))/
            (k(p).*rml(m,n)))*(sin(k(p)*a)-(k(p)*a*cos(k(p)*a)));
            A1(3+(m-1)*3,3+(n-1)*3) = ...
                exp(-1i*k(p)*a)*(1+(1i*k(p)*a))-1;
        end
    end



display(A1);
display(B1);
```

List of Publications

Book Chapter

1. H.N.Patel and D.K.Ghodgaonkar, "Application of 3D level set based optimization in microwave breast imaging for cancer detection" accepted in Level Set Method in Medical Imaging Segmentation, Boca Raton:Fl, USA, CRC Press.

International Journal

1. H.N.Patel and D.K.Ghodgaonkar, "Study of effect of numerical breast phantom heterogeneity on dielectric profile reconstruction using microwave imaging," Progress In Electromagnetics Research M, Vol. 58, pp. 135-145, 2017.

2. H.N.Patel and D.K.Ghodgaonkar, "Application of group theory for computation reduction in microwave imaging of human breast model at 500 MHz," Progress In Electromagnetics Research M, Vol. 51, pp. 165-173, 2016.

International Conference Proceedings

1. H.N.Patel and D.K.Ghodgaonkar,"3D level set based optimization of inverse scattering problem for microwave breast imaging", IEEE MTT-S International Microwave Bio Conference, 15-17 May 2017, Gothenburg, Sweden, pp. 1-4.

2. H.N.Patel and D.K.Ghodgaonkar,"The effect of noise on complex permittivity reconstruction in mathematical breast model", IEEE International Conference on Systems in Medicine and Biology, 4-7 January 2016, IIT Kharagpur, pp. 13-16.

3. H.N.Patel and D.K.Ghodgaonkar,"Computationally efficient microwave imaging of human breast model using group theory" IEEE MTT-S International Microwave and RF Conference,10-12 December 2015, Hyderabad, pp. 81-84.